Development of Thin-Film Based Microdevices and Process Enhancement for Making the Same

Qing Guo

A dissertation
submitted in partial fulfillment of the
requirements for the degree of

Doctor of Philosophy

University of Washington
2012

Reading Committee:
I-Yeu (Steve) Shen, Chair
Guozhong Cao, Co-Chair
Qiuming Yu

Program Authorized to Offer Degree:
Mechanical Engineering

©Copyright 2012
Qing Guo

DEDICATION

This Ph.D. dissertation is dedicated to my beloved grandparents, respective parents, and my entire families, who have been my constant source of inspiration. They have given me the drive, discipline, and strength to tackle any challenging task with enthusiasm, confidence, and determination. Without their deep love, knowledge, patience, and devotion, my academic achievements would not have been made possible!

ACKNOWLEDGEMENTS

I wish to express sincere appreciation to my home department, Mechanical Engineering, for their long-term support, and especially to my two academic advisors, Professor Shen and Professor Cao, for their knowledge, patience, guidance, and inspiration.

I also would like to thank my thesis committee members, Professor Karl F. Böhringer, Professor Jiangyu Li, Professor Qiuming Yu, Professor Robert B. Darling (GSR), and Professor Anant M. P. Anantram (GSR), for their generous help and valuable instructions.

A special acknowledgement should be given to the Department of Physics. Without their three-year continuous TA financial assistantship, I would not be able to keep my graduate study.

Meanwhile, I want to thank all my lab mates. They are Tsung-Liang (Anthony) Wu, Cheng-Chun (Ryan) Lee, Chia-Che (Joseph) Wu, Chuan Luo, Hsien-Lin (Stacey) Huang, and Bobby Manson. With the absence of their endless support, my project would not even be able to move forward.

A very special thank is given to my wife, Shin-Chih Hu, and my dog, Hsiao-Hsuan Hu, for their encouragement, understanding, and devotion.

At last, I want to express deep appreciation to all my true friends, who unselfishly share their life experience and happiness with me.

University of Washington

Abstract

Development of Thin-Film Based Microdevices and Process Enhancement for Making the Same

Qing Guo

Co-Chairs of the Supervisory Committee:

Professor I-Yeu (Steve) Shen
Department of Mechanical Engineering

Professor Guozhong Cao
Department of Material Science and Engineering

Microdevices driven by Lead Zirconate Titanate ($PbZr_xTi_{1-x}O_3$ or PZT) have received wide attention recently, because they could potentially outperform other MEMS devices in terms of bandwidth, energy density, and actuation strength. PZT integrated microdevice is undoubtedly promising, but its development and fabrication still remains challenging. To cope with such challenges and develop a well functional microdevice with adoption of thin-film PZT in sub-millimeter range requires thorough understand on its properties and fundamental behaviors both in theoretical and practical way.

First of all, I developed and improved the microfabrication procedure of PZT thin film microsensor and microactuator. Such procedure includes modified sol-gel preparation, stable fabrication of bottom electrode with proper micro surface texture, microdevice wire bonding and packaging. Meanwhile, during the study I characterized the patterns of thin-film PZT defects. Through parametric study, the degree of bottom electrode porosity is revealed to be the most

critical parameter surpassing others strongly affects the deposited thin-film PZT quality. A second parametric study is simultaneously carried out to ensure the fabrication repeatability of low porous bottom electrode. These contributions not only greatly improve the yield of thereafter lab-fabricated thin-film PZT but also provide an effective way for quick prediction of ongoing PZT fabrication yield based on the judgment of one parameter.

Fabrication of satisfied thin-film PZT could be difficult, however, measuring material piezoelectric properties of just-prepared PZT could be even challenging. Although there are many currently available solutions, they are either complicated or expensive. Most important, they are not applicable for thin-film PZT application. I developed an easy, low cost, but effective method to deal with the thin film piezoelectric coefficient d_{33} through a mini impact hammer approach. Such method is proved to be suitable for both bulk and thin-film PZT. More practically, it can be adopted as a fast way for lab-prepared PZT quality evaluation.

PZT deposition requires a Pt/Ti bi-layer bottom electrode to be annealed retaining condensed structure. The heat treatment will inevitably pull electrode to be porous. It is well known that electrode with pores can greatly affect thin-film PZT material properties. For such reason, I designed and fabricated a special nonporous bottom electrode which inherits the porous electrode surface micro texture but with pores sealed. Although due to the limited experimental results no strong evidence shows new electrode surpasses traditional one in all ways, it contains large effective electrode area by covering the pores earns it better chance to outperform porous electrode.

Keywords: Thin-Film PZT, Bottom Electrode, Porosity, Piezoelectric Coefficient

TALBE OF CONTENTS

Page

Dedication i

Acknowledgments ii

List of Figures v

List of Tables ix

Chapter 1: General Introduction..1

1.1 Background..1

1.2 Advantages of PZT..2

1.3 Challenges..3

1.4 Research Objective..6

Chapter 2: Fabrication of PZT Thin Films Based Microsensors and Microactuators...........9

2.1 Introduction..9

2.2 Substrate..11

2.2.1 Substrate Pretreatment..12

2.2.2 Bottom Electrode Evaporation and Annealing..............................18

2.2.3 Bottom Electrode Porosity Analysis..22

2.3 Sol-Gel PZT..31

2.3.1 Sol-Gel PZT Preparation..32

2.3.2 Sol-Gel PZT Modification..35

2.3.3 Sol-Gel PZT Analysis..39

2.4 Thin-Film PZT..45

2.4.1 Deposition Techniques..46

2.4.2 Sol-Gel Deposition..48

2.4.3 Defect Inspections..49

2.4.4 Parametric Study..56

2.5 Finalization..68

2.5.1 Top Electrode Evaporation and Patterning..68
2.5.2 Backside Deep Wet and Dry Etching..74
2.5.3 Specimen Post Processing..76
2.6 Summary..79

Chapter 3: Measurement of Piezoelectric Coefficient d_{33}..80
3.1 Introduction..80
3.2 Challenges..80
3.3 Theoretical Foundation..84
3.4 Finite Element Analysis for Thick-Film PZT...87
3.5 Experimental Setup and Validation..91
3.6 Applications of d_{33} Measurements to PZT Thin Films...94
3.7 Applications of d_{33} Measurements to PZT Thin Film Microactuators.................97
3.8 Remarks on Residual Stresses..100
3.9 Summary..101

Chapter 4: Studies on Novel-Designed Nonporous Pt/Ti Bi-Layer Bottom Electrode......103
4.1 Introduction..103
4.2 Sample Preparation..105
4.2.1 Pt/Ti Bi-Layer Bottom Electrode...106
4.2.2 PZT Thin Film...111
4.2.3 Au/Cr Bi-Layer Top Electrode...112
4.2.4 Specimen Finalization...113
4.3 Physical Properties Evaluation..114
4.3.1 Elastic Modulus...114
4.3.2 Leakage Current Density..121
4.3.3 Hysteresis Loop (P-E Loop) 122
4.3.4 Piezoelectric Coefficient d_{33}..123
4.4 Summary.. 125

Chapter 5: Conclusions and Future Work..127
5.1 Conclusions.. 127
5.2 Future Works.. 128

Chapter 1
GENERAL INTRODUCTION

1.1 Background

It has been half century, since microdevice or in more specific way Micro-Electro-Mechanical System (MEMS), as a brand new concept, was brought out in front of the sight of human being. In 1959, when Richard Feynman, a well-known physicist, first pointed out the idea, "There's Plenty of Room at the Bottom" regarding to build devices on the micron scale, nobody believed this will come to reality so fast.

Different from molecular nanotechnology or molecular electronics, MEMS is a microdevice that integrates mechanical elements, sensors, actuators, and electronics on a common silicon substrate. Typically, MEMS is made up of components between 1 to 100 µm and its device generally bares a dimension in size from 20 micron to millimeters. For decades, MEMS have gradually proven to be a key enabling technology of developments in areas such as transportation, telecommunications and health care, but the range of MEMS applications cover almost all fields.

The reason that MEMS becomes a strong industry need is all due to its significant advantages. First, MEMS uses IC technology to integrate multiple and more complex functions on a single miniaturized chip to form a monolithic system, which not only improves the ability of internal communication between mechanical and electrical elements, but also minimizes the size of device with no loss of functionality. Second, MEMS can be manufactured through IC batch fabrication, which tremendously reduces the cost and time. Third, microcomponents integrated inside the MEMS make possible the system faster, more reliable and precise, more portable, and less power consumption. Forth, MEMS device can be treated as module, which is easily employed, maintained, and replaced. Fifth, special designed MEMS may create a unique platform to help exploiting the new physics domains.

To make MEMS become practical, one must be fabricated using modified semiconductor device fabrication technologies normally used for making electronics. These include molding and

evaporation, wet (KOH, TMAH) and dry (RIE and DRIE) etching, photolithography, wire bonding, and other technologies capable of manufacturing small devices.

Thanks to the fast growth of fabrication technologies from semiconductor industry and strong market demands of multidisciplinary applications, today, MEMS becomes one of the most excited engineering projects and received intensive research. Most new cars, for example, use tiny accelerometers to detect crashes and initiate airbag inflation [1,2] and MEMS gyroscopes to detect yaw [3]. Companies such as Hewlett-Packard use MEMS to build printer heads for inkjet printers [4]. Cornell University created the world's smallest guitar, a 10-micron-long instrument sculpted of silicon with six strings, each 50 nanometers in diameter [5]. Texas Instruments invented digital micromirror device (DMD) [6,7], a chip integrated in several hundred thousand microscopic mirrors on its surface, for HDTVs and video projectors [8]. Microlaser, a believed versatile optical instrument, was carried out by Sandia National Laboratories for remote sensing (LIDAR, Light Detection And Ranging) [9,10] and molecular spectroscopy [11]. Medical industries recently also bring MEMS devices to medical diagnostic, monitoring tools and analytical equipment. For example, blood microanalyzer [12-14], NanoChip workstation [15-17], implantable insulin pump [18-21], lab-on-a-chip [22-24] are all novel application to successfully interact with individual tissue, cells, or even DNA segments.

Based on the type of use, MEMS can be classified into microsensors, microactuators, and microstructures. To be functional, most of them are designed to work associated with different style of transducers to convert one type of energy to the other. For most microsensors and microactuators, the conversion between mechanical load and electric charge is commonly adopted. This draws a wide interest on researching piezoelectric materials.

1.2 Advantages of PZT

Currently, the most common piezoelectric materials exploited in MEMS applications are Polyvinylidene Fluoride (PVDF), quartz (SiO_2), Zinc Oxide (ZnO), and Lead Zirconate Titanate ($PbZr_xTi_{1-x}O_3$ or PZT). However, their individual advantages and disadvantages create materials application diversities.

PVDF is one type of ferroelectric polymers that becomes more and more popular in medical applications due to its biocompatibility. It can be synthesized from VDF monomer via a free

radical or controlled radical polymerization process. The film formation of PVDF is flexible and can simple adopt conventional processes such as melt casting, solution casting, and spin-coating. Processed PVDF thin films are typically in the non-piezoelectric alpha phase and must be stretched or annealed to turn piezoelectric beta phase. Although PVDF will obtain piezoelectricity when poled in a large electric field, its low piezoelectric coefficient (approximate 10 pC/N) and small energy density make it hard to be applied in microactuator.

When first discovered by Pierre Curie quartz receives advanced studies not only because of its physical and chemical stability but also for its high-quality-factor (Q) and small temperature coefficient of resonant frequency (TCF). These properties are ideal for oscillators and resonators. However, narrow bandwidth of quartz prevents it become useful microsensor.

ZnO, as another type of biocompatible, degradable, and nontoxic material, is found to have potential piezoelectric properties. Recently, it has also been reported to successfully grow ZnO in shape of nanowires, nanorodes, and nanobelts through chemical vapor deposition (CVD) for flexible self-powered nanogenerator [25-27]. Although ZnO can be easily fabricated on any substrate material (crystalline or amorphous, hard or soft) [28], its low dielectric constant [29] inevitably leads to a microactuator with small actuation strength. Moreover, the fabrication cost of such ZnO film still remains challenge.

Unlike its opponents, PZT has many unique properties enabling it potentially outperform other competitors. As a piezoelectric material, PZT receives wide attention all due to its large bandwidth [30-32], high energy density [33], sensitivity, and actuation strength. As a result, PZT based microactuators enable various killing practices, such as micropump and microejector [34,35], atomic force microscopy (AFM) [36], head positioning system of optical and hard disk drive [37,38], and active control system [39]. Moreover, PZT embedded microsensors is adopted for many innovative applications, such as minute hearing aids [40,41], miniaturized diagnostic tools [42,43], energy converter and harvester [44-46], active and passive damage detection [47], and random access memory [48-50].

1.3 Challenges

PZT integrated microdevice is promising, but its development remains challenging. One of the top issues could be thin-film PZT defects.

Currently, the available techniques for fabricating thin-film PZT can be summarized as pulsed laser ablation [51], rf sputtering [52], chemical vapor deposition (CVD) [53], metal-organic decomposition (MOD) [54], screen printing, and sol-gel method, etc. Among these techniques, sol-gel method has been elected to be the most popular one simple because it requires relatively low process temperature [55], can precisely control chemical composition [56], and achieves large area deposition at very low cost. However, our experiment confirms that the use of sol-gel technique on lab basis attempting for a good thin-film PZT quality can always be problematic. In the past few years we continuously suffer from low thin film yield (defect free area is less than 40%) even the process strictly follows the developed classic recipe. There are many reasons causing film defects. Under series process heat treatment, residual stresses, either compressive or tensile stresses, are unavoidably induced in thin-film PZT all due to the PZT crystal structural volume change and its thermal expansion mismatches with bottom electrode. It is reported by some other researchers that compressive residual stress may initiate film delaminate or peel off from the substrate, while tensile residual stress is the reason introducing film surface cracks [57,58]. In addition, after sol-gel spin-coating PZT solvent evaporation accompanied with gel film shrinkage will tend to create bumps and holes/voids on PZT surface. Although repeated experimental results suggest that some fabrication factors are potentially responsible for the thin-film PZT defects, no systematic work has been seriously carried out to characterize these related factors as well as their individual impact on film quality.

Second challenge is the measurement of thin-film PZT material properties. Restricted by the varying process condition, lab-prepared PZT thin films through different fabrication batches often behave various performances. Such performance is known to be dominated by multiple material properties, for instance, elastic Young's modulus E (mechanical properties), film capacitance C and leakage current density J (electrical properties), PZT remnant polarization P_r and coercive field E_c (ferroelectric properties), and piezoelectric coefficient d_{33} (piezoelectric properties). In the past, due to the lack of accurate thin-film property measuring technique, PZT obtained from different batches are ideally considered to be the same. Some of their properties such as elastic modulus and piezoelectric coefficients are either determined based on *a priori* knowledge or courteously borrowed from existing literatures. Since these values are not direct measurements on our PZT thin films, their adoptions in finite element analysis (FEA) model barely help matching the simulation prediction with experimental results. For the case of thin-

film PZT equipped microactuator, displacement simulation of its diaphragm center point consistently has one order of magnitude difference to the real deflection. Previous researcher in the group tried to uncover the key factor that causes the major difference by carefully examining the device cross section geometry, which varies from top electrode size to diaphragm thickness and cavity silicon residue as well. This approach is eventually proved to only provide minor improvement even an optimized geometry setup is achieved. Many evidence pointed out that calibration of thin-film PZT material properties could be the last chance providing the solution. Unfortunately, no thorough work has been done so far to properly address the problem.

The third challenge is the improvement of Pt/Ti bi-layer bottom electrode. To cope with the requirement of thin-film PZT fabrication, just-evaporated bottom electrode needs to be annealed under very high temperature to obtain condensed layer. However, such heat treatment process will inevitably pull the electrode to be porous. Moreover, repeated experiment shows that the degree of annealed bottom electrode porosity is very hard to control and usually adopts various patterns. The patterns could be roughly concluded as nonporosity, low porosity, medium porosity, and high porosity or island. Through long term tracing on electrode pattern, we discovered that the thin-film PZT grown on top of the bottom electrode has inverse surface quality trend to the degree of electrode porosity. As annealed bottom electrode becomes less porous, above sintered PZT thin film likely to receive less defects. When such porosity drops below approximately 20%, PZT has a great chance to become a defect free and smooth layer. However, when spin-coated and sintered on a completely nonporous bottom electrode, those PZT thin film defects suddenly appear and film crack, delamination, or even peels off happens. The observation indicates that proper amount of electrode pores are very necessary. Electrode pores with surface micro texture may function as anchors enabling PZT thin film firmly latch on to it and fight against heat induced residual stress. However, electrode pores can literally influence thin-film PZT behavior by changing its mechanical, electrical, ferroelectric, and piezoelectric properties [59-62]. A reasonable interpretation on the mechanism behind this could be the existence of Ti bonding material fast diffusion through electrode pores into the PZT grain boundary [63-65]. To deal with the problem, a development of special nonporous Pt/Ti bottom electrode is highly desired, on which the surface micro texture is inherited from porous electrode while those pores can be properly covered and sealed.

1.4 Research Objective

The study begins with a thorough understand on thin-film based microdevice fabrication process. Based on such knowledge, the research objective can be projected as follow.

First, modifications of sol-gel PZT preparation. Sol-gel PZT preparation is one of the key processes in chemical solution deposition (CSD) technique. It is reported that the chemistry of the sol-gel solution and the structure of the gel film have strong influence over the properties of the final PZT thin films [66,67]. Although it is suggested that such properties can be modified by proper reagents adding sequence and solution aging [68,69], its heat involved dehydration process for added reagents can physically remove required acidic solvent. Meanwhile, extensive aging may chemically form partial gelation. Both actions are subjected to an increase of sol-gel viscosity and precipitates. Although dehydration time and aging period are preset to be 5 minutes and 3 days respectively, they are quite empirical and very sensitive to unforeseeing situations such as ambient temperature change and variable operation skills from different operators. The modifications are focused on sol-gel PZT dehydration process through use of physical (molecular sieve) and chemical approaches (acetic anhydride). The detail works will be carefully stated in Section 2.3.2. It is quite understood that when such dehydration is free of thermal treatment, the process will become much easier to control and independent of human error.

Second, parametric study on thin-film PZT sol-gel deposition. Based on the available results, defects of sol-gel derived PZT thin films are indentified as bumps, dimples, black dots/holes, cracks, and partial or complete peel off. Many fabrication parameters are targeted for evaluating their individual impact on the film defects. It includes spin-coated sol-gel PZT thin film drying methods, thin film drying temperature and time, age of sol-gel PZT, degree of bottom electrode porosity, and bottom electrode surface wettability. Intensive study reveals that bottom electrode porosity is the most crucial parameter that strongly affect deposited thin-film PZT quality; refer to Section 2.4.4. Comparing with it, the rest parameters only have relatively minor influence. The merit of this work is that it will help us effectively predict the ongoing thin-film PZT fabrication yield simply based on the judgment of one parameter.

Third, parametric study on low porous Pt/Ti bi-layer bottom electrode fabrication. It is known that the degree of bottom electrode porosity is the most critical factor affecting thin-film

PZT quality. How to ensure the repeatability of fabricating low porous bottom electrode becomes necessary. Another parametric studies is thereafter carried out, which includes the evaluation of e-beam selection, electrode deposition thickness, electrode annealing temperature, annealing dwell time, annealing ramp up/down rate, annealing position and posture, and air flow in the furnace. Through investigation, the parameters setting priorities and values are individually studied and empirically adjusted; refer to Section 2.2.3. It is confirmed by the repeated experiment that with adoption of the determined parameter value in right order the deposited and annealed Pt/Ti bi-layer bottom electrode has a stable trend to bear low electrode porosity.

Fourth, development of a simple and effective method for extracting lab-made thin-film PZT piezoelectric coefficients d_{33}. Measuring piezoelectric properties for thin-film PZT is always challenging. Currently, there are many available methods for bulk PZT piezoelectric properties measurement. They frequently adopt two major approaches. The first one is trying to apply an electric field and measure corresponding strain while the second is to apply a known force and measure corresponding charge. These two methods are really innovative and appealing, but they are unfortunately proved to be inapplicable for lab-fabricated thin-film PZT. This is because PZT taking the form of thin film usually provides an insignificant deformation under applying field, which makes it very hard to sense surface displacement. On the other hand, thin-film PZT is extremely vulnerable under a large applying force and very easy to get a film crack, which avoids accurate measurement of generated charge on its surface. To deal with the challenge, we design a simple and low cost d_{33} measuring setup by employing a mini impact hammer, charge amplifier, and an oscilloscope. When hammer tap on the specimen surface with small impulsive force, it will cause a thin-film deformation and generate corresponding surface charge. This electric charge is collected and magnified by charge amplifier and sent to the oscilloscope. In the meantime, bulk PZT at hammer tip will also send a force generated charge to the oscilloscope. The oscilloscope registers peaks of both electric signals. The thin-film PZT d_{33} with substrate effect can be obtained by taking the ratio of two peak values. After calibrated with a theoretical d_{33} that is free of substrate effect, a d_{33} calibration factor α is determined. We assume thin-film PZT is uniform and maintains same quality throughout the whole wafer. When the piezoelectric coefficient d_{33} of another specimen on the same wafer is measured through mini hammer approach, its substrate effect can be compensated by multiplying previously found α and the

real d_{33} can be restored. The developed method is proved to be a simple, efficient, and accurate both on bulk and thin-film PZT applications. When applied to a finite element model of a PZT thin film membrane microactuator, the simulation with the adoption of measured piezoelectric coefficients d_{33} matches well with the real experiment results. The detailed works are discussed in Chapter 3.

Fifth, development of nonporous Pt/Ti bi-layer bottom electrode. During the study, a deposition and annealing procedure for fabricating newly designed nonporous bottom electrode (NBE) with the desired surface texture is presented. Then three-layer PZT stacks are spin-coated and sintered on the NBE alongside with the porous bottom electrode (PBE). To evaluate the performances of PZT thin film on both types of bottom electrodes, physical properties including PZT elastic modulus E, thin film leakage current density J, PZT hysteresis loop (P-E loop), as well as its piezoelectric coefficient d_{33}, are subsequently measured. Based on the special design, the performance of PZT thin film fabricated on NBE is expected to be improved comparing with that on PBE. Unfortunately, such prediction does not eventually well supported by the limited experimental results. However, NBE contains large effective electrode area by covering the pores earns it better chance to outperform PBE; refer to Chapter 4. This requires additional works for further approval.

Chapter 2

FABRICATION OF PZT THIN FILMS BASED MICROSENSORS AND MICROACTUATORS

2.1 Introduction

For several decades, the fabrication of PZT experiences a long term development. Nowadays, it is still one of the hottest research topics and received worldwide attention. Currently the available methods for PZT thin film fabrication are physical deposition (PD) (screen printing), physical vapor deposition (PVD) (electron-beam evaporation, radio frequency (RF) sputtering, magnetron sputtering), chemical vapor deposition (CVD) (metal-organic chemical vapor deposition (MOCVD)), and chemical solution deposition (CSD) (sol-gel process). Among all competitors sol-gel process ranks the most popular technique and is now widely employed. A typical sol-gel derived PZT thin film fabrication process for microsensors and microacturators is illustrated in the Figure 2.1 and can be briefly described in the following sub-steps.

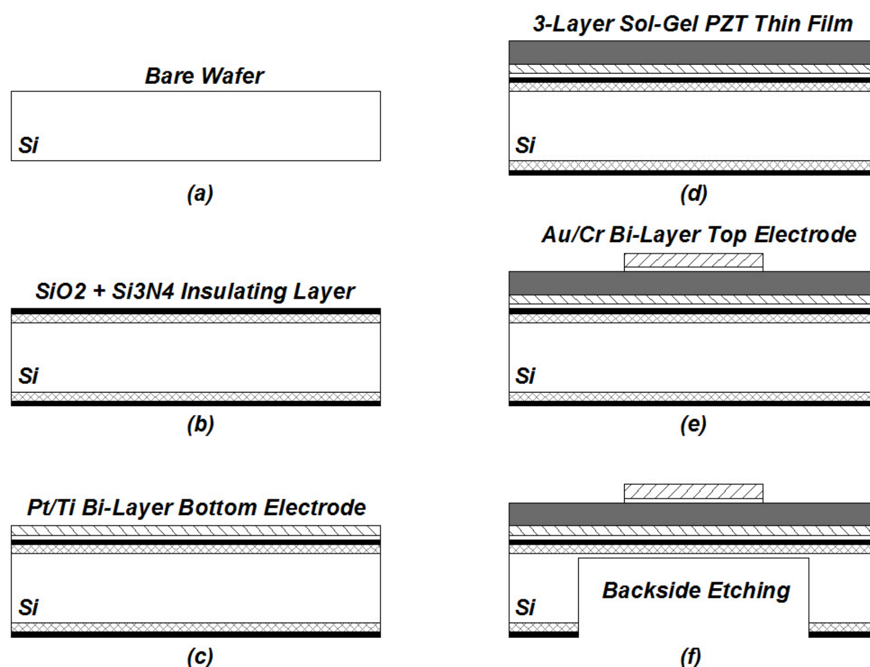

Figure 2.1: PZT thin film fabrication process

First step, a bare boron doped silicon wafer substrate, as sketched in Figure 2.1(a), is deeply cleaned through use of strong acid or base chemical. Second step, the deeply cleaned silicon

substrate is fired to a very high temperature in oxygen enriched ambient for growing silicon oxide insulating layer. Third step, the collected silicon substrate is transferred into low pressure chemical vapor deposition (LPCVD) furnace for growing silicon nitride stop layer; see Figure 2.1(b). Forth step, pretreated silicon substrate undergoes a platinum (Pt)/titanium (Ti) bi-layer bottom electrode deposition in the electron-beam evaporation chamber; see Figure 2.1(c). Fifth step, bottom electrode coated silicon substrate will endure a high temperature annealing process to release the residual thermal stress that induced in the forth step. Sixth step is the preparation of sol-gel PZT. Several major sol-gel PZT processes have been reported, which include alcohol based system [70-73] and acetic acid/water based sol-gel technique [74,75]. In our research, an acetic acid/water based sol-gel technique is pursued and optimized. In sol-gel preparation a mixture of metal alkoxides that contain lead (Pb), zirconium (Zr), and titanium (Ti) nano-clusters is combined with a mixture of alcohol and water. Followed by a hydrolysis and condensation process after the mixing, a sol with a proper viscosity or a gel will be formed [60]. Seventh step, sol-gel PZT is deposited onto previously platinized silicon substrate by either dip-coating or spin-coating. As the solvent of the sol-gel evaporates, cross-linking of individual PZT nano-clusters is promoted and thereafter results in the sol-gel transition. Eighth step, the coated PZT thin layer is sintered at high temperature together with silicon substrate to obtain a densified thin film with desired PZT crystalline phase. Figure 2.1(d) shows that PZT multi-layer stacks can be achieved by simply repeating the coating and sintering steps for several times. Ninth step, a gold (Au)/chromium (Cr) bi-layer top electrode is deposited onto the thin-film PZT and patterned by using either wet etching or liftoff process; see Figure 2.1(e). Final step is to deep-etch from the backside of the silicon substrate via deep reactive ion etch (DRIE) and release the PZT thin film in the form of electrodes sandwiched membrane; see Figure 2.1(f). The quality of the fabricated PZT thin film can be inspected under the optical microscope or scanning electron microscope (SEM). A good PZT thin film usually shows a uniform and crack-free surface and bares the thickness of around 400 nm per single layer.

The production of high quality PZT thin films requires a good understanding on the properties of all involved materials and a solid study on the mechanism of each related process. Generally, these efforts are focusing on four major processes which are silicon substrate preparation, sol-gel PZT preparation, thin-film PZT deposition, and specimen finalization. Starting from next section, more details about these processes will be intensively discussed.

2.2 Substrate

Like many other MEMS, the fabrication processes of PZT thin film derived microsensors and microactuators are adopted from the microelectronics industry and designed to start on a substrate with a layer-stacking technique. The selection and preparation of the substrate could be critical since it exposes a strong effect on the subsequent yield. Due to the good integrability into existing processing technologies, platinized silicon wafer becomes a commonly used substrate. However, in recent research it is reported that the various types of materials such as metallic foil [76], alumina plate [77], glass [78], and flexible plastic film could be decent substitutes. Metallic foil and alumina plate are selected as substrate because of their high thermal and chemical stability. But their drawbacks are obvious. Comparing with platinized silicon wafer, sol-gel derived PZT thin film on metallic foil shows a much lower dielectric permittivity ε_{33} and piezoelectric coefficient d_{33}. This is believed that the lower property profiles are possible due to the interactions between PZT thin film and substrate/electrode [76]. On the other hand, the PZT thin film built on the alumina plate requires a very high sintering temperature (950 °C to 1050 °C) which inevitably causes high film porosity up to 50%. For this reason the PZT thickness has to be increased in order to avoid tremendous drop of piezo-mechanical properties [77]. Glass or flexible plastic film as a substrate is another good trial. During the process, the PZT thin film is first grown on MgO layer by using graphoepitaxial technique inside RF-magnetron sputtering and then glued onto the substrate through transferring process. Although this approach is claimed to reduce the strain and/or constrain effect to the rigid substrate [78], it will potentially lead to a loose film boundary condition and introduce the measurement error.

In the study, we use a silicon wafer as substrate. Start from there the substrate preparation process such as substrate pre-cleaning, silicon oxidation, silicon nitride growth, Pt/Ti bi-layer deposition, and bottom electrode annealing will be demonstrated. In the mean time, the bottom electrode morphology analysis including electrode SEM inspection, electrode porosity control, electrode annealing optimization, and electrode surface wettability test will be discussed.

2.2.1 Substrate Pretreatment

Substrate Selection

The silicon wafers with sizes of 3 inches and 4 inches are two common choices for the MEMS microfabrication research. In our case, 3 inches p-type <100> boron doped silicon wafers are frequently adopted. These commercial available single side polished (SSP) wafers usually bare the conductivity of 1-10 Ω·cm and thickness of 330-432 μm (13-17 mils). Table 2.1 lists the specifications of 3 and 4 inches wafers that purchased from two companies (Silicon Quest International, Inc. and Montco Silicon Technologies, Inc.).

Table 2.1: The specifications of 3 inches and 4 inches wafers

	Silicon Quest International, Inc.		Montco Silicon Technology, Inc.
Thickness (μm)	330 - 432	475 - 575	356 - 406
Diameter (inch)	3	4	3 ± 0.02
Resistivity (Ω·cm)	1 – 10	5 – 10	1 – 5
Type/Orientation	P/Boron <100>	P/Boron <100>	P/Boron <100>
Specification	SSP, 2 SEMI-STD FLATS	SSP, 2 SEMI-STD FLATS	Prime, SEMI-STD FLATS
Part #	-	-	-
Lot #	INV3P01-10TST	INV4P05-10TST	3P01-5SSP-INV
Quantity (pcs/Box)	25	25	25

Substrate Pre-Cleaning

Although sitting in the sealed box, bare silicon wafers may have surface contaminations. For example, the organic and inorganic materials can be introduced when wafers are wire-sawed from silicon boule, doped in the furnace, and packed by the operators. These contaminations could be deeply removed during substrate pre-cleaning process by immersing the wafers in the wet chemical bath such as strong acid or base solution.

As shown in the Table 2.2, a typical procedure is described as follow. First, bare wafers are loaded on a boat and sunk into a Nano-Strip™ (photomask and wafer resist stripping and cleaning agent from Cyantek, Inc.) tank at room temperature for 20 minutes. Nano-Strip™ comprises a stabilized formulation of 90% sulphuric acid (H_2SO_4), 5% peroxymonosulfuric acid (H_2SO_5) and <1% hydrogen peroxide (H_2O_2) compounds. It will react with organic materials and metals. Second, after a 3 cycles of dump rinse in the deionized (DI) water, wafer boat is

transferred into a buffered oxide etch (BOE) tank that contains ammonium fluoride (NH_4F) and hydrogen fluoride (HF) with a 10:1 ratio at room temperature for 2 minutes. BOE is a chemically stable solution designed to maintain a certain pH and a more uniform etching rate. It is used specifically to remove native oxides, a very shallow layer with thickness of approximately 1 nm, which formed on silicon when exposed to air under ambient condition. Third, when dump rinsed in the DI water for 3 cycles, the wafer boat is shifted back to the Nano-Strip™ tank for another 20 minutes and followed by additional 3 cycles of dump rinse. At last, the wafer boat is placed into the chamber of a spin rinse dryer for final cleaning and air dehydration.

Table 2.2: A typical procedure of silicon substrate pre-cleaning process

	Cleaning Bath	Operation	Duration
Step 1	Nano-Strip™	Dip	20 min.
	DI Water	Dump Rinse	3 cl.
Step 2	BOE	Dip	2 min.
	DI Water	Dump Rinse	3 cl.
Step 3	Nano-Strip™	Dip	20 min.
	DI Water	Dump Rinse	3 cl.
Step 4	DI Water	Spin-Rinse & Dry	1 cl.

Silicon Oxidation

Deep-cleaned silicon wafer is previously implanted with boron dopant. According to the equation

$$\rho = \frac{1.305\times10^{16}}{N} + \frac{1.133\times10^{17}}{N\left[1+\left(2.58\times10^{-19}N\right)^{-0.737}\right]} \tag{2.1}$$

where *N* is dopant density, such material impurity will cause silicon wafer to be conductive [79]. Growing a silicon oxide (SiO_2) layer on top of the wafer can build an insulating buffer and prevent the aftermath of the conductivity.

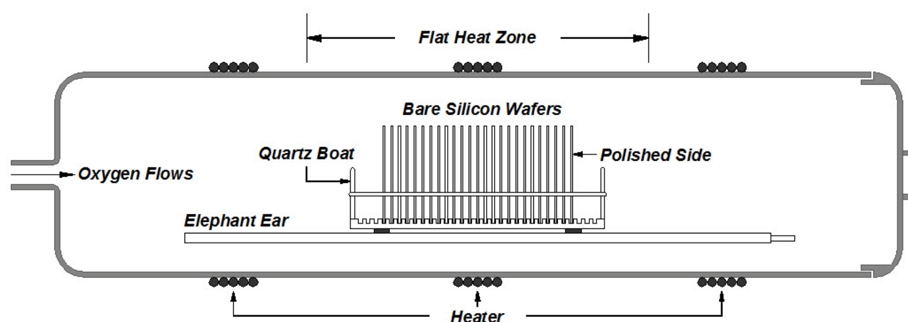

Figure 2.2: Oxygen-enriched silicon oxide fast growth

Table 2.3: Silicon oxidation process recipe

	Step	Seq. Type	Time (min)	Target (°C)	N_2 Sol	N_2 SP	O_2 Sol	O_2 SP	N_2/H_2 Sol	N_2/H_2 SP	N_2BP Sol
1	Initialize	Time to Target	10	30	Open	60.0	Closed	0.0	Closed	0.0	Closed
2	Ramp up	Ramp	10	1050	Open	60.0	Closed	0.0	Closed	0.0	Closed
3	Stabilize	Dwell	10	1050	Open	60.0	Closed	0.0	Closed	0.0	Closed
4	Oxidize	Dwell	180	1050	Open	30.0	Open	10.0	Closed	0.0	Closed
5	Purge	Dwell	10	1050	Open	60.0	Closed	0.0	Closed	0.0	Closed
6	Ramp Down	Ramp	3.0	30	Open	60.0	Closed	0.0	Closed	0.0	Closed
7	End	End	XXX	XXX	Closed	0.0	Closed	0.0	Closed	0.0	Open

Silicon oxidation process is conducted in the oxidation tube furnace (MRL812 atmospheric furnace stack tube 3) from Washington Technology Center (WTC) Microfabrication Laboratory. Two options, dry and wet oxidation, are available for growing the layer. However, comparing with the first option the wet oxidation is much more efficient. When the oxygen (O_2) flows through the heated (95 °C) DI water bubbler, it dissolves the water into the process gas and injects the vapor into the oxidation tube furnace. This will provide an oxygen-enriched ambient for silicon oxide fast growth. In the mean time, as shown in the Figure 2.2, bare wafers (25 wafers per process batch) are vertically lined up on the quartz boat in a row with polished side facing towards the tube entrance. When the tube furnace is preheated to the process temperature, literally 1050 °C, the boat is gradually slid inside the middle of the tube where the uniform temperature produces a flat heat zone (FHZ). It usually takes up to 3 hours for growing the silicon oxide to around 500 nm. Referring to the Table 2.3, during the whole process the furnace temperature and gas flow are controlled by a computer through preprogrammed SpecView software. After overnight furnace cooling, oxidized wafers with pink color will be collected and inspected under ellipsometer or Nanospec thickness measurement system. A five-

spot inspection method illustrated in Figure 2.3 is adopted for silicon oxide thickness verification. From Table 2.4 we continuously observe that the thicknesses of the oxide layer measured at surrounding edge of the wafer are always thicker than that obtained at the center location. The possibility could be high that the oxidation process gas in the tube furnace can hardly be evenly distributed under the laminar flow.

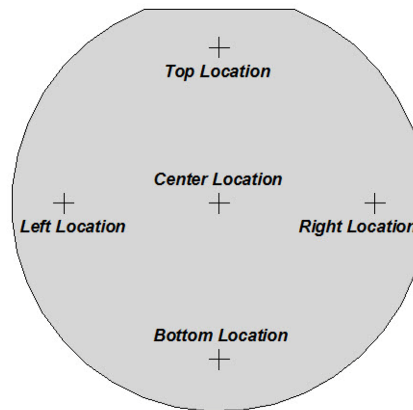

Figure 2.3: Five-spot inspection for silicon oxide thickness verification

Table 2.4: Silicon oxide thickness five-spot inspection data

Batch No.	Wafer No.	Top (nm)	Bottom (nm)	Center (nm)	Left (nm)	Right (nm)
X-002	1	542.7	541.1	539.5	571.1	547.0
	13	540.6	534.7	535.6	561.0	537.8
	25	524.8	528.7	526.2	536.5	530.8
X-003	1	530.9	544.9	535.7	540.9	541.1
	13	553.2	574.8	555.5	555.5	552.3
	25	542.6	562.6	552.7	551.1	548.3
X-008	1	582.8	583.7	581.6	593.6	586.5
	13	587.2	576.7	577.2	581.3	591.0
	25	580.7	595.5	585.7	591.2	591.9

Silicon Nitridation

Silicon nitride (Si_3N_4 or SiN_x) is a chemical compound of silicon and nitrogen. It is reported by many researchers that silicon nitride is a hard ceramic having mechanical strength over a broad temperature range [80-82], moderate thermal conductivity [83,84], low coefficient of thermal expansion [85,86], moderately high elastic modulus [80-82,85], and high fracture toughness [80-82]. In addition, it is noticed that silicon nitride layer is repeatedly used as a popular insulator [87,88] and chemical barrier in silicon-based MEMS device to electrically

isolate different structures or as an etch mask in bulk micromachining. Moreover, as a passivation layer silicon nitride is superior to silicon oxide, as it is a significantly better diffusion barrier against water molecules and sodium ions, which are two major sources of corrosion and instability in micro electro-mechanical systems [89,90]. For these reasons, it is necessary to add a silicon nitride layer right above the silicon oxide to enhance the substrate mechanical and chemical behavior.

There are many ways to grow silicon nitride. One of them is through a simple direct chemical reaction. Silicon wafer is burnt in nitrogen ambient at temperatures between 1300 and 1400 °C and silicon nitride can be formed by following equation

$$3Si(s)+2N_2(g)\rightarrow Si_3N_4(s) \quad (2.2)$$

Other widely employed methods are low pressure chemical vapor deposition (LPCVD) and plasma enhanced chemical vapor deposition (PECVD). LPCVD is a technology depositing silicon nitride at a rather high temperature in a horizontal tube furnace, while PECVD can work at a rather low temperature under vacuum conditions. Both technologies are attractive because of their high efficiency. For example, LPCVD has a nitride deposition rate of 1.5-2 nm/min while PECVD can achieve 10-30 nm/min [91]. All makes these possible should credit the following synthesis equations

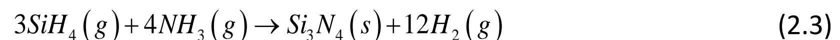

$$3SiH_4(g)+4NH_3(g)\rightarrow Si_3N_4(s)+12H_2(g) \quad (2.3)$$

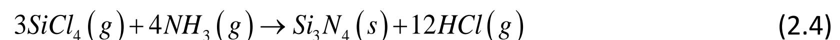

$$3SiCl_4(g)+4NH_3(g)\rightarrow Si_3N_4(s)+12HCl(g) \quad (2.4)$$

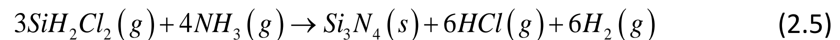

$$3SiH_2Cl_2(g)+4NH_3(g)\rightarrow Si_3N_4(s)+6HCl(g)+6H_2(g) \quad (2.5)$$

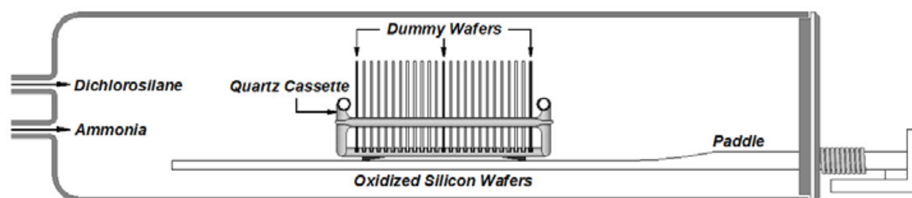

Figure 2.4: Silicon nitridation process

We operate the silicon nitridation process on LPCVD (tube furnace No.3) in WTC Microfabrication Laboratory. First, the processing wafers (25 wafers per process batch) are loaded into a quartz cassette and put on the center of a paddle. For thickness inspection purpose, bare dummy wafers are inserted in the middle and both ends of the cassette with one at each location, see Figure 2.4. Second, when paddle is transported into the tube furnace by timing belt, the tube door will be closed and sealed simultaneously. Third, following equation (2.5), dichlorosilane (DCS, SiH_2Cl_2) and ammonia (NH_3) are imported into the tube furnace with proper mixing ratio (ex. in our case the ratio is 5:1). Controlled by a computer, the deposition pressure will drop to 300 mtorr, meanwhile the processing temperature will rise up to 825 °C. Finally, after approximately 40 minute, the deposition of silicon nitride with thickness around 200 nm is accomplished. A typical nitrided silicon wafer should reflect green color. Same inspection instrument and method that used on silicon oxide are acquired for silicon nitride thickness verification. The measurements are shown in Table 2.5. Under Nanospec system, we are aware that the nitride thicknesses of wafers located in the front of quartz cassette are most likely thicker than those of substrates sit in the back. One possible reason is that the mixing chemicals flow in from the front end of the furnace and then fill up the whole tube which eventually leads to a different chemical concentration and reaction rate.

Table 2.5: Silicon nitride thickness five-spot inspection data

Batch No.	Wafer No.	Top (nm)	Bottom (nm)	Center (nm)	Left (nm)	Right (nm)
N-002	1	237.9	219.0	218.1	233.9	229.9
	13	216.3	198.7	240.6	300.5	210.5
	25	230.7	216.1	230.0	227.7	236.0
N-003	1	219.7	208.6	219.2	217.4	217.4
	13	199.8	188.1	189.4	197.6	197.2
	25	217.8	201.6	202.0	211.9	209.0
N-008	1	228.0	217.4	227.6	226.4	224.5
	13	221.3	204.5	206.6	219.5	213.5
	25	238.4	218.4	209.0	232.4	227.6

Although it has higher resistivity and dielectric strength than most insulators commonly available in microfabrication (1016 Ω·cm and 10 MV/cm, respectively) [91], It is notable that silicon nitride deposited by LPCVD will experience strong tensile stress. Such stress could be dramatically reduced in PECVD technology by adjusting deposition parameters.

2.2.2 Bottom Electrode Evaporation and Annealing

Bottom Electrode (Pt/Ti Bi-Layer) Evaporation

In the application of MEMS microsensors and microactuators, Lead Zirconate Titanate Oxide ($PbZr_xTi_{1-x}O_3$ or PZT) becomes most widely studied ferroelectric material. PZT requires electric contact from electrodes to be functional. Recently, it is reported that electrodes are found to play an important role in the performances of PZT [92-94] including remnant polarization (2*Pr*), cycles of fatigue, and leakage current. In order to maintain a high PZT performance and reliability, researchers have investigated many types of bottom electrodes such as platinum (Pt) [95-97], ruthenium oxide (RuO_2) [98,99], strontium ruthenate ($SrRuO_3$) [100-102], calcium ruthenate ($CaRuO_3$) [102], iridium (Ir) [103], iridium oxide (IrO_2) [104,105], lanthanum nickel oxide ($LaNiO_3$) [101,106], and indium tin oxide (ITO) [107] to fulfill such requirements. However, among all of them a combination of Pt/Ti bi-layer is widely adopted. As a standard electrode material, Pt has an outstanding compatibility during PZT fabrication since it possesses a high conductivity under electric field and excellent stability in high temperature oxidation. Moreover, Pt outperforms its competitors by dominating the PZT crystallographic orientation in <111> to ensure higher piezoelectric coefficients and dielectric constant. To improve bonding between Pt and silicon substrate, a Ti thin layer is frequently selected for promoting adhesion [108,109]. The formation of Pt/Ti bi-layer electrode is usually realized by standard metallization techniques such as sputtering and evaporation.

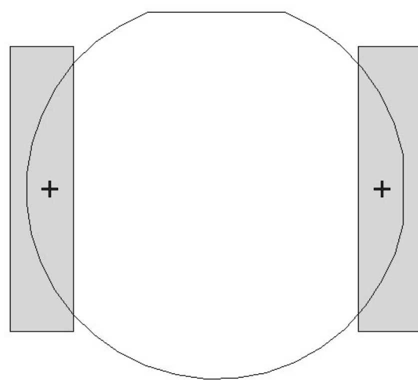

Figure 2.5: Alignment mark covered by Kapton® mask tapes

In the study, we take advantage of E-Beam evaporator from WTC for bottom electrode deposition, not only because of its fast deposition rate but also due to its less raw material

consumption. Deposition material Pt (99.99% pure, 1/8 inch dia. × 1/8 inch) and Ti (99.995% pure, 1/8 inch dia. × 1/8 inch) pellets are both purchased from Kurt J. Lesker® Company. A typical procedure can be described as follow. First, pretreated wafers are cleaned by Nano-Strip™ bath followed by dump rinse and dry process. Second, Kapton® mask tapes (Kapton® Polyimide Film, made by DuPont Company) are applied on both edges of the wafer as shown in Figure 2.5 to cover the alignment mark. Third, the wafers are placed face down on a substrate planetary inside evaporator (CHA E-Beam Model 822 <Au alloy> or NRC E-Beam Model 3117 <Al Alloy>). Forth, the evaporation chamber is pumped down to 3.0×10^{-6} Torr to initiate the deposition process. The Ti and Pt layers are sequentially deposited with empirical target thicknesses of 50 nm (under rate of 0.1 nm/s) and 100 nm (under rate of 0.3 nm/s), respectively. It is suggested that both E-gun sweep speed and crucible heating power need to be carefully tuned for a good final electrode quality. Improper E-gun sweep speed will either cause an underheated deposition material or increase the risk of melting down the crucible. The former interferes with the deposition rate while the latter brings the metal contamination. Unsuited heating power, especially refer to a fast power increment, will overheat the shell of the deposition material but leave a cold core inside. Such uneven heating up eventually causes metal burst and non-uniform electrode. Extreme case may even cease the deposition process. This typically occurs to the material with very high melting point such as Pt (1768 °C). To avoid the situation, longitudinal and lateral E-gun sweep frequencies are usually preset to 3 Hz and 2 Hz, respectively. Table 2.6 lists the empirical crucible heating and deposition parameters for Ti and Pt while Figure 2.6 illustrates the heating profiles for both materials.

Table 2.6: Empirical crucible heating and deposition parameters for Ti and Pt

Metal	Step 1: Melting			Step 2: Boiling			Step 3: Deposition	
	Melting Point (°C)	Rise Time (min:sec)	Soak Time (min:sec)	Boiling Point (°C)	Rise Time (min:sec)	Soak Time (min:sec)	Thickness (nm)	Time (min:sec)
Ti	1668	2:00	1:00	3287	1:00	1:00	50	8:20
Pt	1768	3:00	2:00	3825	2:00	1:00	100	5:33

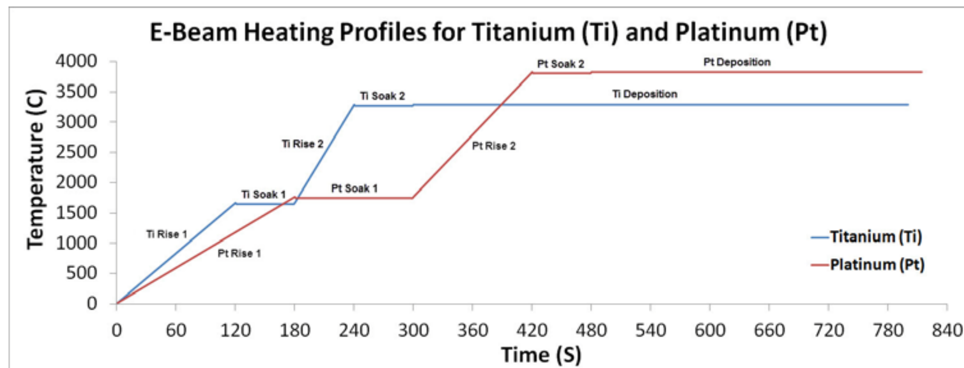

Figure 2.6: Ti and Pt heating profiles during E-Beam evaporation

Bottom Electrode Annealing

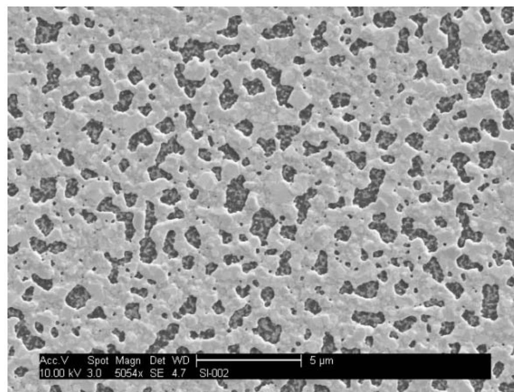

Figure 2.7: SEM picture of typical annealed Pt/Ti bottom electrode

After bottom electrode deposition, the Pt/Ti bi-layer electrode always requires to be annealed under high temperature to get a condensed structure with rough micro surface; see Figure 2.7. Bottom electrode annealing process is conducted in general purpose tube furnace (MRL812 atmospheric furnace stack tube 4) from WTC. As shown in the Figure 2.8, several platinized silicon wafer substrates are laid down one next to the other on the quartz elephant ear in the tube furnace at 800 ˚C for 30 to 60 minutes. A condensed Pt/Ti structure can prevent bottom electrode from peeling off during PZT thin film deposition, while a rough micro surface will make sure PZT thin film firmly anchor into the bottom electrode.

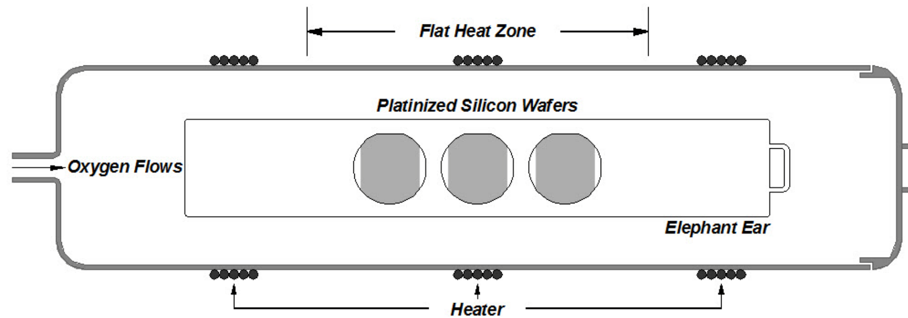

Figure 2.8: Top view of platinized silicon wafers under annealing process

Annealing process is necessary for creating surface microstructure, but it also raises a big challenge, that is high annealing temperature can easily introduce porosity to the Pt/Ti bottom electrode and thereafter affect PZT thin film mechanical, electrical, and ferroelectric properties.

Some researchers suggest that this could be avoided if the bottom electrode is deposited on the preheated silicon substrates [110,111]. When Pt/Ti bi-layer is deposited at low temperature, a tremendous compressive residual stress in Pt film is pre-stored, this is due to Pt layer possesses a very small grain size and has a tendency to re-crystallize during any subsequent thermal treatment [112]. In the later high temperature thermal treatment in oxygen ambient, such stress can be relaxed and become tensile by shrinkage of the film thickness and formation of hillocks and bumps [113,114]. Upon the further high temperature thermal annealing, the Pt hillocks population and grain size will increase [115] and finally yield a porous Pt with decreased density [116,117].

Other researchers, however, indicate that porous bottom electrode due to annealing may be the result of a strong Ti diffusion into the Pt film generating an additional compressive stress [118]. During the annealing, high temperature enhances oxidation of the intermediate Ti layer and triggers its migration into/through Pt [119] followed with an oxidation in the Pt grain boundaries. This will either result in the depletion of Ti bonding material and subsequent loss of Pt adhesion or cause the formation of TiO_{2-x} in the platinum and ultimate encapsulating TiO_2 film on top of Pt [111]. The extensive TiO_2 formation with a low dielectric constant can drastically reduce the net charge density of the device [112]. It is proposed that a modification of Pt/Ti bi-layer deposition and annealing sequence can effectively eliminate the problems [120]. For example, Ti layer is first annealed right after its deposition and then Pt is coated followed with second annealing.

In order to obtain nonporous Pt/Ti bi-layer bottom electrode, we put much effort on trying to follow above two ideas. Unfortunately, it turns out that both methods are currently not applicable to our fabrication. First, due to the equipment limitation from WTC, we are unable to heat the silicon substrate during electrode deposition and will inevitably suffer from a Pt/Ti bi-layer with residual thermal stress. Second, although it reveals that pre-oxidized Ti layer has a weak tendency to diffuse into or react with Pt during the final electrode annealing, we discovered that such bottom electrode can hardly survive (cracks or peels off) from conventional sol-gel PZT rapid thermal anneal (RTA) treatment; see Figure 2.9. For this reason, the design of a stronger nonporous Pt/Ti bottom electrode with proper surface microstructure is required. This special research will be discussed in Chapter 4.

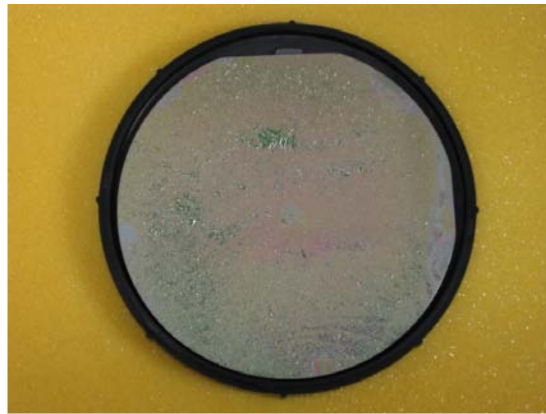

Figure 2.9: Pt/Ti bottom electrode is peeled off after sol-gel PZT RTA Treatment

2.2.3 Bottom Electrode Porosity Analysis

Porosity analysis is a micro level study on Pt/Ti bi-layer, which mainly focuses on the degree of porosity on annealed bottom electrode caused by high temperature treatment. Under SEM, each annealed bottom electrode required to be inspected at nine spots for porosity analysis; see Figure 2.10. As mentioned in previous section, Pt/Ti bi-layer tends to be pulled porous during annealing process. Besides stress relaxation and Ti diffusion, other possible factors such as E-Beam selection, electrode thickness, annealing temperature, annealing time, annealing ramp up/ramp down rate, annealing position and posture, and air flow in the furnace could all play important roles in the degree of porosity on final annealed electrode. Unveiled by SEM inspection, four major electrode porosity degrees such as none porosity (imperforation), low porosity, medium porosity, and high porosity (island shape) are successfully discovered.

Repeated experiments also imply that sol-gel PZT fabricated on the bottom electrode with different morphology has a very stable trend to produce thin film in various qualities. Although the mechanism causing such varieties still remains unclear, one rational guess is that Pt/Ti metallization has a strong influence to the morphology and orientation of PZT thin film since Pt/Ti interface properties mainly affect PZT nucleation-and-growth process. Parametric study, however, provides another possibility to correlate the individual tuning factor with electrode porosity. The database generated by such correlation will serve as a guideline to sort out the factor optimization priority and help projecting the PZT yield tendency.

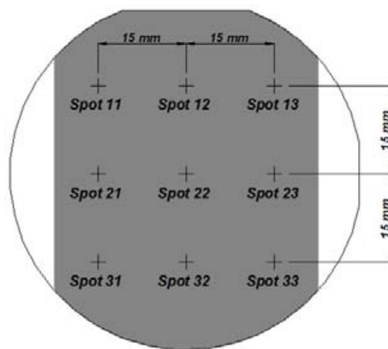

Figure 2.10: Nine-spot inspection array for morphology analysis

<u>E-Beam Selection</u>

In WTC Microfabrication Laboratory, two different evaporators (CHA E-Beam Model 822 <Au alloy> and NRC E-Beam Model 3117 <Al Alloy>) are deployed for electrode deposition. By accident, we find that the selection of E-Beam evaporator could strongly interfere with the bottom electrode annealing results. In the study, four wafers are evenly divided into two testing groups and platinized in CHA and NRC, respectively. Same Pt/Ti bi-layers are deposited on all four wafers but annealed separately according to setup in Table 2.7. The results show that annealing time for electrodes from NRC must be reduced for obtaining similar electrodes porosity to that from CHA; see Figure 2.11. This draws our attention to the deposition mechanism in two evaporators. First, E-gun power in NRC is much lower than that in CHA since NRC holds less evaporation material in a smaller crucible while CHA takes a larger crucible with more material. Second, NRC is designed to maintain high vacuum by using liquid nitrogen filled diffusion pump. The liquid nitrogen effectively cools down the pump oil. However, it may also decrease the temperature inside the deposition chamber. CHA, instead, deploys turbo

molecular pump which results a much higher chamber temperature. These factors inevitably lead to a chamber temperature variance in two evaporators and induce different thermal residual stresses in the deposited Pt/Ti bi-layer.

Table 2.7: Empirical setups for different E-Beam selection and annealing time

Wafer No.	E-Beam Type	Ti Thickness (nm)	Pt Thickness (nm)	Ramp up Time (min.)	Target Temp. (°C)	Dwell Time (min.)	Ramp down Time (min.)	Annealing Posture
SI-002	CHA (Au)	50	100	60	800	60	60	Flat
SI-003	CHA (Au)	50	100	60	800	60	60	Flat
SI-219	NRC (Al)	50	100	60	800	40	60	Flat
SI-220	NRC (Al)	50	100	60	800	40	60	Flat

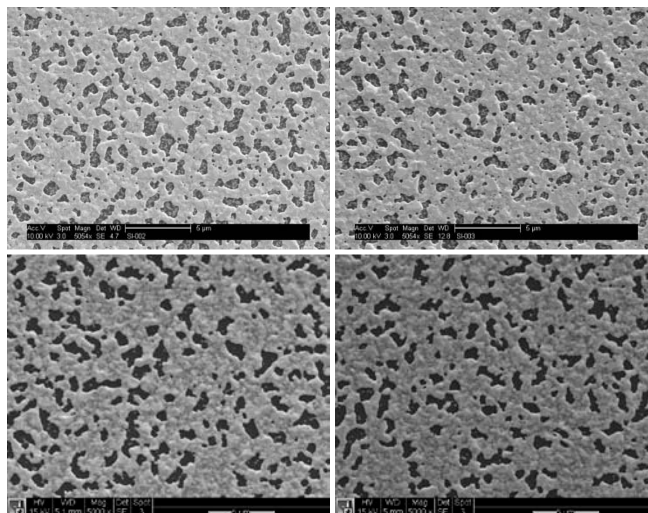

Figure 2.11: SEM pictures of Pt/Ti porosity after annealing. Electrodes on top (SI-002, SI-003) are deposited in CHA. Those on bottom (SI-219, SI-220) are deposited in NRC.

<u>Electrode Thickness</u>

In this study, we produce two platinized wafers with different Pt/Ti bi-layer thicknesses; see Table 2.8. After going through same annealing process, the thicker Pt/Ti bi-layer becomes porous but the thinner one turns island; see Figure 2.12. This is because Pt, Ti, or Pt/Ti alloy may be partially melted under considerably high temperature and possesses certain creeping mobility. Driven by the surface tension, Pt/Ti tends to reduce surface area to volume ratio by shrinking layer thickness and forming near-spherical shape. Comparing with thinner Pt/Ti, the thicker bi-layer has more material, which provides more room to prevent it from being severely pulled.

Table 2.8: Empirical setups for different Electrode Thickness

Wafer No.	E-Beam Type	Ti Thickness (nm)	Pt Thickness (nm)	Ramp up Time (min.)	Target Temp. (°C)	Dwell Time (min.)	Ramp down Time (min.)	Annealing Posture
SI-004	CHA (Au)	50	100	60	800	60	780	Flat
SI-184	CHA (Au)	25	100	60	800	60	780	Flat

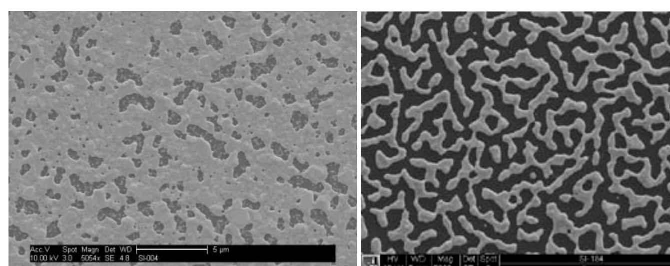

Figure 2.12: SEM pictures of Pt/Ti porosity after annealing. Electrode in the left (SI-004) is thicker than that in the right (SI-184).

Annealing Temperature

Annealing temperature (target temperature) determines the metal tensile strength. It is reported that Ti loses its strength when heated above 430 ˚C [121], while Pt with purity 99.5% has sudden drop in the value of tensile strength in the temperature interval of annealing of 650-680 ˚C [122]. We test two identical platinized wafers under different annealing temperatures; see Table 2.9. The results in Figure 2.13 confirm the prediction that higher temperature much easier forms a porous Pt/Ti bottom electrode. The explanation is that extensively heated Pt/Ti bi-layer has much lower material strength to fight with pre-stored residual stress that induced by electrode deposition.

Table 2.9: Empirical setups for different annealing temperature

Wafer No.	E-Beam Type	Ti Thickness (nm)	Pt Thickness (nm)	Ramp up Time (min.)	Target Temp. (°C)	Dwell Time (min.)	Ramp down Time (min.)	Annealing Posture
SI-207	NRC (Al)	50	50	60	800	15	60	Flat
SI-208	NRC (Al)	50	50	60	700	15	60	Flat

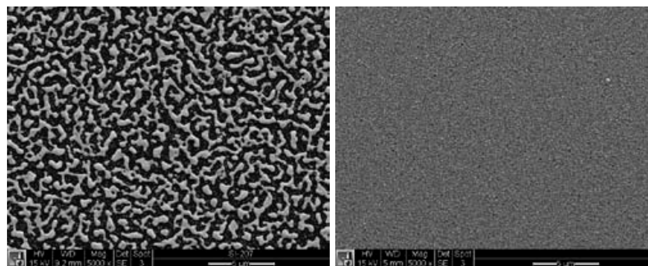

Figure 2.13: SEM pictures of Pt/Ti porosity after annealing. Left electrode (SI-207) is annealed under 800 °C while the Right one (SI-208) is annealed under 700 °C.

Annealing Time

Annealing time (dwell time) is the maximum period for Pt/Ti bi-layer condensation. Table 2.10 lists different annealing time for two identical electrodes. Under the same annealing temperature, longer dwell time allows more electrode residual stress to be fully released and form irreversible island pattern; see Figure 2.14.

Table 2.10: Empirical setups for different annealing time

Wafer No.	E-Beam Type	Ti Thickness (nm)	Pt Thickness (nm)	Ramp up Time (min.)	Target Temp. (°C)	Dwell Time (min.)	Ramp down Time (min.)	Annealing Posture
SI-193	CHA (Au)	50	100	60	800	10	60	Flat
SI-198	CHA (Au)	50	100	60	800	30	60	Flat

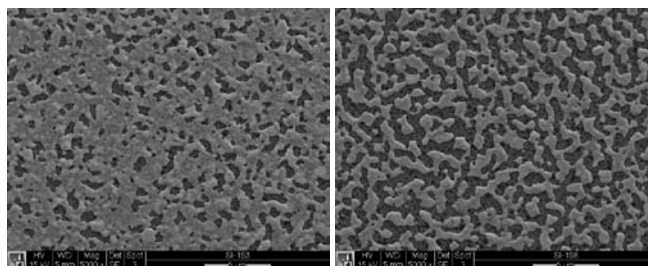

Figure 2.14: SEM pictures of Pt/Ti porosity after annealing. Electrode in the left (SI-193) is annealed for 10 min. and that in the Right (SI-198) is annealed for 30 min.

Annealing Ramp up/Ramp down Rate

Ramp up/ramp down rate refers to the heating increment for reaching the target annealing temperature. Not like RTA, annealed wafer should be heated up with the furnace followed by a furnace cooling. Two empirical setups listed in Table 2.11 are used for comparison purpose. Both setups adopt same ramp up rate, annealing temperature and annealing time. However,

first setup using lower ramp down rate provides additional effective annealing time and leads to a porous Pt/Ti; see Figure 2.15. Instead, second setup is a modified recipe that adopts a higher ramp down rate. This enables a quick furnace temperature drop and retains a relatively intact electrode pattern; see Figure 2.16.

Table 2.11: Empirical setups for different annealing ramp down rate

Wafer No.	E-Beam Type	Ti Thickness (nm)	Pt Thickness (nm)	Ramp up Time (min.)	Target Temp. (°C)	Dwell Time (min.)	Ramp down Time (min.)	Annealing Posture
SI-012	CHA (Au)	50	100	60	800	60	780	Flat
SI-008	CHA (Au)	50	100	60	800	60	60	Flat

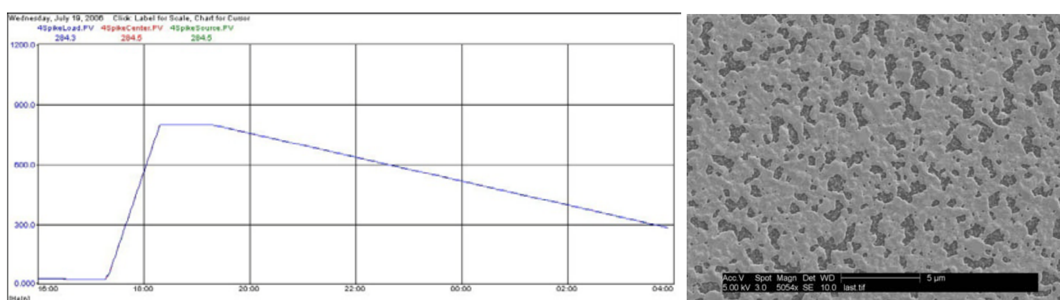

Figure 2.15: Temperature vs. time graph is shown in the left where a low ramp down rate is adopted. Right picture is the electrode porosity for Pt/Ti through left annealing setup.

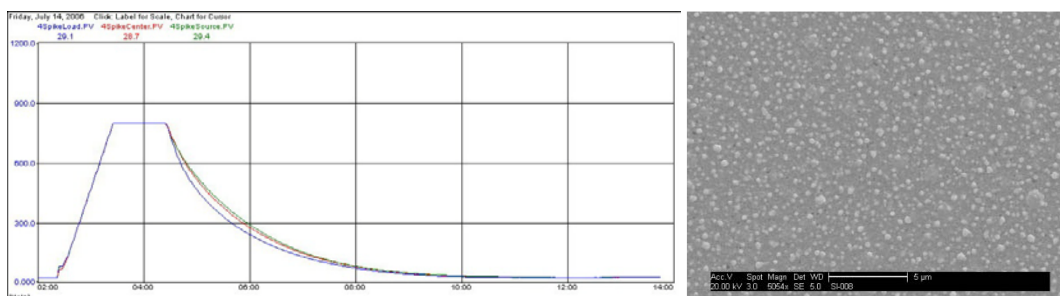

Figure 2.16: Temperature vs. time graph is shown in the left where a high ramp down rate is adopted. Right picture is the electrode porosity for Pt/Ti through left annealing setup.

<u>Annealing Position and Posture</u>

In the study, we repeatedly find that the position and posture of wafer annealing in the tube furnace tremendously affect the finally annealing results. Although ideally the temperature should be three-dimension evenly distributed inside the tube, the real case indicates a big variation from location to location, even in the tube flat heat zone. During the experiment, we

carry out two sets of wafers, three per set, for comparative study. First round, one set of wafers is vertically standing in the quartz boat; see Figure 2.17. Second round, another set is laid down one next to the other on the quartz elephant ear; refer to Figure 2.8. The annealing setups for both rounds are identical; see Table 2.12. Six wafers are individually inspected under SEM. For the first set, all three wafers only show Pt/Ti porosity near surrounding edges but leave the centers untouched; see Figure 2.18. On the contrary, the second set shows pretty similar electrode porosity patterns throughout the entire wafers; see Figure 2.19.

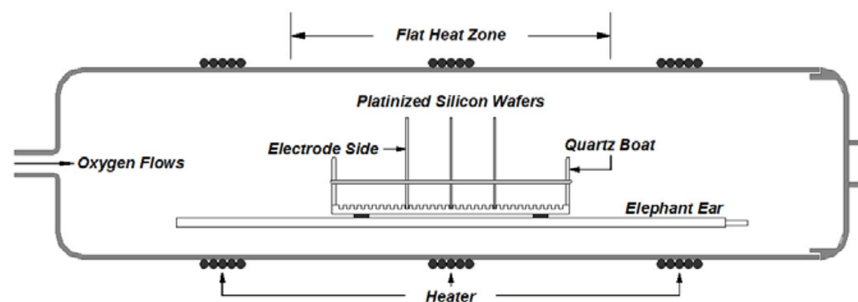

Figure 2.17: Side view of platinized silicon wafers during vertical annealing

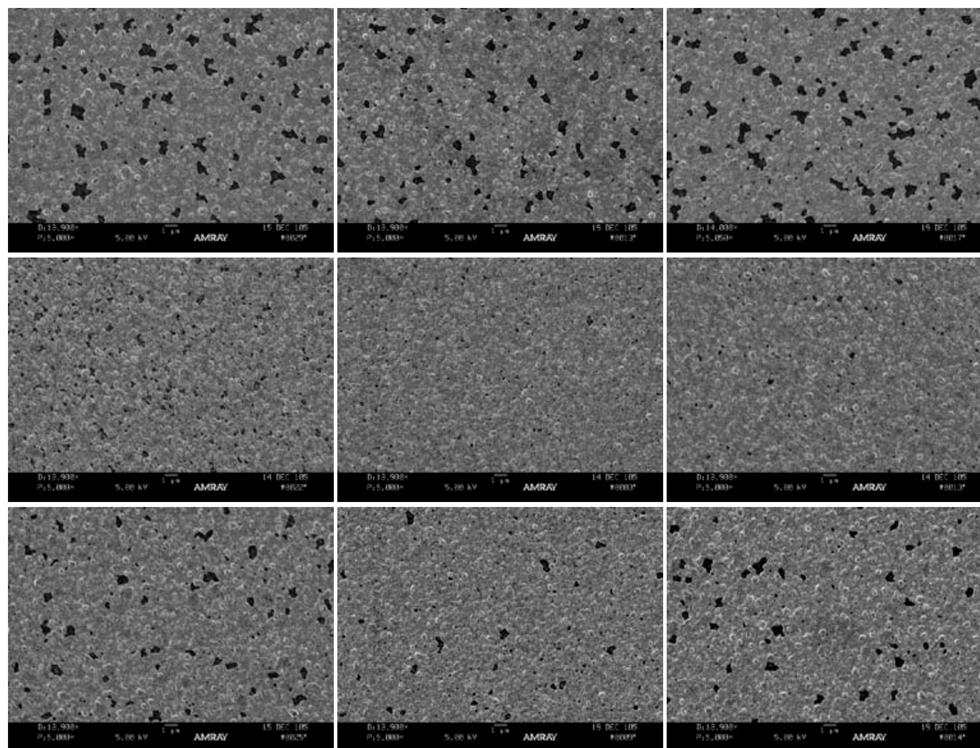

Figure 2.18: SEM pictures of Pt/Ti porosity after vertical (stand) annealing. Columns from left to the right represent annealed electrodes on wafer SI-037, SI-038, and SI-039, respectively. Rows from top to bottom are inspections at spot 12, 22, and 32, respectively.

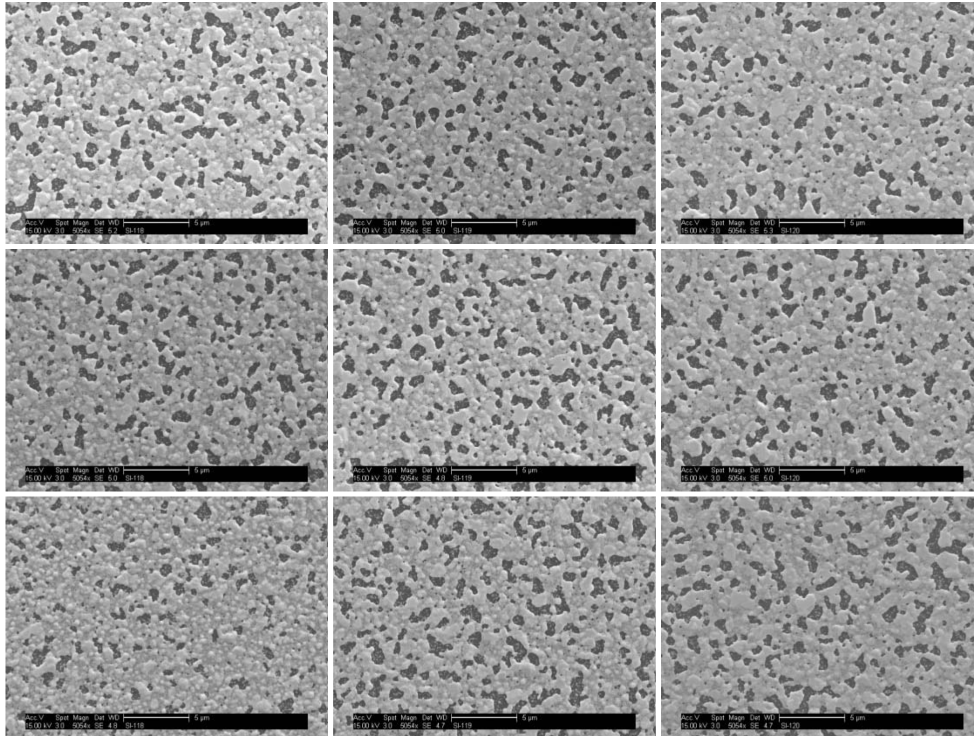

Figure 2.19: SEM pictures of Pt/Ti porosity after laid down (flat) annealing. Columns from left to the right represent annealed electrodes on wafer SI-118, SI-119, and SI-120, respectively. Rows from top to bottom are inspections at spot 12, 22, and 32, respectively.

Air flow

Unexpected air flow introduced by tube temperature difference can hardly be avoided in the capped furnace. Uneven Pt/Ti porosity caused by such insignificant air flow is usually observed. We conduct two identical platinized wafers undergoing annealing processes listed in Table 2.13. It happens to find that macro views of two annealed electrodes bare different morphologies; see Figure 2.20. It should be pointed out that different annealing time and ramp down rate could not be reasons causing such pattern variances, since they are the factors that affect the porosity on the whole electrode simultaneously. Micro views of electrode porosities inspected in different locations are shown in Figure 2.21. It clearly demonstrates the temperature drop along the path of circulating air flow.

Table 2.13: Empirical setups for different annealing time and ramp down rate

Wafer No.	E-Beam Type	Ti Thickness (nm)	Pt Thickness (nm)	Ramp up Time (min.)	Target Temp. (°C)	Dwell Time (min.)	Ramp down Time (min.)	Annealing Posture
SI-197	CHA (Au)	50	100	60	800	60	30	Flat
SI-199	CHA (Au)	50	100	60	800	30	60	Flat

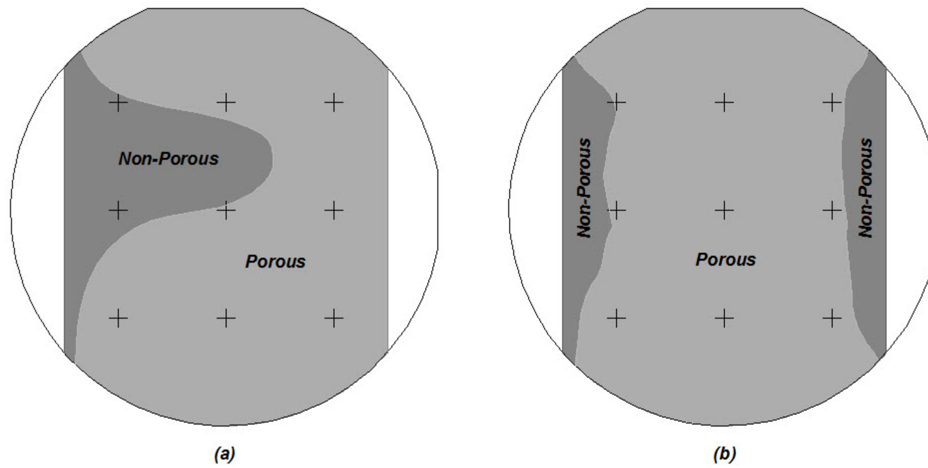

Figure 2.20: (a) and (b) are macro views of electrode porosity for SI-197 and SI-199.

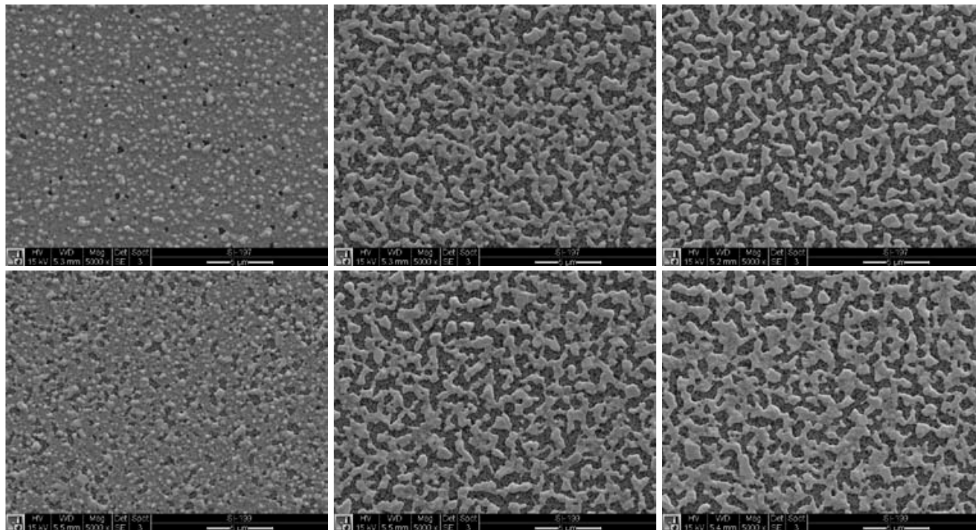

Figure 2.21: Micro views of Pt/Ti porosity after annealing. Top and bottom rows represent annealed electrodes on wafer SI-197 and SI-199, respectively. Columns from left to right are inspections at spot 11, 12, and 13, respectively.

Conclusion

Generally, Pt/Ti bi-layer bottom electrode deposition and annealing is a very important step. It directly determines the thereafter PZT thin film quality deposited on it and must be paid special attention. Through long term investigation, setting priorities and values of all annealing factors for Pt/Ti electrode are individually studied and empirically tuned; refer to Table 2.14. By adopting these adjusted annealing factors in right order, annealed Pt/Ti bi-layer has a stable trend to bear low electrode porosity while maintaining proper surface microstructure. Repeated experiments also confirm that chances are good that sol-gel PZT spin-coated on low porous Pt/Ti electrode will eventually yield high quality thin-film PZT. More details about the relationship between bottom electrode porosity and will PZT thin film quality be further discussed in Section 2.4.4.

Table 2.14: Empirical setting priorities and base values of annealing factors

Priority	1st	2nd	3rd	4th	5th	6th	7th
Factor	E-Beam Selection	Annealing Position and Posture	Electrode Thickness	Annealing Temperature	Annealing Time	Annealing Ramp up/Ramp down rate	Air Turbulence
Base Value	NRC (Al)	Flat Heat Zone Flat	Ti: 50 nm Pt: 100 nm	800 °C	30 Min.	60 °C/Min. 60 °C/Min.	N/A

2.3 Sol-Gel PZT

PZT can be prepared through many ways, among which sol-gel method is widely adopted. It becomes so popular is because such method possesses many unsurpassable privileges. First, sol-gel PZT that formed in terms of colloid solution can be prepared in advance with precise control of required chemicals. Second, sol-gel PZT takes advantage of chemical solution deposition (CSD) to yield desired thin film composition through transferring excellent controlled stoichiometric ratio from coating solution [123]. Third, thickness of thin film deposited by sol-gel PZT can be easily adjusted using spin-coating method. Fourth, low production cost enable sol-gel PZT be deployed for large area thin film fast deposition [124].

Although alcohol based and acetic acid/water based systems are two common sol-gel PZT preparation techniques, our experiment follows the classic recipe of preparing acetic acid/water based sol-gel PZT mentioned in doctoral dissertation by Yi-Chu Hsu [125]. Instead of brief

introduction, more details about sol-gel PZT preparation procedure and its mechanism are deeply discussed. For repeatability and simplification purpose, some process modifications are proposed. The method for sol-gel PZT quality analysis is also included at last.

2.3.1 Sol-Gel PZT Preparation

Sol-gel PZT preparation starts with three organic precursors: lead (II) acetate trihydrate ($Pb(C_2H_3O_2)_2{\cdot}3H_2O$, 99+%, A.C.S. Reagent, Sigma-Aldrich®), zirconium (IV) propoxide ($Zr(OCH_2CH_2CH_3)_4$, 70 wt.% in 1-propanol, Sigma-Aldrich®), and titanium (IV) isopropoxide ($Ti[OCH(CH_3)_2]_4$, 97%, Sigma-Aldrich®).

Lead acetate held in beaker is dissolved in glacial acetic acid (CH_3COOH, with more than 80% acid by mass, J. T. Baker®) at 80 °C on stirring hot plate (Corning® PC-620D). Stirring bar is applied at the moment for a fully precursor dissolution, during which 3 mole crystalliferous water is freed out. The solution temperature is then raised up to 110 °C for 5 minutes to drive water away. This step is crucial since undesired water in the solution will cause gelation of zirconium propoxide and titanium isopropoxide. According to the records, almost 60% failures of sol-gel PZT preparation are directly related to the existence of water in lead acetate trihydrate precursor solution. However, over dehydration may remove necessary acetic acid and decrease solution solubility. To avoid the case, a Parafilm® (Pechiney Plastic Packaging Company) with a hole (around 15 mm in radius) in the middle is covered on the beaker to limit acetic acid evaporation. The anhydrous solution is then cooled to room temperature. In another beaker, zirconium propoxide and titanium isopropoxide are sequentially added and string mixed. 20 minutes later, two solutions are mixed by pouring sticky liquid from one beaker into the other.

At this stage, four reactions such as substitution, esterification, hydrolysis, and condensation occur successively [126]. The mechanism of these reactions requires a fully understanding.

<u>Substitution Reaction</u>

When mixed with acetic acid, both zirconium propoxide and titanium isopropoxide rapidly initiate reactions to exchange their propyl and isopropyl groups with acetyl group according to

$$Zr(OCH_2CH_2CH_3)_4 + 2CH_3COOH \rightarrow Zr(OCH_2CH_2CH_3)_2(CH_3COO)_2 + 2CH_2CH_2CH_3OH \quad (2.6)$$

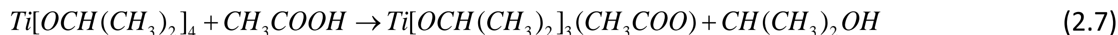

$$Ti[OCH(CH_3)_2]_4 + CH_3COOH \rightarrow Ti[OCH(CH_3)_2]_3(CH_3COO) + CH(CH_3)_2OH \quad (2.7)$$

and produce zirconium propoxide diacetate and titanium isopropoxide monoacetate. These compounds are major materials for the later condensation reaction.

Esterification Reaction

Once substitution reaction is done, the esterification reaction starts [127] following

$$CH_2CH_2CH_3OH + CH_3COOH \rightleftharpoons CH_3COOCH_2CH_2CH_3 + H_2O \quad (2.8)$$

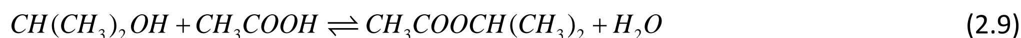

$$CH(CH_3)_2OH + CH_3COOH \rightleftharpoons CH_3COOCH(CH_3)_2 + H_2O \quad (2.9)$$

Propanol and isopropanol yielded from Equation (2.6) and (2.7) will react with remaining acetic acid in the solution to form propyl acetate and isopropyl acetate individually. Water is another product from the reaction and will serve as fuel in the following hydrolysis reaction.

Hydrolysis Reaction

When the quantity of water produced by esterification reaction reaches critical value, it will activate hydrolysis reaction [128] according to

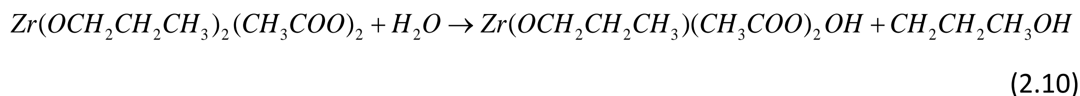

$$Zr(OCH_2CH_2CH_3)_2(CH_3COO)_2 + H_2O \rightarrow Zr(OCH_2CH_2CH_3)(CH_3COO)_2OH + CH_2CH_2CH_3OH \quad (2.10)$$

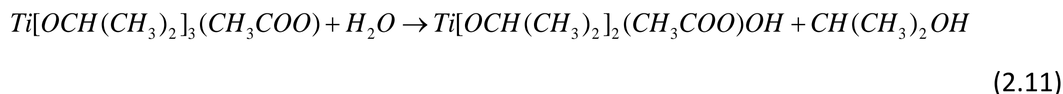

$$Ti[OCH(CH_3)_2]_3(CH_3COO) + H_2O \rightarrow Ti[OCH(CH_3)_2]_2(CH_3COO)OH + CH(CH_3)_2OH \quad (2.11)$$

In the Equation (2.10) and (2.11), both zirconium propoxide diacetate and titanium isopropoxide monoacetate have fast reaction with water and form propanol and isopropanol, respectively. In the meantime, propoxy group ($OCH_2CH_2CH_3$) in the zirconium propoxide diacetate and isopropoxy group ($OCH(CH_3)_2$) in the titanium isopropoxide monoacetate are substituted by hydroxy group (OH). Such hydroxy group can be used in the further condensation reaction to create linkages of metal propoxide acetate [126].

<u>Condensation Reaction</u>

Condensation reaction is brought by the presence of hydroxy group, which will form -Zr-O-Zr- and -Ti-O-Ti- networks within zirconium propoxide diacetate and titanium isopropoxide monoacetate. Possible equations for the reaction are proposed as follow

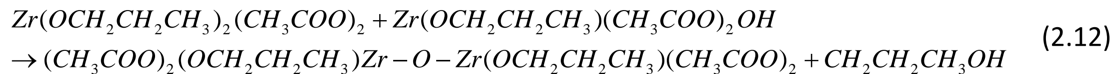

$$Zr(OCH_2CH_2CH_3)_2(CH_3COO)_2 + Zr(OCH_2CH_2CH_3)(CH_3COO)_2OH \rightarrow (CH_3COO)_2(OCH_2CH_2CH_3)Zr-O-Zr(OCH_2CH_2CH_3)(CH_3COO)_2 + CH_2CH_2CH_3OH \quad (2.12)$$

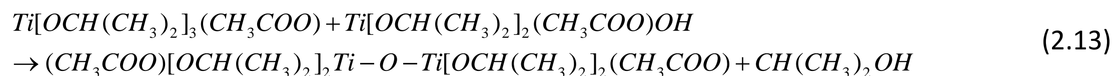

$$Ti[OCH(CH_3)_2]_3(CH_3COO) + Ti[OCH(CH_3)_2]_2(CH_3COO)OH \rightarrow (CH_3COO)[OCH(CH_3)_2]_2Ti-O-Ti[OCH(CH_3)_2]_2(CH_3COO) + CH(CH_3)_2OH \quad (2.13)$$

It is noticed that Equation (2.8) and (2.9) work in both directions. When the water produced in the equation is excessively consumed in the hydrolysis reaction, the equilibrium position of esterification reaction will shift to the right until acetic acid in the solution is used up. Since there is adequate acetic acid in the solution, it can speed up the hydrolysis and condensation reaction. Leaving the solution unattended at this stage, above two reactions will crosslink more -Zr-O-Zr- and -Ti-O-Ti- and eventually lead to the formation of solid precipitates or a fully gelled continuous network and destroy the sol-gel PZT. This post polymerization is what called gelation. Gelation of sol-gel PZT can never be terminated, but there are some ways to slow it. One treatment is to add additional amount of DI water. It is claimed that the gelation time of sol-gel PZT highly depends the amount of added water [129]. When the molar ratio of zirconium propoxide, titanium isopropoxide, and acetic acid is determined, the sol-gel PZT gelation time will dramatically increase as the amount of water increases. Although it is true that at early stage water can also react with zirconium propoxide and titanium isopropoxide to cause gelation, this behavior can be tuned by introducing acetic acid in advance [130]. That's why the proper adding sequence of acetic acid and water must be strictly followed. Another modification for elongating the gelation time is to pre-include extra amount of acetic acid. It is experimentally proved that sol-gel PZT can hardly gel in a reduced pH solution. In general, as-prepared sol-gel PZT can be stored for couple days without gelation if redundant DI water and acetic acid are both present. The solution diluted by such mixed acidic water can also achieve a lower viscosity.

Given enough time, the sol-gel PZT will still turn from transparent to opaque which means certain amount of precipitates or gel come out. This is believed as a result of non-stop esterification reaction causing a reduction of solution acidity, because redundant acetic acid can slowly but persistently reacts with propanol and isopropanol produced through hydrolysis reaction and gradually form ester and water. In order to maintain a low pH value, lactic acid ($CH_3CHOHCOOH$, 85% w/w, Sigma®), a much stronger acid, should be dripped in to stabilize the solution. Glycerin ($CH_2OHCHOHCH_2OH$, 99.9%, Fisher Scientific®) and ethylene glycol ($HOCH_2CH_2OH$, J. T. Baker®) are also sequentially added at last to enhance the sol-gel PZT mechanical properties. It is observed from the experiment that thin film derived by sol-gel PZT with these two additives likely provides much better film elasticity and has lower tendency to crack.

Finally, before applied on thin film deposition, the prepared sol-gel PZT should be vial-sealed and empirically aged for three days to reach its equilibrium state with a light yellow color. A pH test result for such solution should fall in the range of 4.0 ± 0.5 all due to the existences of remaining acetic acid and lactic acid.

2.3.2 Sol-Gel PZT Modification

Ideally, the recipe for sol-gel preparation should work smoothly. However, from repeated experiments we do find some quality variations. Many factors could be responsible for the results. Although quantities of each involved chemical is pre-calculated, measurement error and chemical transfer loss often bring the variance. Also, many other preparation sub-steps such as initial solution water removal, sol-gel filtering, and particle aggregation are all headache problems and can hardly be precisely controlled. For these reasons, sol-gel PZT modification is carried out for targeting the recipe repeatability and simplification.

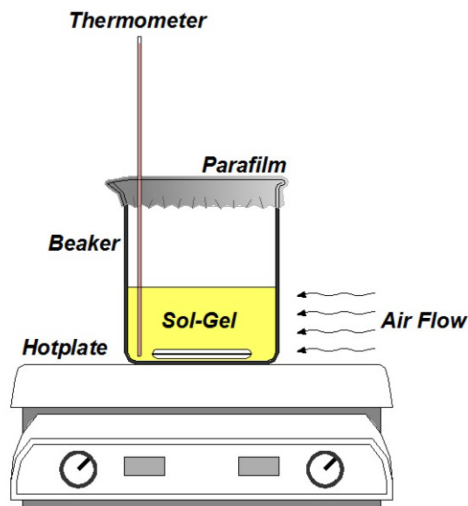

Figure 2.22: Original setup for sol-gel PZT preparation.

As mentioned previously, in the first step when lead acetate dissolves in glacial acetic acid, solution is thermally treated to remove the water. Considering the boiling points for water and acetic acid are 100 °C and 117 °C respectively, 110 °C sitting in the middle is empirically set for water removal. Unfortunately, this stable dehydration temperature is very difficult to reach. During the preparation illustrated in Figure 2.22, beaker on the hot plate only receives bottom up heating which induces solution temperature ununiformity. Hot plate rapid heating can also cause overshoot and transient temperature difference inside beaker. Moreover, surrounding air flow in the fume hood will lead to a fast heat dissipation in solution. Under these circumstances, lots of efforts are made to minimize the temperature influence. For example: First, the beaker is either wrapped circumferentially by aluminum foil (Figure 2.23 (a)) or placed in silicon oil bath to receive uniform thermal condition (Figure 2.23 (b)). Second, Parafilm® is fully covered on top of the beaker to prevent water vapor absorption from open air and help keeping internal temperature. Third, a temperature controller (Corning® CLS400188 or CLS6795PR) is deployed for instant temperature adjustment, see Figure 2.23. These improvements are proved to be effective, but their outputs may highly depend on operators' different manipulating skills. It is quite understood that if such dehydration can be set free of thermal treatment, the process will become much easier and independent of human error.

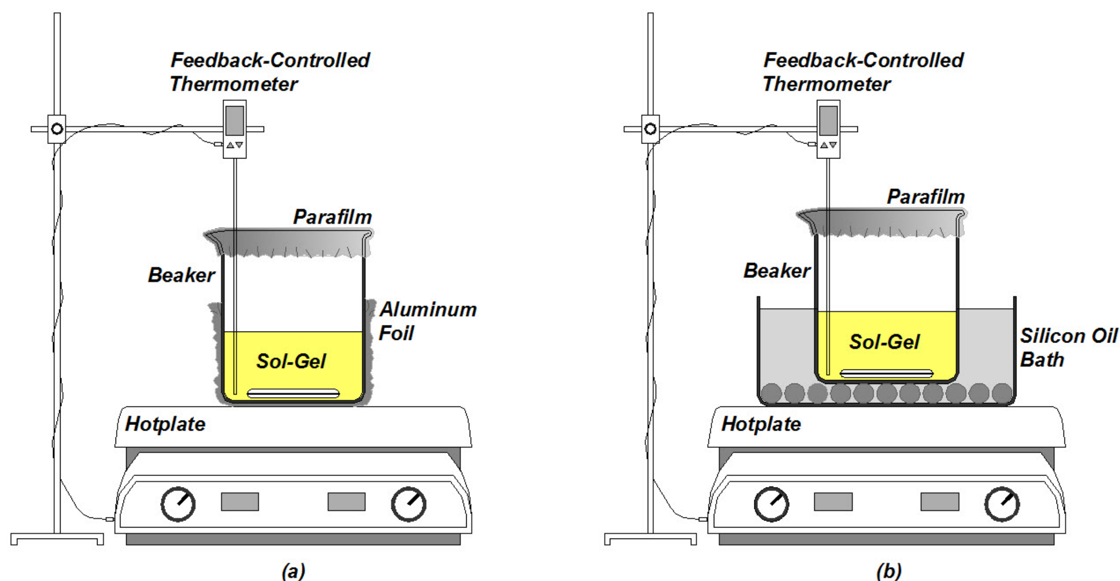

Figure 2.23: Modified setup for sol-gel PZT preparation.

First attempt is physical modification. Molecular sieve (Type 3A, 8-12 Mesh beads, EMD™ Chemicals, Inc.) is one type of silicon oxide material containing tiny pores of a precise and uniform size. It can be operated on molecular level to trap the substance without changing solution composition. Water, for instance, has a much smaller molecule size than those of lead acetate and acetic acid. When molecular sieve is presented, water molecules released from trihydrate could be the only substance forced passing through the pores and retained within them. Before use, molecular sieve need to be baking activated in the oven and furnace cooled to around 35 °C. It is believed that molecular sieve is well functional under acetic acid and can quickly absorb up to 99.9% of water from the solution. The improvement is simple but its drawbacks are obvious. This is because dusts brought by oven activation are usually brought into the acetum solution during molecular sieve soaking. They may cause unwanted chemical reaction and form unexpected precipitates when mixture of zirconium propoxide and titanium isopropoxide is later added. Moreover, contamination could happen due to the additional requirement of filtering process for the sieve separation and the sol-gel collection.

Second attempt is chemical modification. Acetic anhydride ($(CH_3CO)_2O$, J. T. Baker®) is a clear and colorless liquid chemical with a sharp odor similar to that of acetic acid. As the name indicates, acetic anhydride is a compound that is commercially prepared by dehydrating acetic acid at 800 °C according to

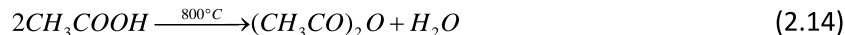

$$2CH_3COOH \xrightarrow{800°C} (CH_3CO)_2O + H_2O \tag{2.14}$$

This reaction has tendency to reverse the direction since acetic anhydride can simply hydrolyzes in water to yield acetic acid under room temperature. Because it reacts with water, through

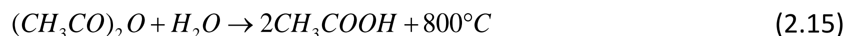

$$(CH_3CO)_2O + H_2O \rightarrow 2CH_3COOH + 800°C \tag{2.15}$$

we could use acetic anhydride as a dehydration agent in reaction mixtures where removal of water is necessary. This improvement is fairly efficient and quite repeatable, but hydrolysis reaction inevitably creates extra amount of unnecessary acetic acid. From Section 2.3.1, plenty of acetic acid will enhance alcohol esterification and chain-affecting hydrolysis and condensation to destroy sol-gel. For this reason, either acetic acid evaporation or water addition has to be used for makeup. However, the former takes too much time to physically remove excessive acetic acid, and the latter can chemically balance esterification but dramatically lower the final solution viscosity and concentration.

Other modifications are focused on sol-gel finalizing such as solution filtration and particle segregation. Dusts, large aggregated particles, and precipitates are often contained in the prepared sol-gel PZT. Previously filter paper is used for solution filtration; see Figure 2.24 (a). This method forces sol-gel penetrate the pores on the paper only under gravity and usually takes several hours. When a syringe (BD 30 ml, Luer-Lok™) combined with MF-Milipore MCE Membrane (0.22 µm, 150 psi (10 bars), Millex®GS) at tip is adopted, sol-gel will be quickly injected through the membrane by applying external pressure; see Figure 2.24 (b). Thus, the infiltration process can be effectively shortened to within half hour. Finally, 20 minutes ultrasonic is applied to vial-bottled solution for fine particle segregation. Experiment results confirm that sol-gel undergoes this step can retain good condition during relatively long term storage.

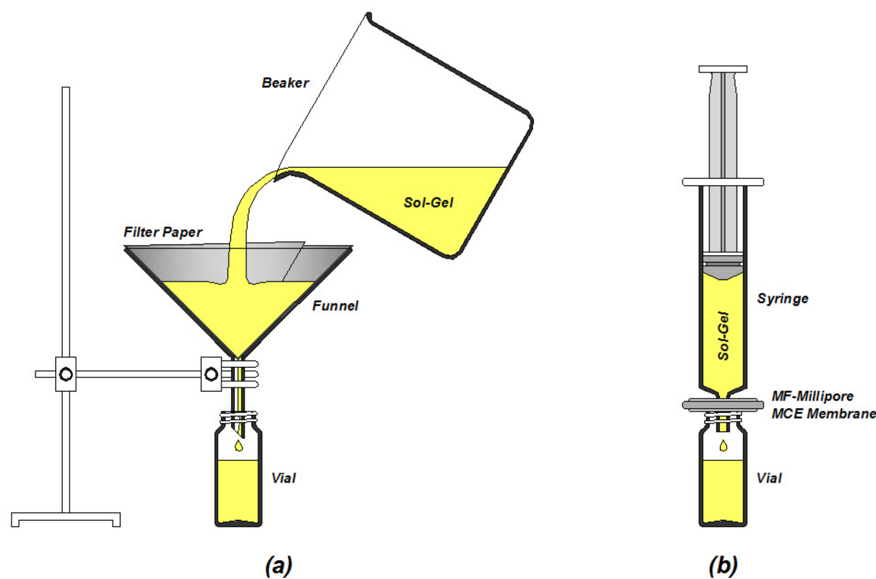

Figure 2.24: Modified setup for sol-gel PZT filtration.

2.3.3 Sol-Gel PZT Analysis

Even strictly following the same procedure, quality variances are often observed in sol-gel PZT prepared through individual batch. Usually, a satisfied sol-gel PZT may arbitrarily be determined by simple clues, for example, appearances such as color, transparency, and viscosity. No wonder, these are not scientific criteria for material qualification judgment. For decades, X-ray diffraction (XRD), a non-destructive analytical technique, is popularly elected for intensive material analysis, because it can easily reveal material information about crystallographic structure, chemical composition, and physical properties. In order to be inspected under XRD, sol-gel PZT must be converted from liquid to solid state by coating (dip-coating or spin-coating) and firing in advance to form consolidated thin film on selected substrate. The film is then exposed under incoming X-ray and measured for beam scattered intensity (counts) in terms of incident and scattered angle (2θ), polarization, and wavelength or energy. Figure 2.25 illustrates the setup of a typical XRD (Bruker AXS D8 FOCUS Diffractometer) while its inspection results for sol-gel PZT prepared from different batches are group listed in Figure 2.26. The sol-gel PZT analysis obeys material standard analyzing procedure and is described as follow.

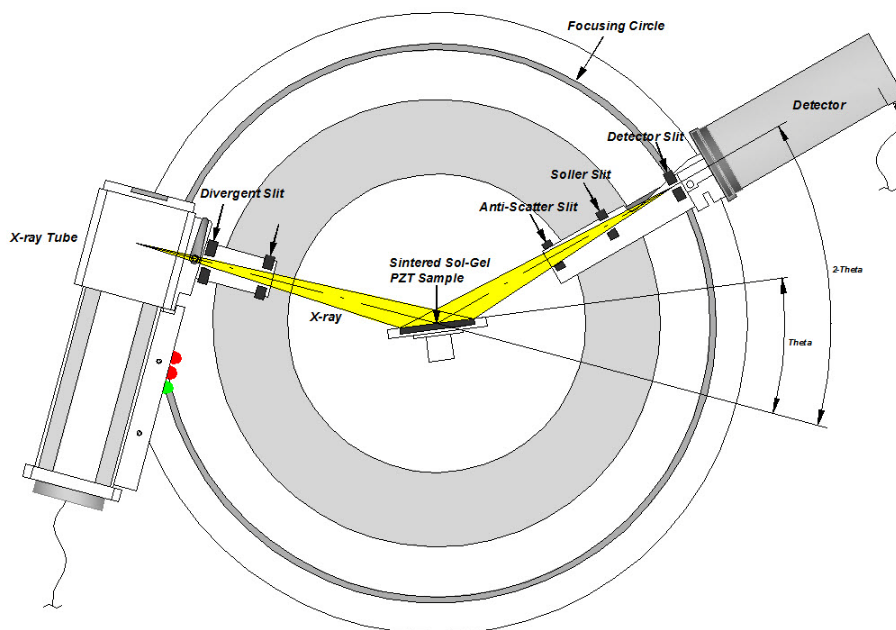

Figure 2.25: Setup of a typical XRD

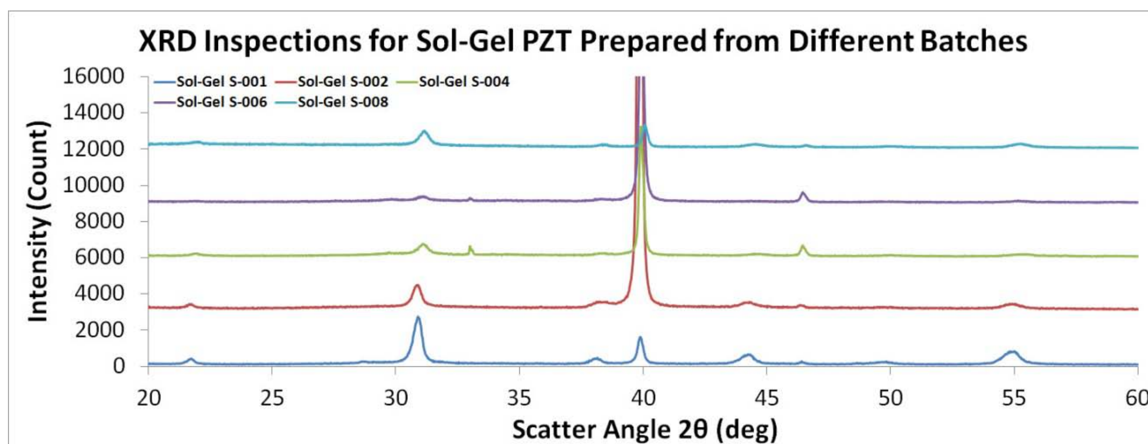

Figure 2.26: XRD inspection results sol-gel PZT prepared from different batches

Crystallographic Structures Verification

Controlled by solution stoichiometric ratio, the obtained PZT film sintered from sol-gel is expected to be crystallized $Pb(Zr_{0.52}Ti_{0.48})O_3$. Through XRD inspection, the scattered data is decoded by Jade Software™ and compared with reference database [131] for peak location and intensity verification; see Figure 2.27 and 2.28. Such step is preliminarily used for quick verification of the presence of expected PZT crystal structures.

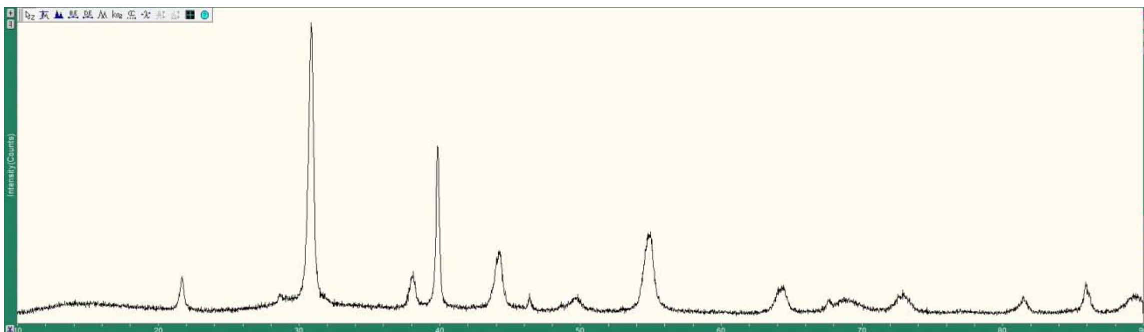

Figure 2.27: X-ray beam scattered intensity vs. incident and scattered angle (2ϑ) plot for sintered sol-gel PZT

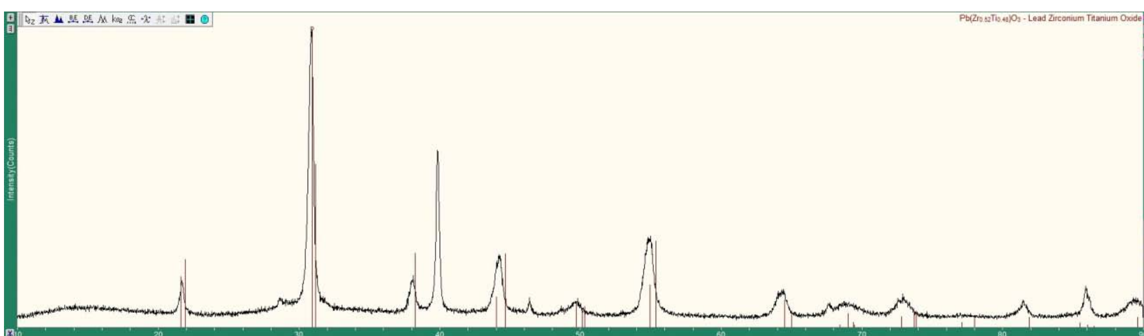

Figure 2.28: XRD inspection data curve superimposed with $Pb(Zr_{0.52}Ti_{0.48})O_3$ reference database

Chances are that XRD inspection data curve is sometimes not perfectly aligned with reference database. This is quite common for many possible reasons. One could be different phases exist in the PZT film. It is not necessary that sintered sol-gel PZT yields crystal structure, more often, as pointed out in Figure 2.29, amorphous PZT can be formed as a byproduct and contributes extra peaks. Merged double peaks or multi peaks should be responsible for another reason. Although with different intensity, Jade Software™ tends to treat them as one when these adjacent crystal PZT peaks stay too close to each other; see Figure 2.29. Other reasonable possibilities could be peak shift, either equal shift or random shift. Equal peak shift is usually caused by XRD equipment lacking of periodic system calibration. Random peak shift is due to the difference of crystal structure lattice model between sintered sol-gel PZT (monoclinic, rhombohedral, or tetragonal) and ideal model (cubic) from standard database; see Figure 2.30. All these need careful considerations and should be sorted out from crystallographic structures verification.

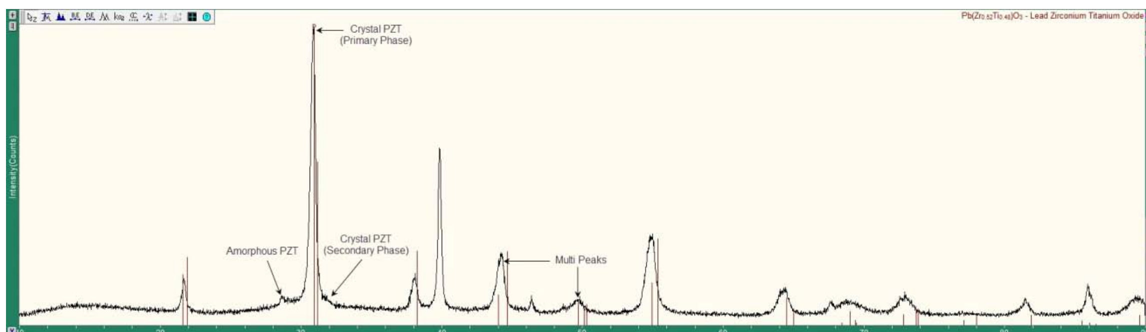

Figure 2.29: XRD inspection data curve with amorphous PZT and crystal PZT multi peaks

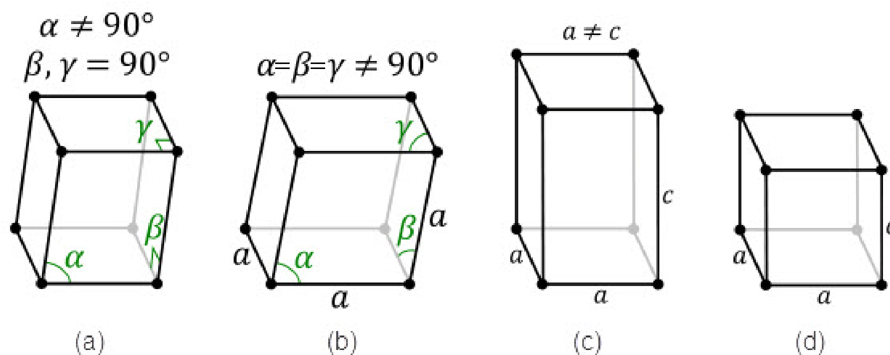

Figure 2.30: Possible crystal structure lattice model for PZT. (a) monoclinic, (b) rhombohedral, (c) tetragonal, and (d) cubic.

Chemical Compositions Identification

Even XRD inspection data curve for sintered sol-gel PZT is well aligned with reference database, it is still hard to determine whether the right compounds are obtained or not. Peak normalized percentage area is a quite useful tool for further identification of chemical compositions. After peak search and decomposition process illustrated in Figure 2.31, Jade Software™ will provide percentage area of each found peak that normalized respect to the largest peak. In the example case, fourteen peaks of sintered sol-gel PZT are identified through XRD within angles (2θ) from 10° to 90°. Their percentage area values corresponding to specific angles are listed in Table 2.15. In the meantime, such values of those from reference database are also presented. Similarity comparison between these two datasets will finally confirm the previous expectation. In our case, the results show pretty good agreements which indicate the right compounds formation of PZT are achieved.

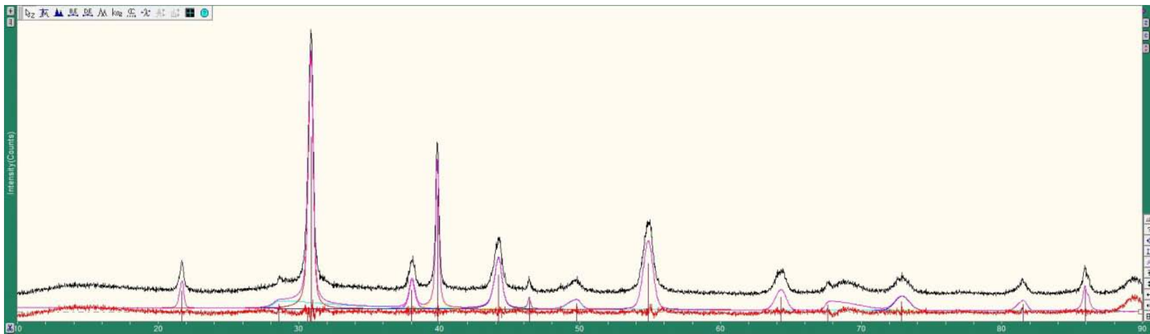

Figure 2.31: XRD inspection data curve after peak search and decomposition process

Table 2.15: XRD inspection data for PZT peak percentage area

Angle 2θ (deg)	Peak Height (Count)	Percentage Height (H%)	Peak Area (No Unit)	Percentage Area (A%)
21.719	299	11.9	120.7	10.4
28.658	120	4.8	97.8	8.4
30.880	2510	100.0	1164.6	100.0
38.137	309	12.3	143.1	12.3
39.861	1451	57.8	467.8	40.2
44.240	507	20.2	325.4	27.9
46.401	137	5.4	27.6	2.4
49.678	99	3.9	72.8	6.3
55.000	668	26.6	512.5	44.0
64.420	231	9.2	183.8	15.8
67.717	74	3.0	22.3	1.9
72.999	141	5.6	120.5	10.3
81.443	142	5.7	83.0	7.1
85.920	269	10.7	134.0	11.5

Physical Properties Determination

This final step is for material quality purposes. Two physical properties are required to be determined which are PZT grain size and lattice constant.

PZT grain size, often refers to as crystal diameter for single crystal material, is conducted for determining PZT quality since larger PZT grain size usually provides better piezoelectric performance [132,133]. Its value can be generally calculated from

$$t = \frac{0.9\lambda}{B \times \cos(\theta)} \tag{2.16}$$

where t, λ, B, and ϑ are the diameter of the PZT crystal, the wavelength of X-ray source, peak full width at half maximum (FWHM), and X-ray incident angle, respectively. Since the operated XRD (Bruker AXS D8 FOCUS Diffractometer) adopts Cu Kα_1 X-ray source whose wavelength is 1.54059 Å, Equation (2.16) can be modified to

$$t = \frac{1.386531}{B \times \cos(\theta)} \tag{2.17}$$

For this case, the largest peak of crystal PZT is found at angle 2θ of 30.880° in Table 2.15 where its FWHM listed in Table 2.16 is 0.394 *rad*. From Equation (2.17) the PZT crystal diameter is calculated to be 23.493 nm.

Table 2.16: XRD inspection data for PZT FWHM and d-spacing

Angle 2θ (deg)	FWHM (rad)	Plane Indices (l m n)	d-Spacing (Å)	Reference d-Spacing (Å)
21.719	0.0060	0 0 1	4.0885	4.1097
28.658	0.0121	N/A	3.1124	N/A
30.880	0.0069	1 0 1	2.8933	2.8865
38.137	0.0069	1 1 1	2.3578	2.3515
39.861	0.0048	N/A	2.2597	N/A
44.240	0.0095	0 0 2	2.0457	2.0549
46.401	0.0030	N/A	1.953	N/A
49.678	0.0109	1 0 2	1.8337	1.8329
55.000	0.0114	1 1 2	1.6682	1.6702
64.420	0.0118	2 0 2	1.4452	1.4432
67.717	0.0045	0 0 3	1.3826	1.3699
72.999	0.0127	1 0 3	1.2950	1.2978
81.443	0.0087	2 2 2	1.1807	1.1758
85.920	0.0074	2 0 3	1.1303	1.1351

Lattice constant is the parameter accepted as constant distance between unit cells in a crystal lattice. Three dimensional lattices acquire three lattice constants, but in the special case such as cubic crystal structures all constants are ideally equal (Figure 2.30(d)) and can be calculated through

$$a = d_{lmn} \times \sqrt{l^2 + m^2 + n^2} \tag{2.18}$$

where a, d_{lmn}, l, m, and n are lattice constant, d-spacing, and plane indices in Cartesian coordinates along x, y, z directions, respectively. For this case, d-spacing for each peak of crystal

PZT is determined by Jade Software™ from Figure 2.32 and they are listed in Table 2.16 together with reference values for comparison. Moreover, internal calculation also provides a set of plane indices for each corresponding peak; see Figure 2.33. Since only the largest peak of crystal PZT is interested, its plane index is found to be <101> which indicates *l*, *m*, and *n* are 1, 0, are 1, respectively. Applying Equation (2.18), the calculated lattice constant for the sintered sol-gel PZT is 4.092 Å (such value from reference database is 4.082 Å). This result fairly agrees with that of typical $Pb(Zr_{0.52}Ti_{0.48})O_3$ which has a value of 4.036 Å [100].

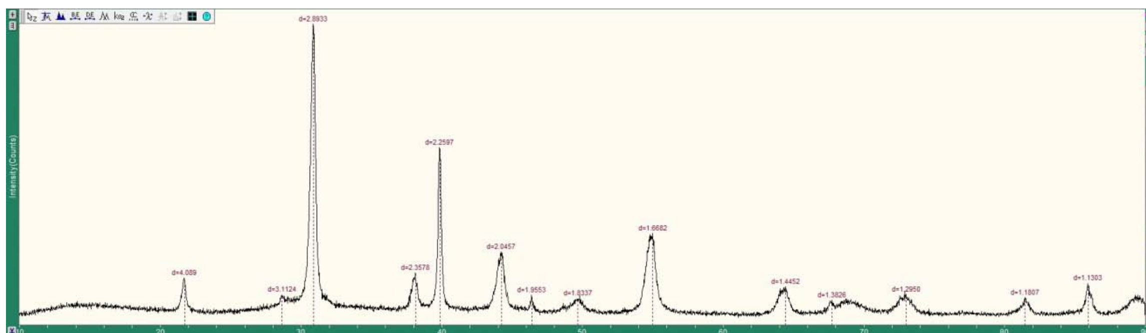

Figure 2.32: d-spacing values for each peak of crystal PZT

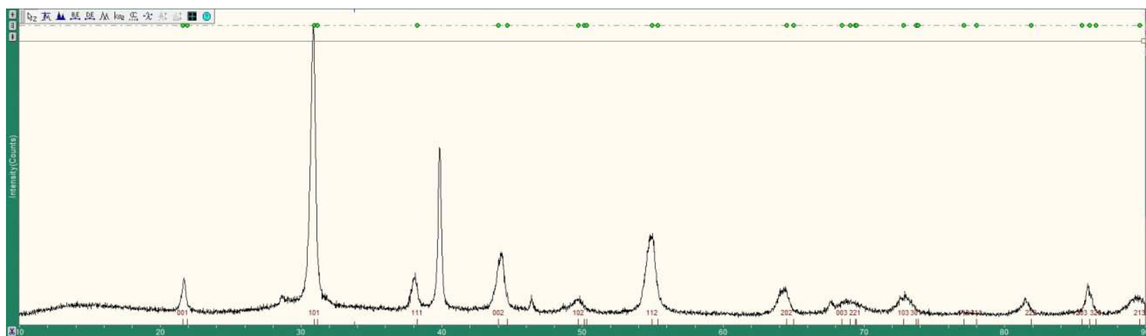

Figure 2.33: Plane indices for each peak of crystal PZT

So far, a satisfied sol-gel PZT with proper chemical composition and potential good quality in sintered thin-film PZT is proved to be accomplished.

2.4 Thin-Film PZT

Thin-film PZT deposition is one of the key processes throughout the whole fabrication, simply because its yield has a strong impact on the performance. Although hard works from previous researchers provide a guideline, the evolution of the process never ends. It is observed that even strictly follow the provided recipe a high product yield may not be one hundred

percent guaranteed. This is because there are still many uncertainties could be involved during the process to cause unrepeatable results. The section will first begin with a brief introduction to several current available techniques for PZT deposition. After that, a more detailed description of sol-gel derived PZT is elaborated step by step. In the meantime, some major possible defects brought by the technique are deserved to be emphasized and extensively discussed. After numbers of pertinent improvements, it is now confident to claim that we are able to achieve a three-coating, uniform, and crack free thin-film PZT on a 3 inches wafer.

2.4.1 Deposition Techniques

According to the different usages, PZT material is usually fabricated in terms of thin film (up to 1 μm), thick film (up to 100 μm), and bulk (up to 1 mm). In the past few decades, a lot of research effort has been devoted to make PZT fabrications compatible with standard MEMS processing as well as improving the PZT properties. Today, there are only four major approaches widely adopted: screen printing deposition (SPD), physical vapor deposition (PVD), chemical vapor deposition (CVD) and chemical solution deposition (CSD).

SPD is a traditional technique of fast depositing films with thickness in the range from 10 μm to 100 μm. In many MEMS applications, devices require PZT films up to tens of microns for high resonance frequency and high voltage sensitivity [134]. Most modern techniques have limitations of depositing PZT with large thickness. For this reason, SPD becomes a preferred simple and convenient method for getting PZT thick films [135,136]. However, the PZT thick films fabricated through this method has significant drawbacks. Printed PZT thick films can hardly avoid high structure porosity. Such porosity will inevitably cause a low $e_{31,f}$ coefficient and eventually leads to a decreased charge sensitivity [134].

Sputtering deposition as one type of PVD is a mature technique used to coat thin films of a material onto selected substrate. When sputtering ions, typically argon ions, are created, they will accelerate into the target and knock out the material. The target material is ejected in the form of neutral particles and travel in a straight line until they reach the coating substrate. Through intensive researches, many advantages of sputtering deposition prove it to be an efficient and stable method for PTZ thin films fabrication, especially on a very large substrate (8 inch silicon wafer) [137]. First, it can ensure the PZT good uniformity, reproducibility and high density [138]. Second, it can enhance the PZT thin films adhesion on the substrate. Third, it will

maintain coated PZT material composition close to that of the target. However, it is also noticed that during the sputtering deposition the inert sputtering gases are easily built into the growing thin films and cause PZT impurities [139]. With such imperfection, the researchers have to pay extra attention to identify the sputtering conditions.

Metalorganic chemical vapor deposition (MOCVD) is a newly derived CVD technique and has been widely used for high brightness light emitting diodes (LEDs) manufacturing recently. The feasibility investigation of MOCVD for PZT thin films fabrications never stops, because many preliminary results show that it can be a possible good substitute. During the PZT fabrication process it can flexibly control the Zr/Ti ratio by adjusting each precursor temperature and carrier gas-flow rates [140]. It is also reported that the PZT thin films prepared through MOCVD show good uniformity with fine grain size [141]. However, additional researches discover that the process window for growing a single phase PZT could be very narrow in the low-temperature MOCVD. Furthermore, it is claimed that the control of the amount of Pb input precursor is crucial for the formation of the crystalline PZT phase [142]. All these results indicate that MOCVD is very promising but still needs great improvement.

Sol-gel processing belongs to the category of CSD technique. The solution is prepared in advance with the required chemicals. After spin-coated onto a substrate, the solvent is evaporated and the solution is gelled to form a condensed film. Provided a rapid thermal annealing (RTA) heat treatment, such film can be subsequently densified by relatively low sintering temperatures (usually less than 700°C) [126,129]. As compared to the above three methods, sol-gel technique is now the most widely employed fabrication method for PZT thin films. Unlike PVD and CVD, the sol-gel technique does not require vacuum chamber and the composition of the PZT thin film is much more easily controlled. Deposition over large and flat surfaces is much easier with the sol-gel technique, and better results are found in terms of film homogeneity [143]. Moreover, sol-gel technique results in a suitable method of integration with many MEMS processes [144,145]. But every coin has both sides. Unfortunately, what makes sol-gel technique possible also makes it headache to the researchers. First, the thicknesses and uniformities of PZT thin films highly depend on viscosity of sol-gel solution, rotation speed of spin-coating, shape and size of depositing substrate, and wettability of bottom electrode layer. Second, sol-gel technique could be very sensitive to the environment such as floating dust, ambient temperature, and surrounding humidity. Third, since the stack layers have different

thermal expansion coefficients, improper heat treatments may introduce PZT thin film internal cracks, layer delaminations, and even film peeling off. Fourth, lab-made sol-gel derived PZT thin film has big variations in material properties such as piezoelectric coefficients, dielectric coefficients, and stiffness coefficients. Thus, a careful study turns out to be necessary for acquiring satisfied PZT thin films.

2.4.2 Sol-Gel Deposition

Due to the profound accumulative experience in the past, sol-gel derived PZT is naturally selected as thin film deposition technique. The procedure mainly follows the step seven and eight listed in Section 2.1 with Figure 2.1(d) and can be further described in details as follow. First, chemical pre-cleaned wafer is coved by Scotch® brand tape (3M Company) on surrounding edges as shown in Figure 2.34(a) to protect the alignment mark and extraction bottom electrode. Second, platinized wafer is spin-coated with aged sol-gel PZT on a spinner (Headway PWM32) to form a smooth gel-like amorphous PZT layer. Third, PZT coated wafer is left in an open air condition for additional solvent evaporation to encourage cross-linking being formed among individual PZT nano-clusters. Forth, wafer substrate is removed of Scotch® brand tape (3M Company) and sintered in general purpose tube furnace (MRL812 atmospheric furnace stack tube 4) at 650 °C for 15 minutes to obtain densified thin-film PZT with desired crystalline phase; see Figure 2.34(b). It needs to be pointed out that RTA with a sudden high temperature rise is intentionally chosen in this heat treatment step, majorly for a better PZT crystallization and a reduction of thin film surface damage [146,147]. Fifth, repeat previous four steps twice by stacking another two layers of PZT to reach the desired thin film thickness (generally around 0.4 µm per layer and 1.2 µm in total for thin-film stack). P-15 stylus surface profilometer (KLA-Tencor Corporation) is involved for each layer thickness measurement.

In the early development, diluted sol-gel PZT is kept applying as coating material for the third layer stacking. Since no systematic work has been carried out at that moment, first two obtained PZT coatings often hard to avoid cracks. In order to prevent film short, it is believed that a use of diluted sol-gel PZT can seal the possible defects. However, regardless of its effect, the sealant layer does pay the price for sacrificing the total film performance. Fortunately, such dilemma has been solved through recent study. Now a diluted sol-gel for three-layer PZT deposition is not adopted any more.

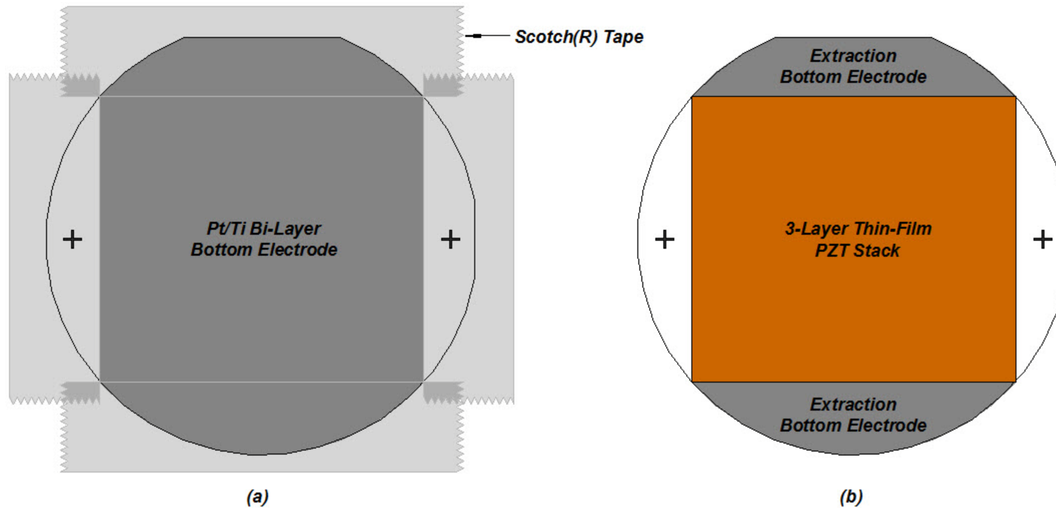

Figure 2.34: Typical procedure for stacking thin-film PZT by means of sol-gel technology

2.4.3 Defect Inspections

Before any fabrication improvements, sol-gel derived PZT thin films often show some imperfections. Bumps, dimples, black dots, cracks, and even peels off are four basic types of defects frequently discovered under optical microscope inspections. Figure 2.35 illustrates the inspection detailed locations.

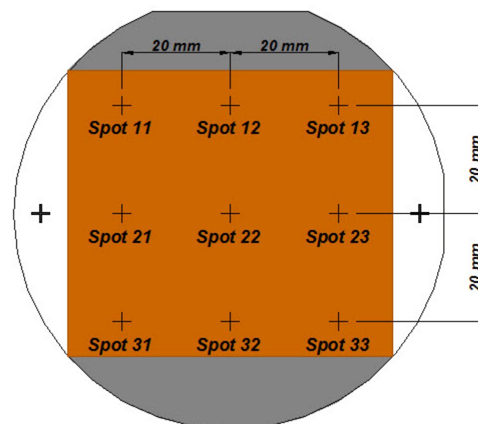

Figure 2.35: Nine-spot inspection array for thin-film PZT defect inspection

<u>Bumps/Dimples</u>

Bumps and dimples refer to as out-of-surface and into-the-surface geometries that widely dispersed all over the thin-film PZT. Several reasons are responsible for its formation. The primary one could be sol-gel PZT itself. During sol-gel PZT preparation, dehydration process

intends to over drive the essential acidic solvent and end up with a relatively sticky solution. The observing color also turns from light yellow to yellow. Originally, the idea of using spin-coating is to help fast spread sol-gel PZT and precisely control thin film thickness. But the uniformity of the film obtained this way is very sensitive to solution viscosity. When over dried sol-gel PZT go through spin-coating process, its lower fluidity introduces a drag force and enhances the film non-uniformity with radial strips. Such strips will be propagated by layer-stacking technique in form of bumps and dimples; see Figure 2.36.

Figure 2.36: Thin-film PZT bumps and dimples inspections on wafer SI-056 at spot 13. Pictures from left to right represent surface non-uniformities on 1st, 2nd, and 3rd layers, respectively.

On the contrary of solvent over removal, dilution is another extreme case. Diluted sol-gel PZT is normally chosen for the 3rd layer spin-coating in old recipe, because it is believed to provide a thinner dummy film and seal the cracks formed on first two layers. As sol-gel PZT is freshly prepared, a certain amount of the solution is spared for dilution with glacial acetic acid at volume ratio of 1:1. It is then stirred in ultrasonic bath for segregation and aged before apply. After aging process, sol-gel PZT with extra acetic acid unlikely forms an entire continuous polymeric network throughout the solution. When spin-coated on a substrate, the layer made of aged diluted sol-gel PZT will form a gel film in terms of discrete polymeric clusters. Such discontinuity finally becomes bumps and dimples after film sintering process; see Figure 2.37.

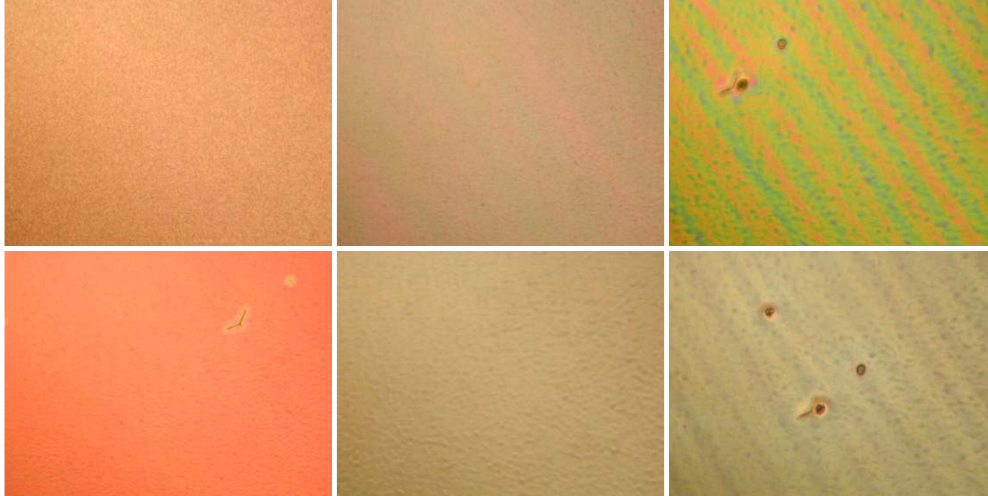

Figure 2.37: Thin-film PZT bumps and dimples inspections on wafer SI-072 at spot 11. Columns from left to right represent surface non-uniformities on 1st, 2nd, and 3rd layers, respectively. Upper and bottom rows are inspections before and after film sintering.

Above inspections uncover another truth. The gel film derived from diluted sol-gel PZT has low film quality which may not be able to fully secure underneath cracks and provide added performance.

Wettability of platinized silicon substrate has been found to be the third reason causing thin-film PZT bumps. In general, this property is usually determined as a balance between adhesive and cohesive forces. Adhesive force tends to create bonding between sol-gel PZT and substrate surface while cohesive force within sol-gel PZT tries to maintain surface tension and avoid such connection. Platinized substrate will turn hydrophobic when sol-gel internal cohesive force becomes greater than the interactive adhesive force. Instead of uniformly spread across the large flat surface, spin-coated sol-gel PZT on the hydrophobic substrate will seek opportunity to shrink and bulge up. After film sintering, these bulges become bumps.

From point to point, non-uniformity introduced by bumps and dimples potentially affects thin-film PZT electrical and mechanical properties such as film capacitance and bending fatigue. But since they have relatively low impact on the PZT quality and will not fundamentally destroy the thin film, bumps and dimples are usually considered as minor defects.

Black Dots

Black dots are general terms for large particles, dusts, and holes observed under optical microscope; see Figure 2.38. The presence of black dots on thin-film PZT should be considered as localized crack initiation and may potentially cause total failure (short circuit) on film at specific location where devices are later built on. Luckily, fabrication experience demonstrates that under most cases black dots are found to be rare and scattered. Since chances are little that devices array bares severe yield drop purely due to their existence, black dots, to a certain extent, could also be regarded as minor defects. Generally, there are two possible reasons causing black dots, which are sol-gel PZT aging period and thin-film PZT spin-coating environment.

Figure 2.38: Thin-film PZT black dots inspections on 1st layer of wafer SI-207. Columns from left to right represent inspection spot 11, 21, and 32 respectively. Upper and bottom rows are inspections before and after film sintering.

As noted previously, internal chemical reaction of as-prepared sol-gel PZT could extremely slow down but will never fully stop. Before achieving a more stable solution, such fresh sol-gel PZT still contains large amount of free acids at its early aging stage. In this highly acidic environment, acetate anions released from hydrolyzed lead acetate will tend to increase its concentration and form dendritic crystals of lead acetate hydrate all due to the ion effect [129]. If not properly treated, these crystal particles will be transported from sol-gel PZT onto substrate and permanently implanted as “seeds” in thin-film PZT through high speed spin-coating process.

Thin-film PZT spin-coating environment is referred to as dust grade. Strictly speaking, 10,000 class cleanroom in WTC is not a dust free environment. Pre-cleaned wafer and just spin-coated sol-gel PZT layer are likely to capture floating dusts from surrounding open air due to their strong needs of fast surface tension removal. In the later sintering process, these inherited dusts will be either firmly embedded into the PZT thin film or burnt away but leave pinholes behind.

Cracks

Based on their observing size and destructive area, cracks are often classified as micro or large cracks; see Figure 2.39. Other than bumps and black dots, cracks could be determined as criterion for films failure. They first initiate randomly at several local points and then fast grow under following series of heat treatment to pull films apart introducing a direct electric short. Cracks are usually related to sol-gel PZT aging period, spin-coated gel film thickness, and thin-film PZT internal residual stresses.

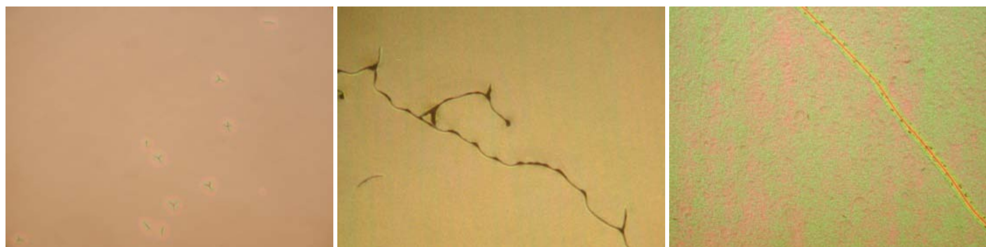

Figure 2.39: Thin-film PZT cracks inspections. Left picture shows micro cracks on 3rd layer of wafer SI-207. Right two pictures are large cracks on 2nd layer of wafer SI-215 and 1st layer of wafer SI-193, respectively.

According to the classic recipe, just-prepared sol-gel PZT requires at least 72-hour aging period forming polymeric network through hydrolysis and condensation reactions. These two reactions can also effectively reduce the concentration of acetate anions in the solution. When an under polymerized fresh sol-gel PZT is spin-coated, those acetate anions may suppress the polymeric network formation. Instead of creating elastic gel films, brittle layers with mixture of metal salts such as lead acetates are produced. The existence of acetate anions in the coatings will continuously degrade the films ductility and introduce cracks during film drying and sintering process [129].

Standard operating procedure (SOP) of thin-film PZT fabrication suggests a thinner coating for each stacking layer when sol-gel technique is applied, since lower layer thickness can improve film drying behavior and profoundly avoid film cracks. Currently, 20 nm to 0.1 μm per coating is widely adopted throughout the industry. However, to achieve satisfied performance, thin-film PZT must take certain thickness. This requires a substantial number of layer-stacking. Without assistance of special equipment, the process could be extremely time consuming and unaffordable on a research basis. Thus, the conflict of interests between single coating and film overall thickness must be settled. Through continuous research, an empirical three-coating-to-one-micron process is developed by Yi-Chu Hsu [125]. It simplifies the layer-stacking process and can time-effectively fabricate a thin-film PZT to around 1.2 μm by pushing the limit of maximum allowable single coating thickness up to 0.4 μm. The process is very appealing, but it also masks some unforeseeable risks. One of them could be film cracks. As is spin-coated at room temperature, solvent vaporization only occurs on the surface of a thicker layer. Meanwhile the dried layer surface is cured as a sticky shell that prevents water, acid, and ester stored inside the gel film from evaporating. Undergoing a sequential firing, the sticky shell and the gel film underneath will expend at different rate inducing an unbalanced shear thermal stress. The torn thicker layer may not survive from cracking if sol-gel PZT applied to it is not well polymerized.

Another major issue causing cracks is the mismatches in coefficients of thermal expansion (CTE) α among successive thin-film PZT, Pt/Ti bottom electrode, and silicon substrate. It is reported that thermal expansion coefficients for these three layers are 7×10^{-6}/K [148,149], 9.94×10^{-6}/K, and 3.5×10^{-6}/K [150], respectively. When rapid thermal annealing at 650°C is first applied, polymeric gel network in a spin-coated PZT will be quickly condensed and crystallized. Right after becoming a solid ceramic layer, thin-film PZT together with electrode and substrate are all trying to expend under different thermal expansion coefficients. Therefore, significant thermal stress would be generated at this moment. Brittle thin-film PZT could be ripped across the surface with open cracks if it is not strong enough to hold the stress.

Peels off

Peels off are aftermaths of a production of disqualified Pt/Ti bottom electrode. They usually launch at three different layer locations that are the PZT/electrode interface, inside electrode, and the electrode/substrate contact surface. Boosted by series of heat treatment and cracks

growth, partial or entire thin-film PZT will eventually be popped out, curled up, or lifted off; see Figure 2.40. Figure 2.41 also presents the macro and micro views of PZT peels off.

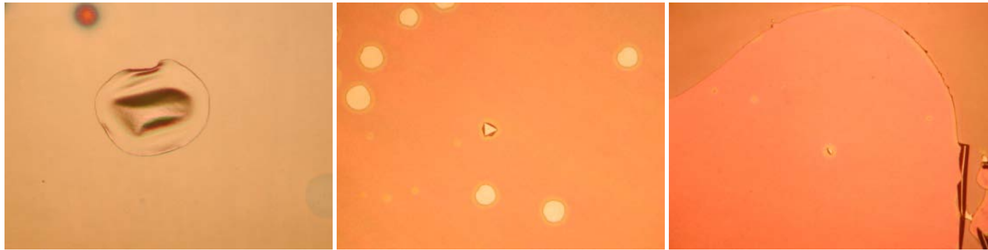

Figure 2.40: Thin-film PZT peels off inspections. Left picture shows popped out PZT on 1st layer of wafer SI-162. Right two pictures are small and large peels off on 2nd layer of wafer SI-209 and SI-221, respectively.

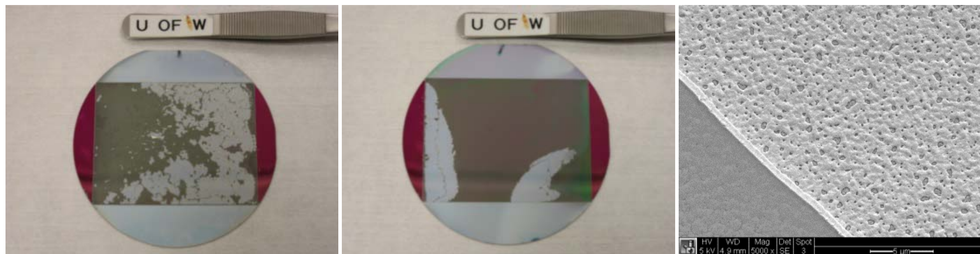

Figure 2.41: Left two pictures are macro views of peels off on wafer SI-206 and SI-207, respectively. Right picture shows micro view of peels off on wafer SI-216 under SEM, where the lower left region is the remaining PZT and the upper right region is the bottom electrode after PZT removal.

Sol-gel PZT spin-coated on Pt/Ti bottom electrode is expected to achieve a complete wetting. But as claimed by many researchers that such behavior highly depends on surface properties such as surface energy, chemical composition, roughness, surface heterogeneity, and contaminants [151,152]. Unlike other type of solids such as carbons that are held together essentially by van der waals force and hydrogen bonds, Pt/Ti crystals are linked by chemical bonds that possess intrinsic high energy surface. Experiment results agree that bottom electrode likely to be more wettable with higher surface energy. Meanwhile, E-Beam evaporated Pt/Ti must be annealed as a condensed bi-layer before sol-gel is applied. Although porous electrode is unavoidably created, its random surface texture could enhance the surface hydrophilicity. However, since the electrode is composed of two different types of metals, its wettability will turn heterogeneous. Moreover, rough Pt/Ti surface easily seize inorganic

particles around it to secure its hydrophobicity by lowering surface energy. Sol-gel liquid spread on a more hydrophobic bottom electrode may not strictly follow the roughness profiles on entire surface providing a full contact. For this reason, sometimes PZT bumps are formed, while in more serious cases, peels off occur.

Many special applications require a direct sol-gel PZT spin-coating on a just-evaporated flat Pt/Ti bi-layer. It is reported that smoother metallic surface are found to decrease the surface energy seeking a low wettability [153,154]. Also, unconsolidated metal electrode is more like a layer of snowflakes with loose grain interconnections. RTA-sintered with PZT coating, this weak bottom electrode can hardly endure the thermal stress generated by CTE mismatch. Finally, internal delamination will destroy the electrode and tear the whole piece of thin-film PZT off the substrate.

The use of Pt/Ti annealing will help achieving a much stronger bottom electrode, but the process barely avoid Ti diffusion into Pt. Due to the limit of metallization, evaporated Pt/Ti can only be deposited on a substrate with low temperature (approximately 200 ˚C). Such deposition condition is expected to produce an electrode containing Pt in small grain size. These small grains tend to re-crystallize under following annealing process by coalescing at the grain boundaries. However, the heat treatment also provides great opportunities for underneath Ti oxidation and migration through the Pt grain boundaries. This possibly results in a depletion of Ti bonding material and subsequent loss of bottom electrode adhesion [112]. When PZT fabrication is attempted on such electrode, thin-film will be either partially popped up or entirely stripped off.

2.4.4 Parametric Study

Through systematic investigation, the above imperfections are found not to be the result of a single parameter but the aftermaths of joint effect of many factors. In the real case, it will be a hard time to deal with all factors simultaneously. That's why a parametric study is necessarily carried out to help sorting out their impacts priorities. We believe a right order of corresponding treatment will simplify the fabrication of thin-film PZT and efficiently increase its yield. Moreover, since experience implied that those imperfections usually start at PZT initial coating, the following work will majorly focuses on the first PZT layer preparation. To set up a study

baseline, all sol-gel PZT are spin-coated at standard cleanroom temperature (72 ˚F / 22 ˚C) and RTA sintered at 650 ˚C for 15 minutes.

Drying Methods

The study begins with the humidity effect since it is suspected by some researchers that environmental humidity is a dominant parameter to the thin-film PZT productivity. It is because humidity induces the high water saturation in the ambient air and constrains the solvent evaporation from spin-coated PZT gel film. According to the records, in year 2007 humidity in WTC varies from 21% to 68%. An under dried polymeric film through firing process will result a hollow structured PZT. This is originally believed to be completely true especially when bumped or cracked PZT with black dots is repeatedly produced in the wet winter nights. The suspect of humidity effect inspires the following study.

One Pt/Ti bi-layer evaporated wafer (SI-193) with high porosity is randomly chosen as substrate and diced undergoing preliminary test. A fully aged (about one and half month) non-diluted sol-gel PZT is applied for first coating. According to the Table 2.17, wafer specimens are dried individually under different conditions but RTA sintered together with the same manner. Note that all parameters below are empirically set.

Table 2.17: Empirical parameters for humidity effect study

Wafer No.	Piece No.	Pt/Ti Porosity	Sol-Gel Type	Aging (Day)	Humidity (%)	Dry Method	Dry Time (Min)	Dry Temp. (°C)	RTA Temp. (°C)	RTA Time (Min)
SI-193	1	High	Non-diluted	49	37	Open Air	15	22	650	15
	2	High	Non-diluted	49	37	Vacuum	15	22	650	15
	3	High	Non-diluted	49	33	Dry Box	15	22	650	15
	4	High	Non-diluted	49	33	Hot Plate	2	200	650	15

For a well care of each specimen, four diced pieces are divided into two groups and processed separately. We do notice that relative humidity slightly changes (37% vs. 33%) when operation switches from first group to the second. But such variation could be negligible since it is small enough to be well within the tolerance and will not significantly affect the results. According to the experiment design, PZT treated by hot plate is supposed to outperform other samples and that open-air-dried one should become the worst. The basic thoughts quite follow the intuition. Specimen left in the open area endures a passive dry. The extent of solvent

reduction solely depends on its ability of natural vaporization under room temperature. Plus the ambient humidity effect, most of solvent will undoubtedly be stored in the film polymeric networks. Dry box and vacuum chamber can provide lower vapor pressure and relatively speed up the solvent drying, but 15 minutes may not be long enough for entire solvent removal. Although fully exposed under open air, the specimen on the hot plate should not receive much influence from surrounding humid air. This is because baking heat from hot plate below will actively drive the solvent up to its vapor point and compel it to move away from the gel film. However, when comparing the surfaces on all collected specimens, it is surprisingly found that all PZT thin films are about same bad qualities; see Figure 2.42. Black dots and holes are evenly distributed throughout the films surfaces. Similar results show up in a repeated experiment. From the study we believe that humidity could be a possible issue bringing film defects but it is definitely not a key factor. Something more important must hind behind it.

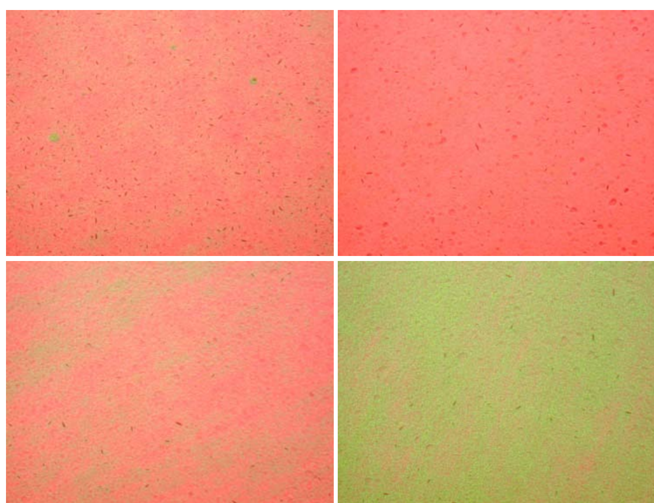

Figure 2.42: Surface qualities of PZT thin films sintered after open air (upper left), vacuum (upper right), dry box (lower left), and hot plate (lower right) drying methods

Drying Temperature and Time

If taking another look at above results, the PZT thin film dried through hot plate is still somewhat better than others. This gives us a hope since pyrolysis technique also adopts the same idea for PZT deposition. In retrospect, conventional thin-film PZT sintering takes advantage of direct RTA by quickly increasing the thermal temperature for a fast PZT crystallization. It is believed that large PZT grain size can be obtained through this method, but the process also addresses large residual stress inside the PZT film due to the CTE mismatch with bottom

electrode. Pyrolysis, as an alternative heat treatment, has been continuously proposed and conducted by many researchers simply because it can actively minimize the layer stored stress and avoid thin film crack initiation and propagation [155,156]. But it is also noticed that low temperature heating of pyrolysis undoubtedly constrains the initial PZT grain growth and may potentially affect the performance of derived film. Unlike directly RTA firing the film outside-in, pyrolysis provides a bottom-up heat source under the substrate using hot plate. Spin-coated PZT gel film is warmed up by one or series low heat treatment (typically 150 - 400 °C) on hot plate undergoing volume shrinkage by driving solvent and organics. Under this way PZT gel film will gradually cure to accommodate the CTE mismatch and avoid huge internal stress generation. After pyrolysis, the residue remaining on the electrode is an amorphous Pb/Zr/Ti polymeric network. Lately sintered by RTA, the network will be converted to condensed PZT crystal film in pervoskite phase. Considering the concept, previous failure is probably related to the improper heating profile. Since one layer PZT coating in the fabrication is around 0.4 µm, a baking at 200 °C for 2 minutes may be too aggressive that fast seals the top surface of gel film and locks the solvent inside. A careful adjustment of the combination of its drying temperature and time may provide a satisfied solution.

Another experiment is serially conducted on four pieces of substrates diced from same wafer (SI-196) baring island bottom electrode. Various drying combinations of temperatures and times are empirically selected; see Table 2.18. If the understanding is right, the experiment results should provide a promising trend for producing good films. However, after final sintering films through different drying combinations are all disqualified in same degree; see Figure 2.43. No sign shows the problem of constant low PZT yield has been alleviated since dimples and black dots are still observed in large area across the whole films surfaces. This proves that the productivity of PZT thin film is not much sensitive to the drying temperature and time as long as aggressive pre-heating is employed. On the other hand, upon the knowledge, many PZT defects are intrinsically related to sol-gel PZT aging. It remains interests that how great effect will be induced by applied sol-gel PZT under various aging status.

Table 2.18: Empirical parameters for drying temperatures and times effect study

Wafer No.	Piece No.	Pt/Ti Porosity	Sol-Gel Type	Aging (Day)	Humidity (%)	Dry Method	Dry Time (Min)	Dry Temp. (°C)	RTA Temp. (°C)	RTA Time (Min)
SI-196	1	Island	Non-diluted	61	34	Hot Plate	1	100	650	15
	2	Island	Non-diluted	61	34	Hot Plate	2	100	650	15
	3	Island	Non-diluted	61	34	Hot Plate	1	150	650	15
	4	Island	Non-diluted	61	34	Hot Plate	2	150	650	15

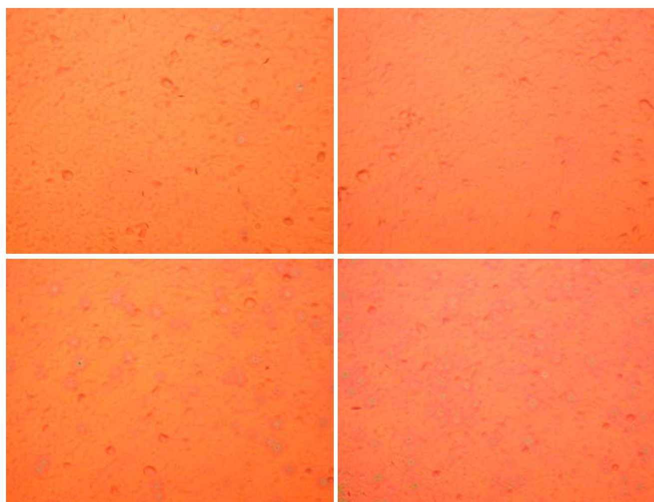

Figure 2.43: Surface qualities of sintered PZT thin films after hot plate dry at 100 °C for 1 minute (upper left), 100 °C for 2 minutes (upper right), 150 °C for 1 minute (lower left), and 150 °C for 2 minutes (lower right)

Age of Sol-Gel PZT

Considering the available sol-gel PZT might be out of dated, another fresh sol is promptly prepared. It is a just-aged (5 days) solution comparing with previous long term aged (61 days) one. Past experience clearly shows that both under aged and over aged sol-gel PZT have great possibilities forming unexpected metal salts. These dendritic crystals of lead acetate hydrate will cause film black dots or cracks when gel film is directly RTA sintered. So a well prepared sol-gel PZT should avoid long term storage. Quick consumption within one month right after preparation is highly recommended.

For experiment consistency, another diced wafer (SI-197) with island Pt/Ti is picked and spin-coated with new sol. Meanwhile, same hot plate drying profile is kept to encounter potential effect from environmental humidity and CTE mismatch; refer to the Table 2.19. The

collected new PZT thin film through RTA firing does not reveal any quality improvement; see Figure 2.44. This totally conflicts with our prediction. Now the question remains open that whether PZT yield is really independent to sol-gel aging period or its effect is just temporarily constrained by hot plate drying.

Table 2.19: Empirical parameters for sol-gel PZT aging effect study - I

Wafer No.	Piece No.	Pt/Ti Porosity	Sol-Gel Type	Aging (Day)	Humidity (%)	Dry Method	Dry Time (Min)	Dry Temp. (°C)	RTA Temp. (°C)	RTA Time (Min)
SI-196	1	Island	Non-diluted	61	34	Hot Plate	1	100	650	15
SI-197	1	Island	Non-diluted	5	27	Hot Plate	1	100	650	15

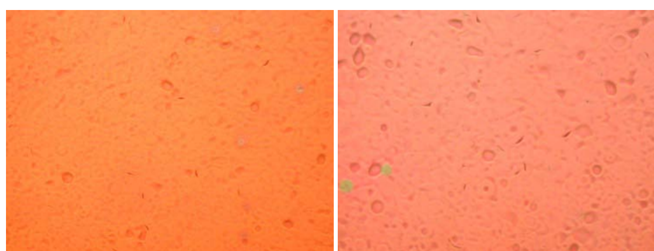

Figure 2.44: Surface quality of sintered PZT on island bottom electrode. Thin films are derived from long term aged sol (left) and fresh sol (right) after hot plate dry.

With the curiosity, second group test is carried out by simply repeating the experiment but removes the hot plate contribution; refer to Table 2.20. Two sol-gel coated wafer substrates adopt conventional open air dry and are consequently RTA fired. According to Figure 2.45, the observed results uncover some useful information. First, comparing between two testing groups, those PZT thin films fabricated with the absence of bottom-up heating have relatively larger size of dimples and cracks. This confirms early understanding on humidity effect. Second, comparing within the group, new sol has no remarkable privilege to produce better thin-film PZT no matter with or without hot plate drying. This means when sol-gel PZT is well prepared its aging period related impact on PZT quality is insignificant.

A possible challenge against the second conclusion may come from the awareness of humidity change included in the second group test. Moreover, the wide applicability of such conclusion still remains doubtful. Thus an additional more serious test for repeatability seems necessary.

Table 2.20: Empirical parameters for sol-gel PZT aging effect study - II

Wafer No.	Piece No.	Pt/Ti Porosity	Sol-Gel Type	Aging (Day)	Humidity (%)	Dry Method	Dry Time (Min)	Dry Temp. (°C)	RTA Temp. (°C)	RTA Time (Min)
SI-197	4	Island	Non-diluted	5	27	Open Air	15	22	650	15
SI-199	1	Island	Non-diluted	38	32	Open Air	15	22	650	15

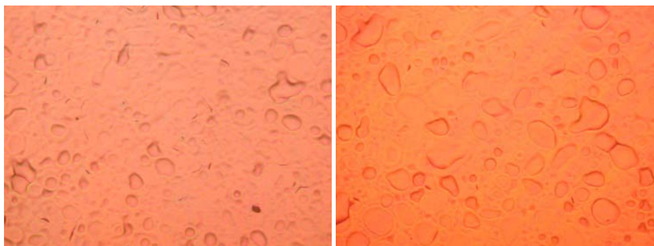

Figure 2.45: Surface quality of sintered PZT on island bottom electrode. Thin films are derived from fresh sol (left) and long term aged sol (right) after open air dry.

A brand new platinized wafer (SI-169) with low Pt/Ti porosity is randomly picked for parallel group study. The wafer is evenly diced into quarters and grouped in two. In each group, one substrate is selected for new sol spin-coating while the other is applied with the old one. Before sintering, first group is hot plate dried (Table 2.21) and those in second group are open air dried (Table 2.22). All specimens are processed under same high environment humidity and then RTA sintered together.

Table 2.21: Empirical parameters for sol-gel PZT aging effect study – III

Wafer No.	Piece No.	Pt/Ti Porosity	Sol-Gel Type	Aging (Day)	Humidity (%)	Dry Method	Dry Time (Min)	Dry Temp. (°C)	RTA Temp. (°C)	RTA Time (Min)
SI-169	1	Low	Non-diluted	20	40	Hot Plate	1	100	650	15
	3	Low	Non-diluted	85	40	Hot Plate	1	100	650	15

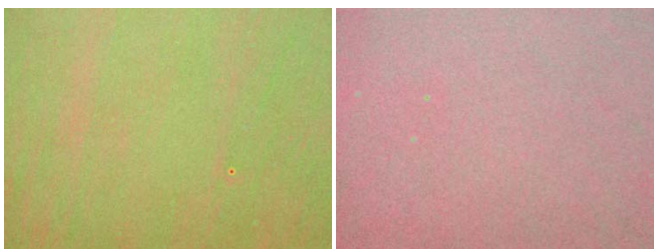

Figure 2.46: Surface quality of sintered PZT on low porous bottom electrode. Thin films are derived from fresh sol (left) and long term aged sol (right) after hot plate dry.

New testing results successfully echo previous conclusion. In addition, they provide a more attractive clue. Considering the only change of bottom electrodes from island to low porous, corresponding PZT thin films deposited on them have drastically improvements; see Figure 2.46 and 2.47. Electrode with certain micro morphology seems dominating other evaluated parameters and has a much greater impact on PZT quality.

Table 2.22: Empirical parameters for sol-gel PZT aging effect study - IV

Wafer No.	Piece No.	Pt/Ti Porosity	Sol-Gel Type	Aging (Day)	Humidity (%)	Dry Method	Dry Time (Min)	Dry Temp. (°C)	RTA Temp. (°C)	RTA Time (Min)
SI-169	2	Low	Non-diluted	20	40	Open Air	15	22	650	15
	4	Low	Non-diluted	85	40	Open Air	15	22	650	15

Figure 2.47: Surface quality of sintered PZT on low porous bottom electrode. Thin films are derived from fresh sol (left) and long term aged sol (right) after open air dry.

Bottom Electrode Porosity (With Proper Surface Microstructure)

Inspired by the discovery, several diced wafer substrates with various porosities on Pt/Ti bi-layer bottom electrodes are picked for parallel study. All of them are first simultaneously spin-coated by individually aged sol-gel PZT, and then sequentially open air dried and RTA sintered; refer to Table 2.23. It is for sure that different sol aging period and environment humidity will more or less affect PZT thin film quality, but through careful studies their influences are proved to be minor and may be ignored. In the upcoming test, it will be more interesting to see whether deposited PZT gradually increases its yield when the degree of bottom electrode porosity constantly drops.

Table 2.23: Empirical parameters for bottom electrode porosity effect study

Wafer No.	Piece No.	Pt/Ti Porosity	Sol-Gel Type	Aging (Day)	Humidity (%)	Dry Method	Dry Time (Min)	Dry Temp. (°C)	RTA Temp. (°C)	RTA Time (Min)
SI-198	1	Island	Non-diluted	38	32	Open Air	15	22	650	15
SI-195	1	Island	Non-diluted	38	34	Open Air	15	22	650	15
SI-194	1	High	Non-diluted	38	27	Open Air	15	22	650	15
SI-181	1	High	Non-diluted	2	27	Open Air	15	22	650	15
SI-167	4	Low	Non-diluted	10	29	Open Air	15	22	650	15
SI-249	1	Low	Non-diluted	7	27	Open Air	15	22	650	15

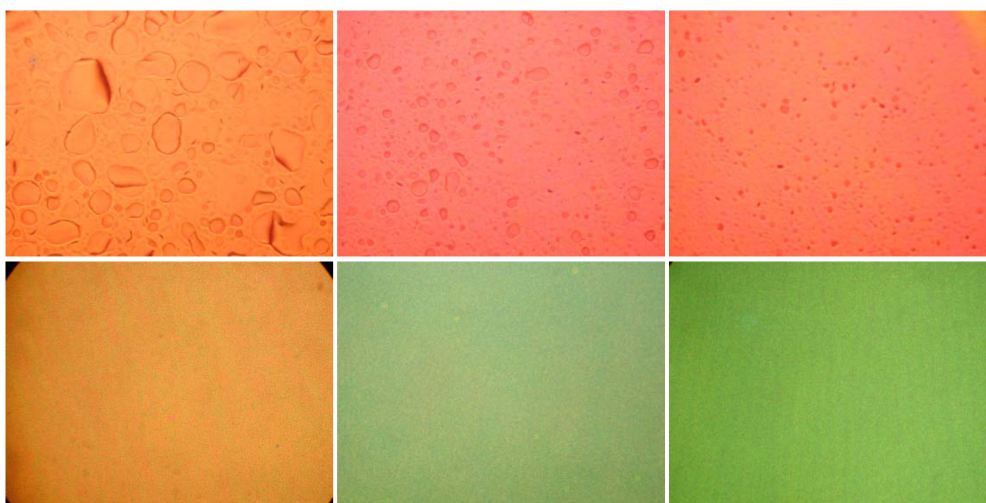

Figure 2.48: Surface qualities of sintered PZT thin films on island (upper left and upper middle), high porous (upper right and lower left), and low porous (lower middle and lower right) bottom electrodes after open air dry.

Fortunately, this time the outcome results quite match our predictions. It clearly shows that the quality of derived PZT film has been continuously modified (Figure 2.48) once degree of electrode porosity on Pt/Ti bi-layer bottom in micro level turns from high to medium, and low, respectively; see Figure 2.49. Figure 2.50 illustrates the corresponding calculations of degrees of porosity on various bottom electrodes through use of MATLAB® R2010a image processing tools. The study once again proves that porosity of bottom electrode surpasses humidity and sol-gel aging effect becoming a key parameter that independently determines the thin-film PZT quality.

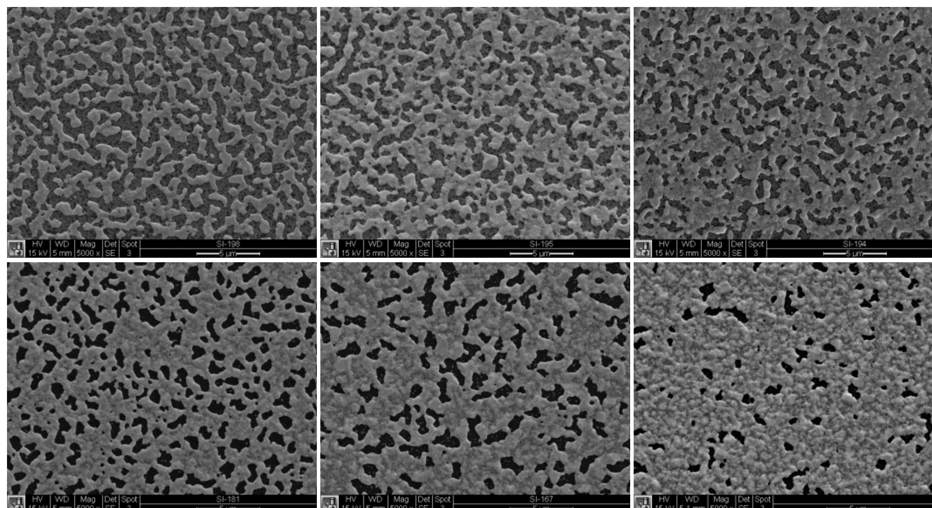

Figure 2.49: SEM pictures of bottom electrodes with high porosity (upper left and upper middle), medium porosity (upper right and lower left), and low porosity (lower middle and lower right).

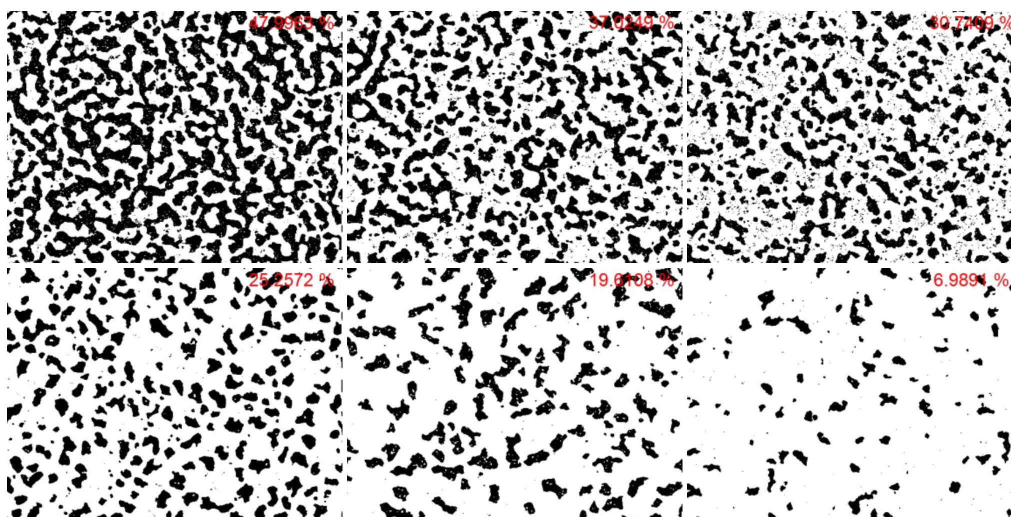

Figure 2.50: Calculated degrees of porosities on bottom electrodes with high porosity (upper left and upper middle), medium porosity (upper right and lower left), and low porosity (lower middle and lower right) via MATLAB® image processing.

Bottom Electrode Wettability

Not like just discussed parameters, the effect of bottom electrode wettability can be observed right after spin-coating. Higher electrode wettability ensures better sol-gel PZT adhesion and uniformity. However, when surface property of Pt/Ti turns hydrophobic, sol-gel spread on it will become discrete and form bumps due to the liquid surface tension. This can be significantly improved by two different approaches. First way is to physically creating surface

micro structures through bottom electrode annealing. It is noticed that coarse micro structures on Pt/Ti bi-layer will effectively enhance the electrode hydrophilicity. Second method is to modify electrode surface property by wet chemical such as Nano-Strip™ or EKC830™ (positive photoresist remover, DuPont EKC Technology, Inc.). Chemical bath treatment is intentionally used for substrate cleaning. In addition it can also induce the formation of C=O and OH functional groups on the Pt/Ti surface and generate a more wettable electrode. However, lab experiences imply that not all kind of acids and bases can be adopted with same functionality. Standard Clean 1 (SC1), a solution of ammonium hydroxide (NH_4OH), hydrogen peroxide (H_2O_2), and water (H_2O) at 1:1:5 ratios, could be one typical example. SC1 is commonly served as thin oxide film removal agent. When annealed porous Pt/Ti bottom electrode is soaked in the buffer, rather than promoting the electrode wettability, SC1 will penetrate the pores and slowly attack the silicon oxide (around 0.3 nm / min at 70 °C). Within few minutes, bottom electrode begins to lose firm connection to the silicon wafer and starts falling off. We'll chalk it up to a rookie mistake since we did ruin several samples in this way even with the knowledge of SC1.

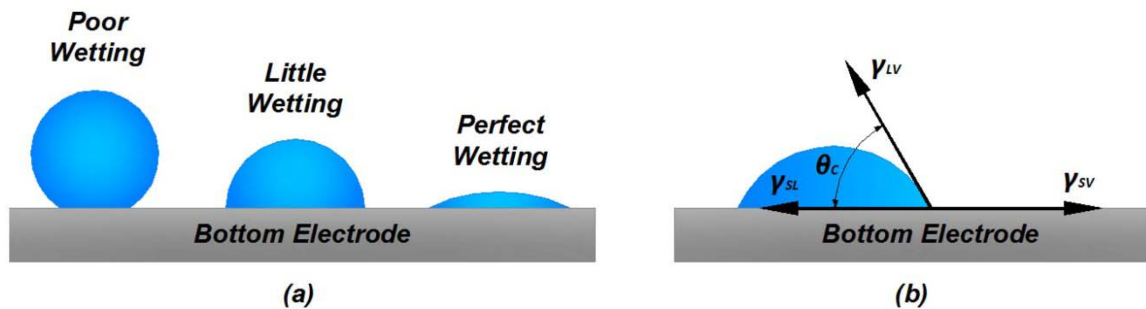

Figure 2.51: Bottom electrode wettability. (a) Contact angles and liquid droplet profiles under different surface wetting conditions. (b) Quantitative measurement of contact angle of liquid droplet wetted to an ideal flat solid surface.

Wettability of electrode surface can be quantified by the contact angle ϑ_c of a liquid that is in contact with it; see Figure 2.51(a). Its concept is mentioned in doctoral dissertation by Chia-Che Wu [157]. The contact angle for an ideal flat and smooth solid surface can be determined by the Young-Dupré equation [158]

$$\gamma_{SV} = \gamma_{SL} + \gamma_{LV} \cos\theta_C \tag{2.19}$$

where γ_{SV}, γ_{SL}, and γ_{LV} are the interfacial free energy per unit area for the interfaces of solid-vapor, solid-liquid, and liquid-vapor, respectively; refer to Figure 2.51(b). Provided with the set

terminology, the surface has a high wettability when $0<\vartheta_c<90°$, while $90°<\vartheta_c<180°$ will provide a poorly wettable surface.

Experiment results confirm that both physical and chemical modifications offer great lifts to the bottom electrode wettability; see Figure 2.52. It is clear to see that without chemical treatment contact angles of liquid droplets on an unannealed wafer (RFWASH-8306-B) are notablely larger than those on an annealed wafer (SI-012). After the wafer is cleaned by Nanostrip™, contact angles on the same wafer will dramatically decrease even no annealing is applied. The sol-gel PZT spin-coated on a more wettable bottom electrode will be much smoother; see Figure 2.53.

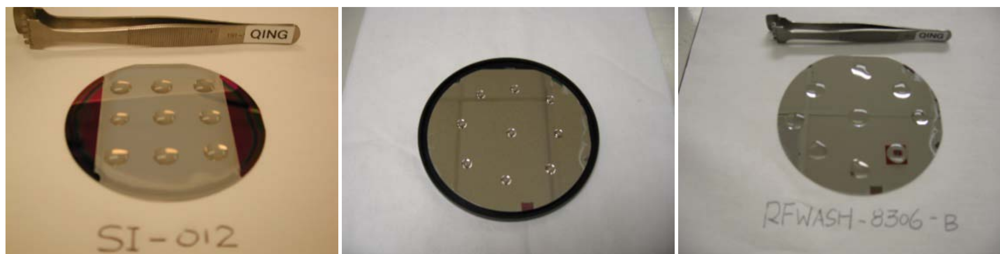

Figure 2.52: Wettability test. From left to right are contact angles of liquid droplets on an annealed wafer without chemical treatment, an unannealed wafer without chemical treatment, and same wafer but with chemical treatment, respectively.

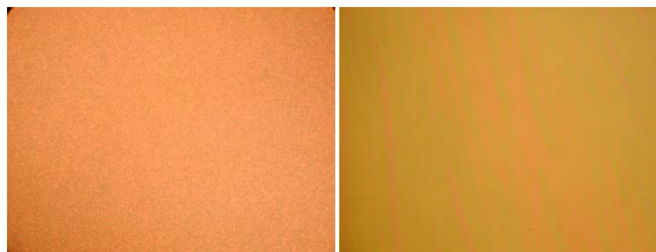

Figure 2.53: Wettability test for comparing the qualities of sol-gel PZT spin-coated on hydrophilic (left) and hydrophobic (right) bottom electrodes.

Conclusion

In general, for the range of the parameters studied above, the porosity of the bottom electrode is proved to be the most crucial factor in minimizing film defects. A satisfied PZT thin film quality is highly related to the degree of electrode porosity. Other parameters, such as drying methods, drying temperature and time, age of PZT sol, and bottom electrode wettability,

have relatively lower impacts. Through careful investigation, the priority order and empirical values of evaluated parameters for fabricating good PZT thin film are determined and summarized in Table 2.24.

Table 2.24: Priority order and empirical value of evaluated parameters

Priority	1st	2nd	3rd	4th	5th
Factor	Bottom Electrode Porosity	Bottom Electrode Wettability	Drying Methods	Drying Temperature and Time	Age of PZT Sol
Base Value	< 20%	< 45°	Hot Plate	100 °C for 1 Min.	> 3 days < 30 days

2.5 Finalization

Finalization is the last touch to the PZT coated wafer. A suitable combination of conductive materials must be built as top electrode on PZT surface. Various techniques are evaluated in the subsequent patterning process. Their adoptions are simply based on the obtained electrodes qualities. Meanwhile, silicon removal on wafer backside is conducted under two different approaches. It demonstrates that deep dry etching could be way complicated but the cavities produce by it are much more compatible with the original design. Undergoing post processing, batch fabricated specimens are fine tuned and diced into individual pieces for the future testing.

2.5.1 Top Electrode Evaporation and Patterning

Top Electrode (Au/Cr Bi-Layer) Evaporation

To turn the prepared thin-film PZT functional, it must be sandwiched in between two electrodes creating a ferroelectric capacitor. Many conductive materials are qualified to be deposited on top of it. Researchers have proposed many types of top electrodes such as platinum (Pt) [159], gold (Au) [160], iridium (Ir) [103], lanthanum nickel oxide ($LaNiO_3$) [161], and indium tin oxide (ITO) [162] as candidates. The combination of Au/Cr bi-layer turns out to be the most popular one possibly because of its wide use throughout the semiconductor industry. Au is not only a chemical stable metal but also easy to operate especially for the post soldering process. Like Ti to Pt, Cr is an ideal bonding material that helps Au receiving perfect connection to the PZT surface.

In our practice, top electrode metallization is conducted in the same E-Beam evaporator (CHA E-Beam Model 822 <Au alloy> or NRC E-Beam Model 3117 <Al Alloy>) that used previous for bottom electrode. Electrode material Au (99.99% pure, 1/8 inch dia. × 1/8 inch) and Cr (99.998% pure, 1-6mm pieces) pellets are still purchased from Kurt J. Lesker® Company. Prior to the metallization, PZT coated wafers are clamped upside down on the planetary and pumped down within the E-Beam chamber for several hours. Once the internal pressure reaches 3.0×10^{-6} Torr, Cr and Au are sequentially evaporated at thicknesses of 25 nm (under rate of 0.1 nm/s) and 500 nm (under rate of 0.5 nm/s), respectively. Au layer is designed to be thick mostly for an easy wiring, but an argument implies that thick Au may affect natural frequency and displacement of later built micro devices [163]. For this reason, a reduction of Au thickness to 100nm is suggested. The melting behaviors for Cr and Au are relatively mild, so there is no need to adjust the E-gun sweep speed (both longitudinal and lateral sweep frequencies are identically set to be zero) during the evaporation. The empirical crucible heating and deposition parameters for Cr and Au are listed in Table 2.25. Figure 2.54 also illustrates the heating profiles for both materials.

Table 2.25: Empirical crucible heating and deposition parameters for Cr and Au

Metal	Step 1: Melting			Step 2: Boiling			Step 3: Deposition	
	Melting Point (°C)	Rise Time (min:sec)	Soak Time (min:sec)	Boiling Point (°C)	Rise Time (min:sec)	Soak Time (min:sec)	Thickness (nm)	Time (min:sec)
Cr	1907	1:00	0:20	2671	0:30	0:20	25	4:10
Au	1064	1:00	1:00	2856	0:20	0:30	500	16:40

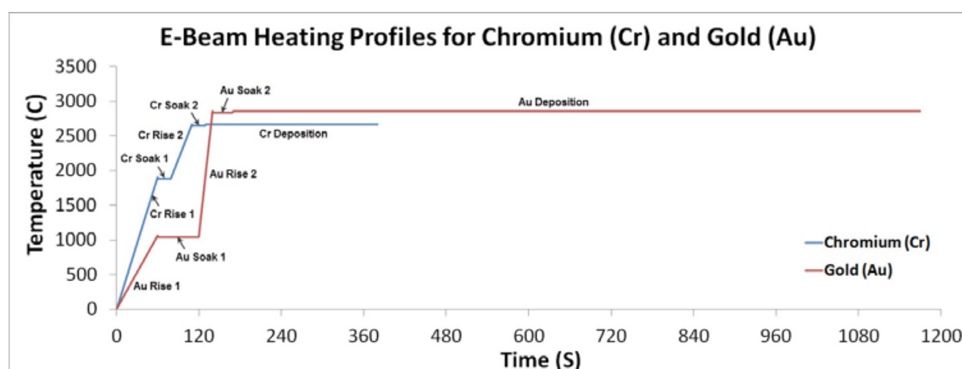

Figure 2.54: Cr and Au heating profiles during E-Beam evaporation

<u>Top Electrode Patterning</u>

The goal of top electrode patterning is to remove unwanted part of Au/Cr bi-layer and create micro structures such as discrete conductive pads on the surface of thin-film PZT. So far there are two major photolithographic approaches frequently conducted by semiconductor industry, which are wet etching and electrode lift-off. We compared both methods and proved that electrode lift-off could be the most suitable one for our fabrication.

When wet etching is selected, the process can be described as follow. First, PZT coated wafer is chemical pre-cleaned and its backside alignment marks is protected by Scotch® brand tape (3M Company) on front side of the wafer; see Figure 2.55(a). Second, after top electrode deposition, Scotch® brand tape is torn off to show the alignment marks; see Figure 2.55(b). Third, P-20 primer (adhesion promoter) and AZ®1518 (AZ Electronic Materials PLC) positive photoresist are spin-coated successively on electrode side by CEE® photoresist spin coater (Brewer Science, Inc.); see Figure 2.55(c). Forth, a prepared top electrode mask is covered on softbake (100 °C for 3 minutes) photoresist and aligned with backside alignment mark through use of ABM IR mask alignment and exposure system (AB-Manufacturing Inc.); see Figure 2.55(d). Fifth, taking advantage of photolithography, unshaded photoresist is exposed under ultraviolet (UV) light for mask pattern transfer; see Figure 2.55(e). Sixth, wafer is soaked in developer consisting of AZ®351 (buffered NaOH, AZ Electronic Materials PLC) and DI water with a 1:4 ratio to wash the degraded photoresist away; see Figure 2.55(f). Seventh, after hardbake (110 °C for 3 minutes), remaining photoresist on top electrode becomes a masking material that resists chemical etching. Wafer now can be immersed in gold etchant (aqua regia, mixtures of nitric acid HNO_3 and hydrochloric acid HCl with a mixing ratio of 1:3) and chromium etchant (mixtures of perchloric acid $HClO_4$ and ceric ammonium nitrate $(NH_4)_2[Ce(NO_3)_6]$) baths to remove unprotected Au and Cr respectively; see Figure 2.55(g). Eighth, wafer with patterned top electrode is submerged in EKC830™ and AZ®300T (AZ Electronic Materials PLC) tanks to strip the positive photoresist; see Figure 2.55(h).

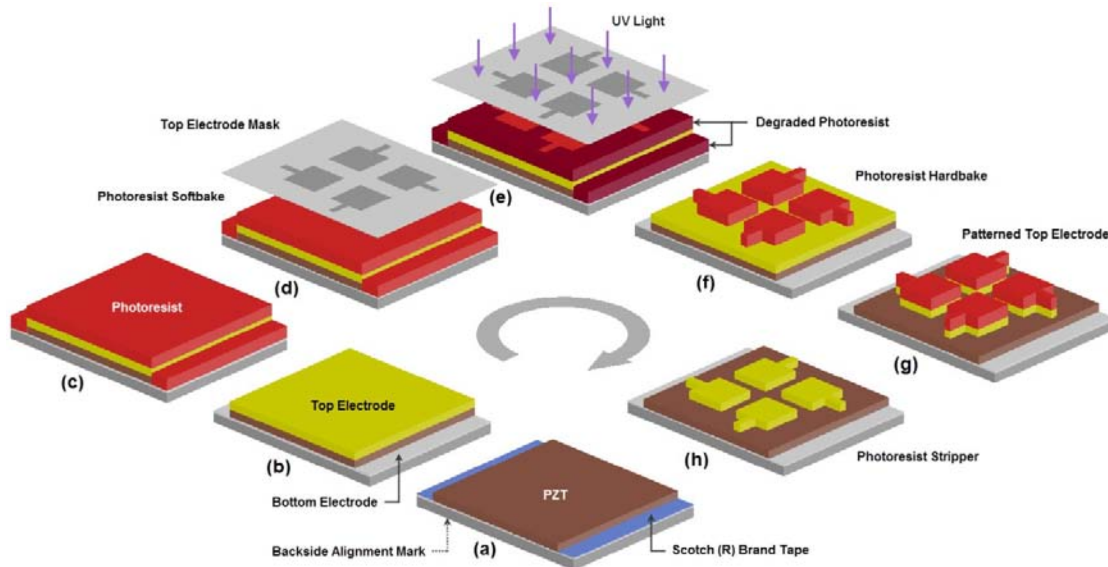

Figure 2.55: Top electrode wet etching fabrication procedure

When Au and Cr etchants are involved in electrode patterning, they are supposed to only attach corresponding materials due to the chemical selectivity (different etch rates in materials). The depth of produced cavities can also be controlled by combining the known etch rate (approximate 3 nm/s for Au etchant and 0.6 nm/s for Cr etchant) and the etching time (approximate 3 minutes for Au etchant and 40 seconds for Cr etchant). However, in the study we continuously find that top electrodes patterned through wet etching remain poor adhesion to PZT. They either have curled up edges or completely fall off. With first guess of inaccurate etch rate, a shorter etching time is once adjusted. But this ends up with a non-through electrode etch. After many trials, the final debugging is targeted on the etching mechanism. As known, Au and Cr are isotropic materials. During the electrode patterning process, the etchants intend to etch the corresponding metals in all directions at same rate. These usually undercut the masking layer and remove extra Au and Cr sideway to form bias with sloping walls; see Figure 2.56. The bias situation becomes even worse especially when wafer in the etchant is frequently agitated to maintain proper etch rate. Given a designed smaller top electrode pad and narrow electrode wire, wet etching will easily scoop all bonding materials Cr out and cause above Au layer falling off.

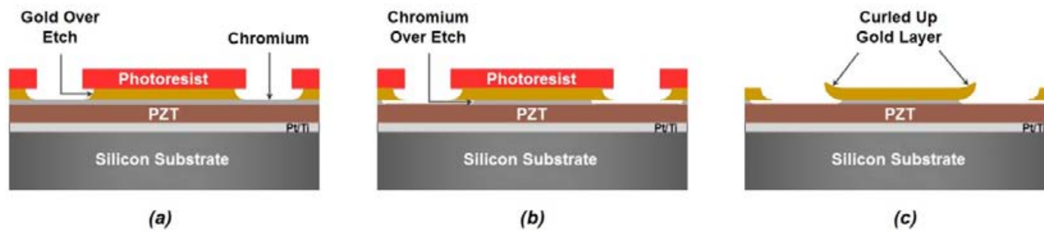

Figure 2.56: Undercut effect during top electrode wet etching process. (a) Gold over etch; (b) Chromium over etch; (c) Curled up top electrode.

For such reason, electrode lift-off is tested below. First, P-20 primer and NR71-1000PY (Futurrex, Inc.) negative photoresist are spin-coated successively on wafer pre-cleaned PZT side (Figure 2.57(a)) by CEE® photoresist spin coater (Brewer Science, Inc.); see Figure 2.57(b). Second, top electrode mask is covered on softbake (150 °C for 1 minute) photoresist and aligned with backside alignment mark under ABM IR mask alignment and exposure system (AB-Manufacturing Inc.); see Figure 2.57(c). Third, mask pattern transferring through photolithography technique is accomplished by exposing and hardening uncovered photoresist under ultraviolet (UV) light; see Figure 2.57(d). Forth, after hardbake (100 °C for 1 minute), wafer is soaked in developer consisting of RD6 (Futurrex, Inc.) and DI water with a 3:1 ratio to dissolve the unstrengthened photoresist and form surface cavities; see Figure 2.57(e). Fifth, Au/Cr bi-layer is deposited at same depth on both photoresist and bare PZT in its cavities; see Figure 2.57(f). Sixth, metalized PZT coated wafer is immersed in acetone tank about 24 hours for washing away the photoresist and Au/Cr bi-layer on it. The remaining metal directly contacts with the thin-film PZT is desired top electrode pad; see Figure 2.57(g).

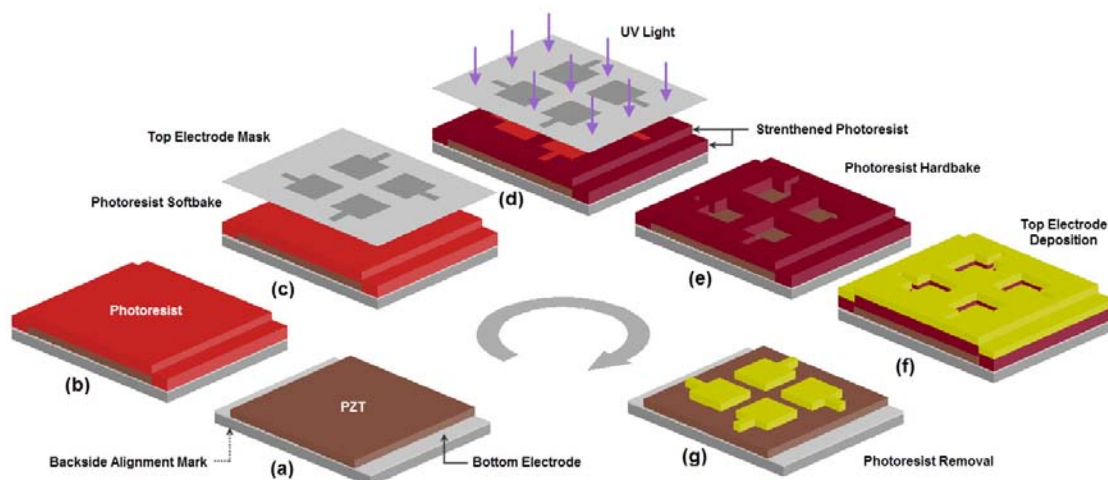

Figure 2.57: Top electrode lift-off fabrication procedure

Lift-off is proved to successfully overcome the previous undercut problem and yield a much stronger top electrode. However, it still has some potential disadvantages. During the photolithography, there is a possibility that part of unwanted photoresist is accidently hardened. Electrode pad sitting on it has a risk to be partially removed; see Figure 2.58(a). Also, for an inverse case, part of required photoresist is accidently stripped off which causes later difficulties of metal removal; see Figure 2.58(b). Another extreme case is related to photoresist geometry. Due to the limit of photolithography, sometimes those microstructures on pattern transferred photoresist layer may take incline wall. When vaporized Au/Cr bi-layer is deposited (for our case, 0.525 µm top electrode vs. 0.7-1.2 µm photoresist), the thick metal is likely to cover the sidewall of the photoresist. This could either prevent acetone from flowing in for above layer lift-off or create several small suspending ears around electrode edges. Sooner or later when these ears curve down to the PZT surface, unexpected short circuits could be connected; see Figure 2.58(c). The last disadvantage is very annoying and somewhat hard to deal with. During the lift-off process, released metal pieces may not float above in the acetone liquid, instead, they sink and reattach with the PZT at many random locations. Once wafer is not carefully collected and dried, these small recaptured metal pieces will never be flushed away.

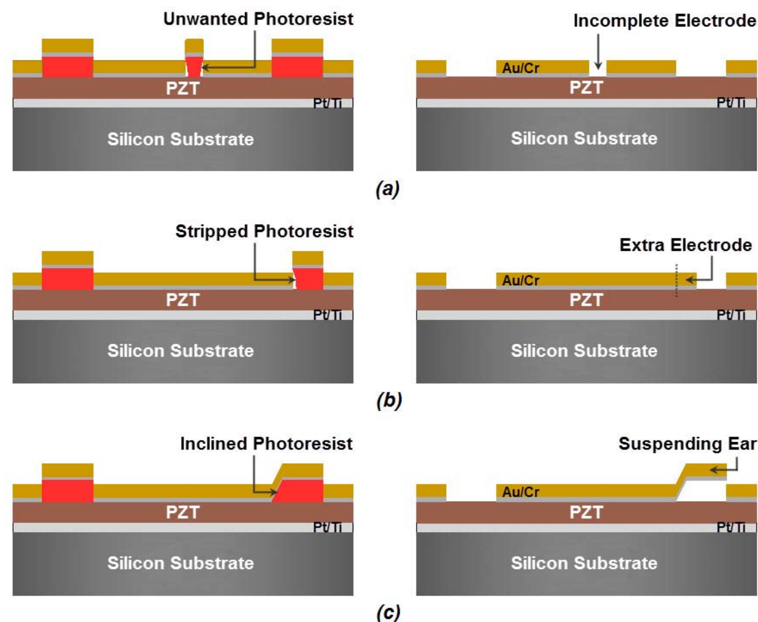

Figure 2.58: Disadvantages of top electrode lift-off process

Up to now, all fabrications focusing on the front side of the wafer are finished.

2.5.2 Backside Deep Wet and Dry Etching

Backside deep etching is the finalizing step of PZT thin film based micro devices, which only touches back side of the wafer. The main purpose of the process is to remove the silicon substrate and release the electrode-PZT-electrode sandwich membrane. In this step, deep wet etching and deep dry etching are commonly adopted.

Deep Wet Etching

The substrate used in fabrication is p-type <100> boron doped silicon wafer which is an anisotropic material. Deep wet etching for this crystal silicon must depend on anisotropic wet etchant such as potassium hydroxide solution (30% KOH in DI water at 80 °C). This is because KOH has a high etching selectivity between <100> (approximate 1.5 μm/min) and <111> (approximate 2.5 nm/min) crystal orientations and ensures the demanding etching rate and direction. From the experiment we find that deep wet etching is much easier to control since KOH hardly attaches silicon nitride (less than 1 nm/min) and silicon oxide (around 10 nm/min). Through the substrate pretreatment, silicon wafer grows oxide and nitride on both sides. Once a designed opening is created on silicon nitride and oxide layer using a combination of photolithography and reactive ion etch (RIE) (Phantom III RIE System, Trion Technology, Inc.), deep wet etching will directly use silicon nitride on this side as an etching mask and that on the other side as an etching stop. Silicon removed this way can also automatically prevent undercut (etchant selectivity) and through etch. But we do find deep wet etching has several unsuitable problems. First one is that KOH can actively react with thin-film PZT and top electrode. If the front side of the wafer is lack of protection, PZT and electrode layer could be both destroyed. Second concerning is the etching result. During deep wet etching, instead of digging a straight cavity, KOH will strictly follow the silicon <111> plane and leave a sloping sidewall at an angle of 54.7° to the <100> wafer surface; see Figure 2.59(a). It means if a membrane is released by deep wet etching, substrate beneath must take a much larger outline size to hold the cavity especially when the substrate is thick. This is a critical issue and generally unacceptable to most micro device applications.

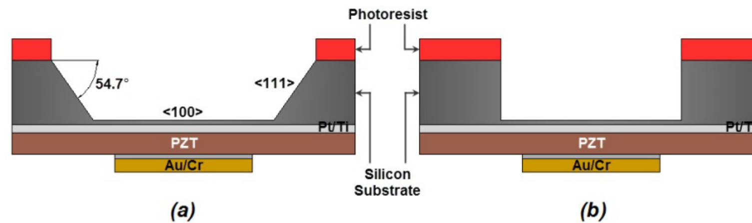

Figure 2.59: Results comparison between deep wet and dry etching

Deep Dry Etching

Unlike wet etching, dry etching has a much different mechanism to guarantee the vertical cavity sidewall; see Figure 2.59(b). Dry etching is often called plasma etching. It etches silicon substrate by accelerating energetic ions of noble gases such as argon (Ar) to bombard on the wafer surface in one direction and knock atoms down. Because the etching is highly directional, the result is unquestionably quite anisotropic.

As is known that plasma etching has no selectivity and will remove whatever materials facing in front of it, thus backside of silicon wafer required to be covered in advance by durable thick photoresist. A combination of P-20 primer and AZ®4620 (AZ Electronic Materials PLC) is selected and spin-coated one after the other. After a two-step softbake (60 °C for 2 minute and then 90 °C for 6 minute), said photoresist layer is mask shaded and exposed under UV light (about 70 seconds) to define etching area. Soaked in developer consisting of AZ®400K (buffered KOH, AZ Electronic Materials PLC) and DI water with a 1:4 ratio for approximate 5 minutes, wafer surface awaiting for cavity opening becomes reachable as those degraded photoresists are gradually dissolved. In the later deep dry etching process, two plasma etchers, RIE (Phantom III RIE System, Trion Technology, Inc.) and deep reactive ion etch (DRIE) (PlasmaPro™ System100, Oxford Instruments PLC), are consecutively used. When patterned photoresist is through hardbake (110 °C for 3 minute), wafer has to be first transported into RIE for silicon nitride and oxide removal (under nitride etching recipe, etch rate on silicon nitride and oxide are 171 nm/min and 34.5 nm/min, respectively) since dry etching recipe carried in DRIE has much lower invasion speed to these two materials. Considering the case, silicon nitride and oxide on the other side of wafer may be qualified as last barrier (etching stop layer) preventing a cavity through etch.

The last step of etching turns out to be problematic since DRIE is designed only holding 4 inches wafer. When a 3 inches wafer is attempted to be transferred into DRIE chamber, it is too small in size to be clamped on the inside load arm. This could be very risky that wafer falls off the load arm and is stuck in the reaction chamber during the internal transportation. Thanks to the contribution from previous researcher, Cheng-Chun Lee [165], who developed a creative technique to get around the problem and give us a new hope. 3 inches wafer must be first flipped over and attached onto one 4 inches wafer at center through use of AZ®4620. After baking together in 110 °C oven for 5 hours, two bonded wafers are placed in the DRIE. This setup makes sure that 4 inches wafer serves as a holding platform well fitting the side of load arm while 3 inches wafer sitting on it receives proper deep etching process. It is noticed that this setup requires careful operation. If 3 inches wafer is initially off centered on 4 inches wafer, there is still a great possibility for joint wafers to slip off the load arm. Another issue is the setup includes extra amount of photoresist. Chances are big that more ion-knocked off photoresist particles turn to polymer powders and fall back to the wafer filling up the deep etched cavity. DRIE has an etching rate on silicon about 0.72±0.06 µm per loop. Considering the thickness of a 3 inches wafer (380±50 µm), 450 loops non-stop rough etching is always set as first round expectedly removing major bulk of silicon (approximate 324 µm). After that, 5 loops per etching round will take place. Since there is a big variation of wafer thickness, a continuous naked eye observation is required after each round of fine etching. The process should not be ceased until the bottom of cavity turns green (silicon nitride on the other side of wafer is reached). This will result a membrane with thickness around 1.5 µm.

Finally, deep etched 3 inches wafer is immersed in acetone tank for at least 24 hours to dissolve the bonding photoresist and detach from 4 inches holding wafer. Post-cleaned by EKC830™, AZ®300T, and DI water rinse, the fabrication of a whole wafer containing tens of designed PZT thin film based microsensors and microactuators is accomplished!

2.5.3 Specimen Post Processing

Just fabricated microsensors and microactuators require special treatment, usually in terms of post processing, to be properly functional. The whole process includes wiring, poling, dicing, and packaging.

The strategy of an optimized procedure is to first identify the qualified candidates on wafer basis since this is the easiest way to connect the devices. Two insulated lead wires are chosen to solder with extraction top and bottom electrodes for avoiding direct membrane touching and breaking; see Figure 2.60. When the soldering iron tip approaches the device, a special care need to be taken since a violent touching or long time soldering may melt and pop out the top electrode.

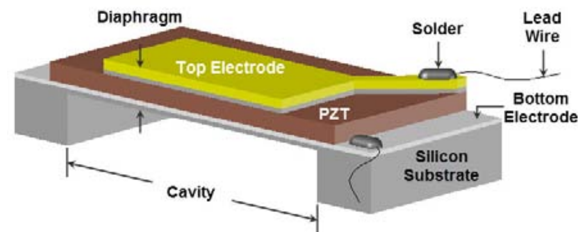

Figure 2.60: Specimen (cross section view) wire soldering

Wired device should be poled for thin-film PZT activation. As a ferroelectric material, ideal PZT crystal possesses a rigid cubic lattice structure where oxygen ions (O^{2-}), lead ions (Pb^{2+}), and titanium-zirconium ions (Ti^{4+}-Zr^{4+}) are located at its corners, centers of facets, and geometric center, respectively; see Figure 2.61(a). However, PZT under this original setup seldom presents satisfied piezoelectricity since all ions are in their neutral status. Poling process can effectively alter the status by generating a bias inside the structure. When PZT based device is applied with 150 KV/cm electric field through direct current (DC) power supply (E3630A, Agilent Technologies, Inc.) and meanwhile heated on a hot plate (Thermolyne Cimarec®, Barnstead International, Inc.) at 90 °C, those positive titanium-zirconium ions will be pulled away from structure center location; see Figure 2.61(b). Under the effect of ions movements, PZT lattice will expand slightly along the axis of the electric field and contracts a little in the side direction. Upon cooling with the electric field still on, such PZT lattice distortion is fixed resulting in a permanent polarization even after the large electric field is switched off. This is more like tare the material with a new zero electric field. PZT treated this way will show much better piezoelectricity and cause larger strain under newly applied field. In the study, we also observed that PZT would easily be depoled once it works under a high temperature condition or a large reverse field that exceeds 70% of poling field strength is applied.

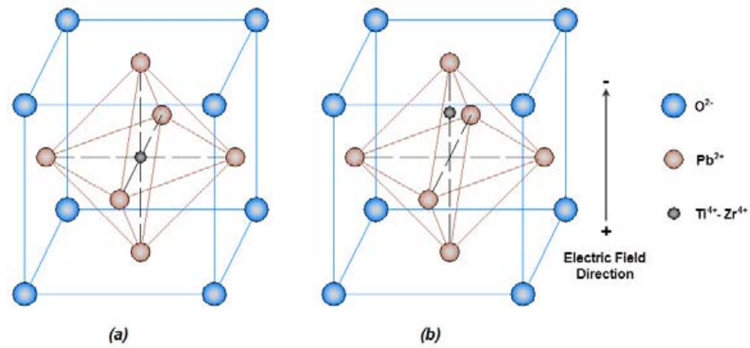

Figure 2.61: PZT crystal lattice structure. (a) Unpoled; (b) Poled.

Wiring and poling processes inevitably sacrifice devices yields since heating and applied field can induce unwanted short circuit. Devices that survive from above two processes will be picked out as good samples and diced off the wafer into many individual units. Dicing saw (K&S 780, Kulicke and Soffa Industries, Inc.) equipped with diamond saw blade (Part Number: 4.6-15A-64RU7-1) is used for device separation. To prevent the cut pieces from flushing away by cooling water, a large blue tape is suggested to attach to the bottom side of wafer for holding all diced units in position.

When wafer is diced into pieces, individual specimen is separated from prepared extraction bottom electrode. To maintain connection with the bottom electrode, lead wire has to be attached sideway to the specimen. Silver paste can be a good substitute since soldering is not suitable on such setup due to the extreme small electrode exposure area. But this method barely provides strong connecting point and sometimes looses contact during thereafter device testing and transportation. Upon the reason, epoxy temporary packaging (5 Minute® Epoxy by ITW Devcon, Inc.) is introduced surrounding the specimen edges. It will not only strengthen the silver paste adhesion point but also encapsulate the bottom electrode and keep it away from the top electrode; see Figure 2.62.

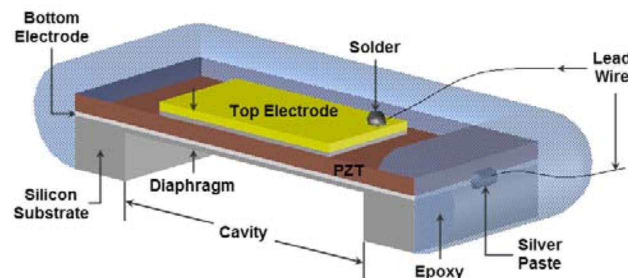

Figure 2.62: Specimen (cross section view) epoxy packaging

2.6 Summary

In this chapter, an entire process for fabricating crack-free thin-film PZT based microdevice is thoroughly investigated and practiced. In the meantime, valuable modifications on key processes are contributed for fabrication improvements.

1. Four major defect types of sol-gel derived PZT thin film are characterized. Through systematic investigation, these defects are strongly tied with the degree of porosity on Pt/Ti bi-layer bottom electrode. It is convincingly proved by the parametric study that such thin-film PZT imperfections will be greatly alleviated when bottom electrode porosity is effectively controlled in a relatively low level (usually less than 20%). In addition, it is also noticed that thin-film PZT defect grade will suddenly uprise when bottom electrode porosity drop to zero.

2. Porosity on Pt/Ti bi-layer bottom electrode can be classified into four major degrees, and it is understood to be a combined effect of many electrode deposition and annealing factors. A careful parametric study has been conducted to prioritize the adjusting order and values of these factors. It clearly shows now Pt/Ti bi-layer bottom electrode through optimized fabrication has a stable trend to bear low electrode porosity while maintaining proper surface microstructure. This is very important to assure the quality of thin-film PZT lately deposited on top of it.

Chapter 3

MEASUREMENT OF PIEZOELECTRIC COEFFICIENT d_{33}

3.1 Introduction

Microactuators driven by Lead Zirconate Titanate ($PbZr_xTi_{1-x}O_3$ or PZT) have received wide attention recently, because they could potentially outperform other MEMS actuators in terms of bandwidth [30-32], energy density [33], and actuation strength. As a result, PZT microactuators enable various new advanced applications, such as minute hearing aids [40,41], miniaturized diagnostic tools [42,43], micropump and microejector [34,35], atomic force microscopy (AFM) [36], and head positioning system of optical and hard disk drive [37,38], and active control system [39]. Moreover, PZT based microsensors have been adopted for many innovative applications, such as energy converter and harvester [44-46], active and passive damage detection [47], and random access memory [48-50]. In scaling down the size to sub-millimeter range, microsensors and microactuators often employ PZT thin films whose thickness is less than 10 μm to maintain a proper aspect ratio. The form of PZT thin films, however, presents a wide range of unique challenges that do not exist in bulk PZT or thick-film PZT (with film thickness more than 100 μm). One of them is measurement and calibration of piezoelectric coefficient d_{33}.

3.2 Challenges

For bulk PZT or thick-film PZT, piezoelectric coefficient d_{33} is often measured in two ways. The first way is to apply an electric field and measure the corresponding strain. In this case, displacement of the PZT surface is often measured via a capacitive displacement probe [166], a laser interferometer [167] or a Laser Doppler Vibrometer (LDV) [168]. Then the normal strain is calculated from the measured displacement.

These methods, however, become impractical for PZT thin films for several reasons. First, normal displacement of PZT thin films is extremely small due to their small thickness in comparison with that of bulk or thick-film PZT. This small displacement is often out of the resolution limit of displacement probes. As a result, the calculated normal strain suffers coarse resolution and low signal-to-noise ratio. Second, laser interferometer measurements highly

depend on surface quality of the PZT sample. The specimen has to be either polished or attached with a mirror to obtain a flat and reflective surface. This proves to be very difficult to realize, when PZT appears in the form of thin films. Third, the measurement of laser interferometer and LDV tend to include a large contribution from substrate bending and distortion, which cannot be accounted for accurately.

The second way to measure d_{33} for bulk or thick-film PZT is to apply a known force and measure the corresponding charge [169]. The applied forces can be either static or dynamic. If a static (i.e., constant) force is uniformly applied over a bulk or thick-film PZT specimen, the stress can be calculated from the applied constant force and the area over which the force is applied. In the meantime, the corresponding charge density can be obtained through the product of the capacitance and voltage of the PZT divided by the electrode area. Theoretically, in the time domain d_{33} is the ratio between the charge density and the stress.

Alternatively, a dynamic force can be applied to a bulk or thick-film PZT specimen via a mechanical shaker [166], as typically done in d_{33} meters or charge measuring rigs. In this case, the instrument first applies a constant preload to hold the PZT specimen. Then it varies the applied load harmonically at an AC frequency that is above the cutoff frequency of the PZT *RC*-circuit but below the resonance frequency of the specimen. In the instrument, a load cell measures the varying applied load and a charge amplifier records the charge. Then d_{33} can be calculated using the same method described above for the constant force measurement.

Both static and dynamic measurement methods become impractical for PZT thin films. In the case of static forces, PZT thin films often have a much smaller time constant than bulk or thick-film PZT. As a result, the measured charge decays very quickly and is difficult to measure accurately in the time domain. Moreover, as PZT becomes thin (e.g., 1 μm), the output voltage is significantly reduced and the signal-to-noise ratio drops. To reduce the noise, a very large force is needed in the measurements. The large force could, in turn, fracture or depolarize the PZT thin films [169].

In the case of d_{33} meters (i.e., dynamic forces), d_{33} meters frequently fracture PZT thin film specimens when the static preload is applied. If the specimens survive the preload, d_{33} meters often penetrate the top electrode during the measurement phase due to the friction between the meter's probe and the specimen. Moreover, the measurements from d_{33} meters vary

substantially from point to point on the same specimen (if the specimen survives the preload and the friction). This primarily results from the fact that thin film specimens often take the form of a thin plate instead of a thick block. Consequently, dimensions, geometry, measurement locations and boundary conditions of the specimen can significantly affect the measured results.

Aside from these "operational" difficulties, measurements of d_{33} from PZT thin films also have their own unique challenges. For example, piezoelectric coefficients of PZT thin films can vary significantly on residual stresses [170,171]. PZT thin films could easily be depolarized during testing when excessive forces are applied [169]. PZT thin films must be tested integrally with its substrate; therefore, the test results will bear certain dependence on the substrate's geometry, material properties and boundary conditions [172].

Facing these challenges, researchers have been developing innovative methods to measure piezoelectric coefficients of PZT thin films [173-177]. One approach is to use simple instrumentation and subsequently correct the effects from the substrate. For example, Lefki and Dormans [29] apply a static force ranging from 0 to 20 N via a metallic tip with 1 mm^2 area to a PZT thin film integrated on a silicon substrate. In return, they measure responding charge Q from the PZT film, and calculate the charge-force ratio known as $d_{33}(dp)$ in the paper. Since the substrate is present, the measured $d_{33}(dp)$ is different from the true piezoelectric coefficient d_{33} of the PZT film. Alternatively, Al-Ahmad and Plana [174] applied two electric fields (parallel-mode and anti-modes) to PZT thin films and measure the variation in capacitance due to the two opposite orientations of the bias voltage, from which the piezoelectric coefficient d_{33} are derived. Although this method is simple and straightforward, it relies on many assumptions (e.g., stress-free condition and $d_{33}=2d_{31}$) and completely ignores the effects of substrate.

The second approach is to use advanced experimental setup to minimize the effects of the substrate. Park et al. [175] use pneumatic loading to induce electric charge to characterize d_{33}. The advantage of this method is that a uniform and non-contact force is applied via the pneumatic loading. This method, however, requires significant hardware (e.g., air chamber). Also, the seals (e.g., O-ring) used in the application could potentially induce in-plane stresses affecting the measured d_{33}. Park et al. also do not devise a solution to compensate for the effects of the substrate. Kholkin et al. [176] and Chao et al. [177] use a dual-beam scanning laser interferometer to measure thickness change ΔL of a PZT film induced by an electric field. The

piezoelectric coefficient d_{33} is then derived using $d_{33}=\Delta L/V$, where V is the applied voltage. Although this method is very appealing, the experimental setup and instrument layout is complicated and expensive. Moreover, the thickness change measured will contain displacement induced by the applied electrical field and responding in-plane stresses simultaneously, according to the theory of piezoelectricity.

From the discussion above, measurements of piezoelectric constant d_{33} of PZT thin films face two major challenges. The first challenge is to eliminate the effects of the substrate. Some of the existing methods only need simple experimental setups, but they cannot completely compensate for the effects of the substrate [173,174]. The other existing methods rely significantly on sophisticate experimental setups to minimize the effects of the substrate [175-177]. The second challenge is the accuracy of the measured d_{33}. How accurate is the measured d_{33}? If d_{33} is measured but its accuracy is not assured, the measured d_{33} has very little value in designing PZT thin-film devices. Hence, there is a strong need for an ideal solution, that is, a simple, cost-effective and yet accurate method to measure piezoelectric coefficient d_{33} of PZT thin films while properly compensating for the effects of the substrate. Such a method is particularly favorable during microfabrication, where the piezoelectric coefficient can be quickly estimated to determine the quality of the fabricated PZT thin films.

This section will address the two major challenges above. Its purpose is twofold. First, a simple and cost-effective method is presented to measure piezoelectric coefficient d_{33} of PZT thin films, with the effect of the substrate properly accounted for. Second, it is important to demonstrate that the proposed measured d_{33} is accurate. We use it to design a PZT thin-film microactuator, whose displacement is validated independently via experiments.

The new method to measure d_{33} is a two-step process. The first step is to use a mini impact hammer (with a load cell) to excite the PZT film. During the excitation, the impulsive force is measured via the load cell and the responding charge of the PZT film is measured through a charge amplifier. The impulsive force has large enough amplitude to ensure a good signal-to-noise ratio, but not so much to cause depolarization of the PZT thin films. Since the impulsive force has extremely short duration (e.g., 200 μs), the discharge effect (i.e., the time constant effect) of the PZT circuit can be ignored. With this method, a digital oscilloscope and a charge

amplifier will be sufficient to complete the measurements. At the end of the experiment, a charge-force ratio can be obtained precisely.

Similar to d_{33} *(dp)* measured by Lefki and Dormans [173], the charge-force ratio will significantly depend on substrate properties and dimensions. Therefore, the second step is to compensate for the effects of the substrate in order to extract the true piezoelectric coefficient d_{33} from the measured charge-force ratio. To do so, one can conduct a finite element analysis of the tested specimen to determine a calibration factor that relates the charge-force ratio to the true piezoelectric coefficient d_{33}.

For the rest of this section, we will first present theoretical foundation and a finite element modeling to quantify the calibration factor. In addition, we will conduct a parametric study to understand how the calibration factor depends on various parameters, such as substrate material, boundary conditions, specimen size, specimen thickness, thickness ratio, and PZT thin-film material. We then explain the experimental setup. We conduct two rounds of experiments to demonstrate the feasibility and accuracy of this method. The first round of experiments is to apply this new method to a disk resonator with thick-film PZT, whose d_{33} is known, to confirm its accuracy. In the second round of experiments, we apply the new method to a PZT thin film deposited on silicon wafer, use the extracted d_{33} to design a PZT thin-film membrane microactuator, and confirm the microactuator's displacement via a laser Doppler vibrometer. This round of the experiment thus proves that the new method can extract d_{33} accurately. Finally, a remark on residual stresses in PZT thin films will be concluded.

3.3 Theoretical Foundation

The analysis below provides a theoretical foundation to justify the use of an impact force to measure piezoelectric coefficient d_{33} of a PZT thin film.

Let us consider an elastic substrate occupying semi-infinite domain in Figure 3.1. The substrate carries a bottom electrode, above which a PZT thin film is coated. Finally, a top electrode occupying a finite area is deposited on the PZT film. The thickness of the two electrodes and PZT film is considered infinitesimal compared with the semi-infinite substrate; therefore, they do not contribute to any stiffness when the substrate deforms under external loads. The polar coordinates r and ϑ define the substrate surface, while coordinate z is normal to

the substrate surface. In addition, z=0 defines the location of the two electrodes and the PZT film. Further, the electrodes are subjected to an open-circuit condition such that no net charge is flowing in or out of the electrode, i.e.,

$$q_3 = \int_A e_3 dA = 0 \tag{3.1}$$

where q_3 is the total charge out of the surface at z=0, e_3 is the electric displacement (i.e., charge density) in the z direction, and the integration can be over the top or bottom electrode.

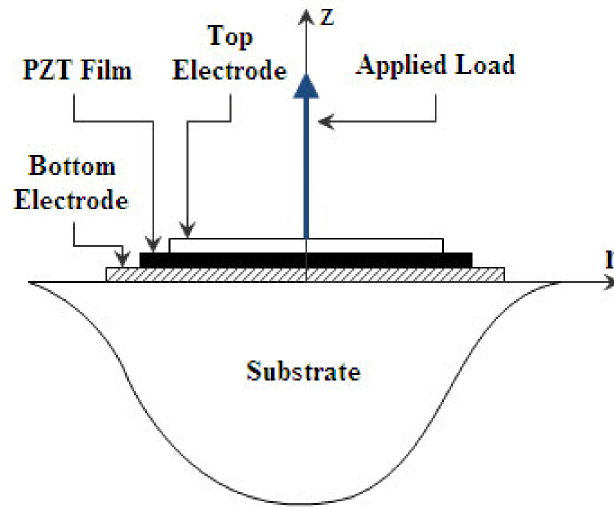

Figure 3.1: Quasi-static analysis of substrate and PZT thin film

Consider the case when an impulsive concentrated load $f(t) = F\delta(t)$ is applied at the origin in Figure 3.1. Assuming a quasi-static condition, Boussinesq's solution of a semi-infinite half space in linear elasticity shows that the stresses on the surface at z=0 take the form of

$$\sigma_r = -\sigma_\theta = \frac{F(1-2\nu)}{2\pi r^2}\delta(t)\,, \quad \sigma_{r\theta} = \sigma_{\theta z} = \sigma_{rz} = 0 \tag{3.2}$$

where σ_r, σ_ϑ are normal stresses, $\sigma_{r\vartheta}$, $\sigma_{\vartheta z}$, and σ_{rz} are shear stresses, and v is the Poisson's ratio of the substrate. In addition, the normal stress σ_z is singular at r=0 satisfying

$$\int_A \sigma_z dA = F\delta(t) \tag{3.3}$$

In this case, the constitutive equation of the piezoelectricity $e_i = d_{ikl}\sigma_{kl} + \varepsilon_{ik}E_k$ is reduced to

$$e_3 = d_{33}\sigma_z + d_{31}\sigma_r + d_{31}\sigma_\theta + \varepsilon_{33}E_3 = d_{33}\sigma_z + \varepsilon_{33}E_3 \tag{3.4}$$

where d_{33} is piezoelectric coefficient, ε_{33} is the dielectric constant and E_3 is the electric field in the z direction. Note that the effect of d_{31} does not appear, because $\sigma_r = -\sigma_\theta$ from (3.2). Substitution of (3.4) into (3.1) results in

$$d_{33} = -\frac{\int_A \varepsilon_{33} E_3 dA}{\int_A \sigma_z dA} \tag{3.5}$$

With a one-dimensional electrostatic analysis,

$$E_3 = V\delta(t)/d \tag{3.6}$$

where V is the voltage and d is the thickness of the PZT film. If we can assume that the PZT film behaves like a parallel capacitor, substitution of (3.3) and (3.6) into (3.5) to obtain

$$d_{33} = -\frac{C_{PZT}V}{F} \tag{3.7}$$

where $C_{PZT} = \frac{\int_A \varepsilon_{33} dA}{d}$ is the capacitance of the PZT film. Note that F and V are the "strength" of the impact and responding voltage. For practical applications, they can be taken as the peak of the impact amplitude or the area underneath the impact history in the time domain.

Equation (3.7) rests on many critical assumptions that may not be realized in experiments. For example, a realistic specimen will not occupy a half-infinite space, and will be subjected to some sort of boundary conditions. The PZT thin film and electrodes will not have an infinitesimal thickness. The impact force applied will not be a point force; instead, it will have a spatial distribution. In light of these realistic constraints, equation (3.7) would take the form of

$$d_{33} = -\alpha\frac{C_{PZT}V}{F} \tag{3.8}$$

where α is a calibration factor associated with the specimen to be tested. If α is determined *a priori* via a finite element analysis, for example, equation (3.8) can be used to extract d_{33}

experimentally free of the effects of the substrate. Also note that $\frac{C_{PZT}V}{F}$ is indeed the piezoelectric coefficient d_{33} *(dp)* measured by Lefki and Dormans [173]. Extracting the true piezoelectric coefficient d_{33} will require a compensation of the substrate effects via the calibration factor α.

3.4 Finite Element Analysis for Thick-Film PZT

We have created several finite element models via ANSYS to evaluate the calibration factor α for various specimens. Figure 3.2 shows a one-fourth model of a specimen, which is a disk resonator consisting of three layers: a brass substrate (also serving as the bottom electrode), a PZT thick film and a top electrode. For the brass substrate, the diameter is 12 mm and thickness is 0.1 mm. It is meshed with solid elements. For the PZT thick film, the material properties are assumed to be PZT-5A. The diameter is 9 mm and the thickness is 0.1 mm. The PZT layer is meshed with piezoelectric solid elements. The top electrode is made of silver with diameter 7 mm and thickness 0.03 mm. It is also meshed with solid elements. The material properties of all layers are listed in Table 3.1 for reference.

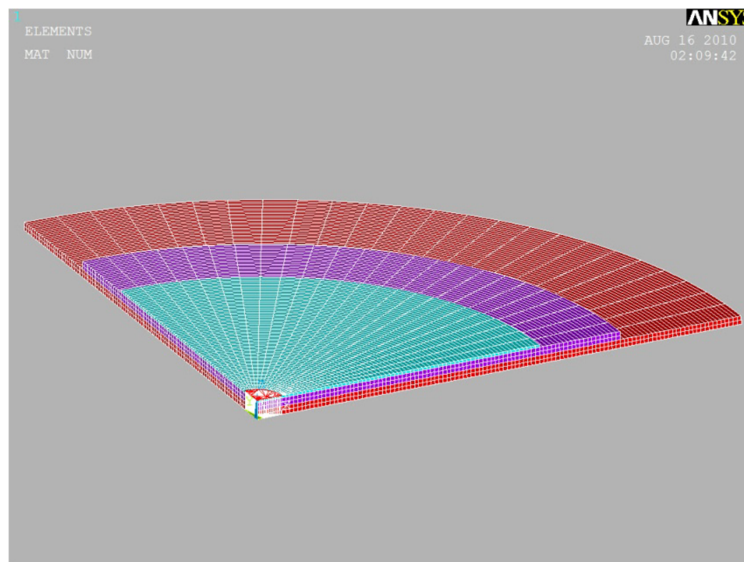

Figure 3.2: Finite element model of circular disk resonator to determine α

Table 3.1: Material properties of all layers used in the FEA for thick-film PZT specimen

	Reference Model			Parametric Studies		
	Top Electrode (Silver)	PZT-5A	Bottom Electrode (Brass)	Silicon	Glue Layer	PZT-5H
Diameter (mm)	7	9	12	12	12	9
Thickness (μm)	30	100	100	100	50	100
ρ (kg/m^3)	1049	7750	8490	2330	1170	7500
d_{31} (m/V)		-1.71×10^{-10}				-2.74×10^{-10}
d_{33} (m/V)		3.74×10^{-10}				5.93×10^{-10}
d_{15} (m/V)		5.84×10^{-10}				7.41×10^{-10}
s^E_{11} (m s^2/kg)		1.64×10^{-11}				1.65×10^{-11}
s^E_{33} (m s^2/kg)		1.88×10^{-11}				2.07×10^{-11}
s^E_{12} (m s^2/kg)		-5.74×10^{-12}				-4.78×10^{-12}
s^E_{13} (m s^2/kg)		-7.22×10^{-12}				-8.45×10^{-12}
s^E_{44} (m s^2/kg)		4.75×10^{-11}				4.35×10^{-11}
s^E_{66} (m s^2/kg)		N/A				N/A
K^T_{11}		1730				3130
K^T_{33}		1700				3400
ε_0 (F/m)		8.85×10^{-12}				8.85×10^{-12}
E (GPa)	83		97	202	2.4	
ν	0.37		0.31	0.33	0.34	

The bottom nodes of the substrate are fixed in the space. Also, interfacial nodes between two adjacent layers are merged to ensure displacement continuity across the interfaces. At the center of the top electrode, a pressure load is applied normal to the electrode over a small area with a diameter of 0.61 mm (to simulate the contact area of a hammer tip to be used in experiments), while the rest of the top electrode is subjected to a stress-free boundary condition. The electric potential of the bottom electrode is set to zero, and the electric potential of the top electrode is assumed to be uniform. Note that the electric potential of the top electrode is unknown, because it will depend on the charge generated from the impact force.

Figure 3.3 shows the charge $Q \equiv -C_{PZT}V$ generated in the PZT layer versus the applied force *F*. (It will be called "charge-force relationship" or simply *Q-F* curve for the rest of the paper.) The straight line with square solid markers is the ideal case depicted in equation (3.7), whose slope is the theoretical d_{33} of PZT-5A, which is 374 pC/N. The straight line with square open markers is from the finite element simulations of the disk resonator predicting a slope of 213 pC/N. As one can see, the finite element simulation does not predict the theoretical slope of d_{33}, because the disk resonator specimen does not satisfy many assumptions made for equation (3.7). According to equation (3.8), the calibration constant of the circular disk resonator is

$$\alpha = \frac{374}{213} \approx 1.7559 \tag{3.9}$$

A parametric study is also conducted to find out what could significantly affect the calibration factor α from the reference configuration above. Parameters considered include substrate material, boundary conditions, specimen size, thickness, thickness ratio, and PZT thin-film material. The parametric study and its results are explained in detail as follows.

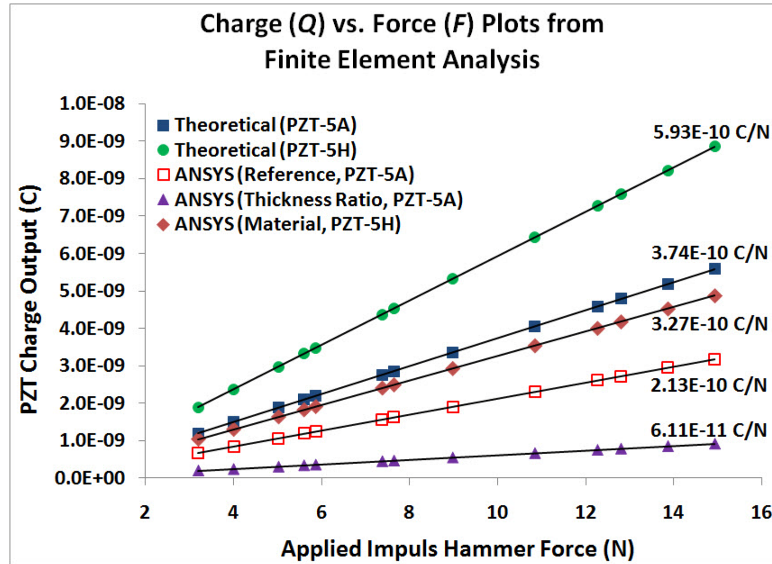

Figure 3.3: Charge (*Q*) vs. force (*F*) plots from finite element analysis

<u>Substrate Materials</u>

The substrate material is changed from brass to silicon. Correspondingly, the Young's modulus is changed from 97 GPa to 202 GPa; see Table 3.1 for detail. The resulting *Q*-*F* curve has a slope of 213 pC/N. Therefore, the substrate material almost does not affect the calibration factor α. To avoid confusion, this result is not presented in Figure 3.3.

<u>Boundary Conditions</u>

In real experiments, the bottom of the substrate may be glued and is not subjected to a perfectly fixed boundary condition. To simulate this, a glue layer is introduced in the finite element model between the substrate and the fixed boundary. The glue layer has a thickness of 0.05 mm and Young's modulus of 2.4 GPa (Table 3.1). With the glue layer, the resulting *Q*-*F*

curve has a slope of 225 pC/N, which leads to a calibration factor α=374/225≈1.6622. This represents a minor 5.3% decrease from the calibration factor α≈1.7559 in equation (3.9).

Specimen Size

In this study, the top electrode, PZT, and brass (bottom electrode) diameter of specimen are reduced from 7 mm to 3 mm, 9 mm to 5.5 mm, and 12 mm to 5.5 mm, respectively, while the thickness of each layer remains unchanged. The resulting *Q-F* curve has a slope of 200 pC/N, which leads to a calibration factor α=374/200≈1.8700. This represents a minor 6.5% increase from the calibration factor α≈1.7559 in equation (3.9).

Thickness Ratio

In this case, the overall thickness of the specimen remains unchanged, but the thickness ratio of the layers is altered. The thickness of the top electrode, PZT, and brass (bottom electrode) is changed to 0.3 μm, 0.673 μm, and 229.027 μm, respectively. In other words, both top electrode and PZT layer are roughly in the same order of magnitude, but are significantly thinner than the substrate. The resulting *Q-F* curve has a slope of 61 pC/N; see Figure 3.3. This leads to a calibration factor α=374/61≈6.1311 representing a significant 250% increase from the calibration factor α≈1.7559 in equation (3.9).

Specimen Thickness

In this case, the thickness of the top electrode, PZT, and brass (bottom electrode) is reduced to 0.339 μm, 1.1313 μm, and 1.1313 μm, respectively. Note that the thickness ratio remains the same as that of the original reference system in Table 3.1. Yet the overall thickness is reduced to about 2.6 μm. The resulting *Q-F* curve has a slope of 223 pC/N, which leads to a calibration factor α=374/223≈1.6771. This represents a minor 4.5% decrease from the calibration factor α≈1.7559 in equation (3.9).

PZT Materials

In this study, the material of PZT is changed to PZT-5H with theoretical d_{33} of 593 pC/N (Figure 3.3). The resulting *Q-F* curve has a slope of 327 pC/N; see Figure 3.3. This leads to a

calibration factor α=593/327≈1.8135 representing a minor 3.3% increase from the calibration factor α≈1.7559 in equation (3.9).

The parametric study concludes that the calibration factor α is only sensitive to the thickness ratio. In other words, the thickness ratio dominates the effects of the substrate. This implies that the calibration factor α can be used to extract piezoelectric coefficient d_{33}, once the thickness ratio of each layer is determined in a specimen. The calibration factor α will be valid for a wide range of piezoelectric and substrate materials. Also, uncertainties in specimen size, thickness and boundary conditions will not significantly affect the calibration factor α and thus the accuracy of this measurement method.

3.5 Experimental Setup and Validation

Figure 3.4 shows the experimental setup to instrument this new method. The setup consists of a mini impact hammer, a charge amplifier, an oscilloscope and a specimen to be tested. The mini impact hammer (made by PCB Piezotronics, Model No. 086E80) has a metal tip with a diameter of 0.61 mm and a load cell with a calibration constant of 22.5 mV/N. When the hammer taps the specimen, the load cell measures the input force and the charge amplifier measures the charge generated by the PZT. Both the measured force and charge are sent to the digital oscilloscope, where their peak amplitudes are recorded. Prior to the experiment, a finite element analysis was conducted to obtain the calibration factor α of the specimen. After the experiment, the piezoelectric coefficient d_{33} is calculated from the peak amplitudes and the calibration factor α according to equation (3.8).

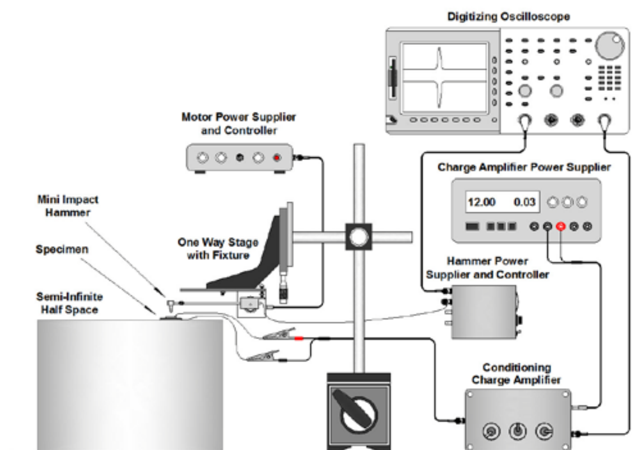

Figure 3.4: Experimental setup for piezoelectric coefficient d_{33} measurement

To test the validity of this new approach, we first choose a thick-film PZT with a known d_{33} as our specimen. The specimen is a commercially available single-layered PZT disk resonator (made by APC International Ltd., Model No. MFT-12T-9.2A1). The disk resonator consists of a brass disk (serving as the substrate and bottom electrode simultaneously), a thick-film PZT layer, and a silver top electrode on the PZT layer, see Figure 3.5. The thickness of the brass disk, the PZT layer and the silver electrode is 0.1 mm, 0.1 mm and 0.03 mm, respectively. The diameter of the brass disk, the PZT layer and the silver electrode is 12 mm, 9 mm and 7 mm, respectively. The specimen is glued to a block of aluminum using epoxy to simulate a fixed boundary condition.

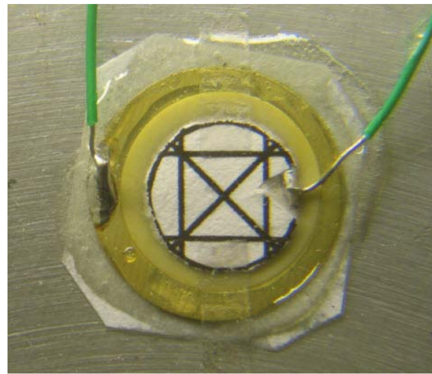

Figure 3.5: PZT disk resonator with lead wires and solder.

According to the manufacturer's claim, the capacitance of the PZT film is 10±30% nF and the film is made of PZT-5A. The exact value of d_{33}, however, is not listed in the specifications. Given a 30% tolerance in capacitance, we assume a 30% tolerance in d_{33}. Since the theoretical value of d_{33} for PZT-5A is 374 pC/N, the piezoelectric coefficient d_{33} of the disk resonator is estimated to be 374±122 pC/N.

During the experiments, the vertical position of the hammer is finely adjusted so that a wide range of impact forces are applied to the specimen in order to obtain the charge-force relationship (i.e., the *Q-F* curve). For each hammer position, at least 20 taps are performed at the center of the specimen, and the peak amplitudes of the measured force and charge are averaged. Figure 3.6 shows some average force and charge measurements as an example. The top and bottom traces are measured force and charge, respectively. With the automatic hammer, the force level can be well controlled. Since 20 measurements are averaged, the measured force and charge are very consistent with very small noise.

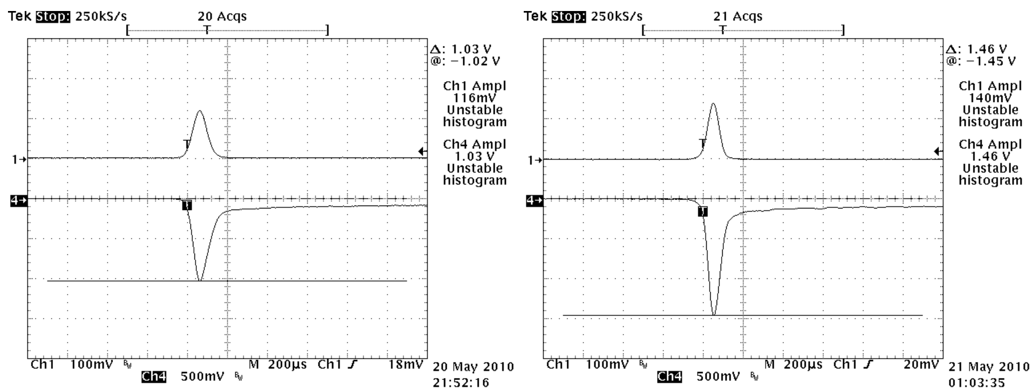

Figure 3.6: Sample of charge-force measurements in time domain for thick-film PZT specimen

After the force (F) and charge (Q) are measured, their peak values are substituted in equation (3.8). Also, the calibration factor α of the PZT thick-film specimen is 1.7559 from the finite element modeling discussed in Section 3.4. Then equation (3.8) calculates the piezoelectric coefficient d_{33} of the PZT thick film.

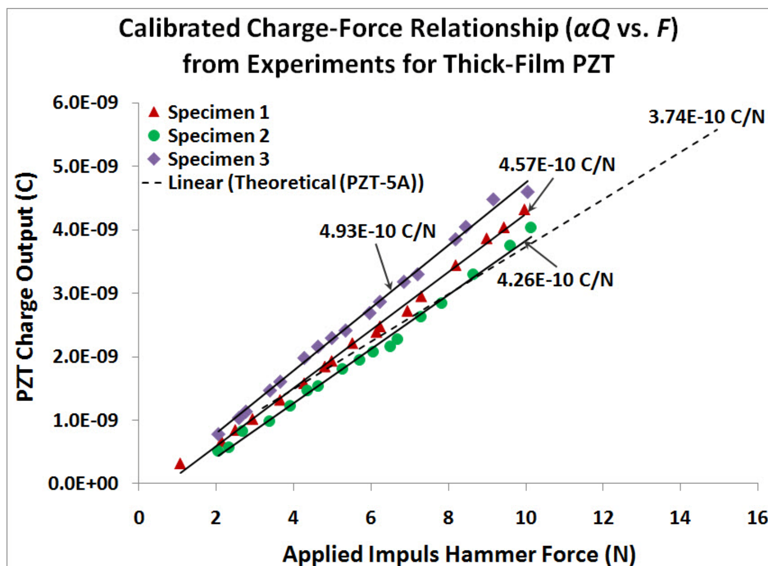

Figure 3.7: Calibrated charge-force relationship (αQ vs. F) from experiments for thick-film PZT

Three thick-film PZT specimens are tested. With α=1.7559, the calibrated charge-force relationship (i.e., αQ versus F) is plotted in Figure 3.7. For each specimen, the markers are from the experimental measurements. The solid lines are from a least-square fit of the experimental measurements, whose slopes give the measured d_{33} according to (3.8). Also plotted in Figure 3.7 is the theoretical charge-force relationship as a reference. The d_{33} obtained from this new approach for the three specimens is 457 pC/N, 426 pC/N and 493 pC/N, respectively. Compared

with the theoretical value 374 pC/N, the measurements from this approach is within the range of 14-32% difference, which is acceptable given that the variation of specimen properties is 30%.

Throughout the experiments, a careful control the magnitude of the impact force is very important. We noticed that a too big impact force could result in depolarization of PZT thick film and affect the consistent d_{33} measurement.

3.6 Applications of d_{33} Measurements to PZT Thin Films

With the demonstrated feasibility of the new method on thick-film PZT, we hereby apply the new method to measure piezoelectric coefficient d_{33} of PZT thin films as follows.

A 3" wafer with a PZT thin film was fabricated strictly following the procedure described in Chapter 2. The only difference is that among three spin-coated PZT layers only first two coatings are derived from non-diluted sol. For the third coating, the sol is diluted 50% by acetic acid and sintering temperature is reduced to 450 °C for 10 minutes. The thickness of the PZT film is measured around 1 µm (first two coatings contribute 0.4 µm per layer while the last coating has thickness about 0.2 µm). After top electrode deposition, the evaporated Au/Cr bi-layer (with a thickness of 25/500 nm) is patterned into multiple electrode pads with dimensions of 3 mm by 3 mm or 4 mm by 4 mm. When the fabrication is complete, the PZT thin film is poled to activate with an electric field of 150 kV/cm at room temperature for 30 minutes. Finally, the wafer is diced into many specimens with dimensions of 5.5 mm by 5.5 mm.

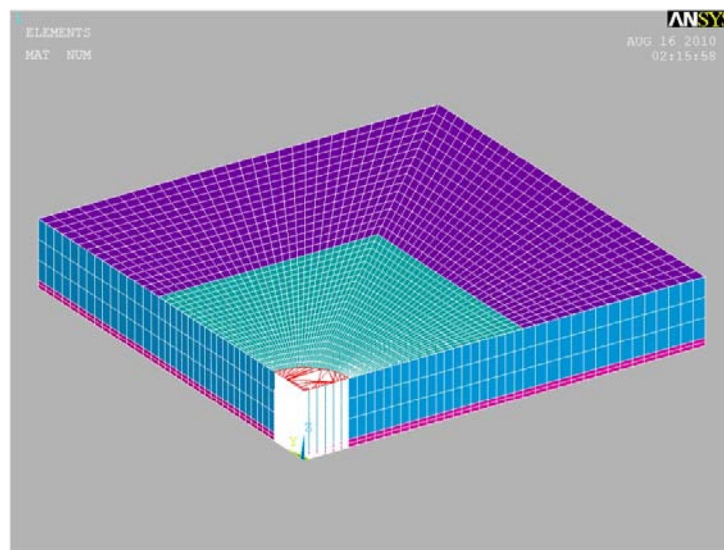

Figure 3.8: Finite element model of thin-film PZT specimen

Based on the geometry described above, we create a finite element model of the thin-film PZT specimen. In Figure 3.8, the finite element model is similar to that shown in Figure 3.2, except that the model now is in square shape and has a separate substrate and bottom electrode. Table 3.2 shows the material properties used in the finite element simulation for the PZT thin film specimen. To obtain the calibration factor, we assume the PZT thin-film material to be PZT-7A with a theoretical piezoelectric constant d_{33} of 153 pC/N. The finite element analysis shows that the charge-force relationship for this specimen has a slope of 59.7 pC/N; see Figure 3.9. Therefore, the calibration factor for the thin-film specimen is

$$\alpha = \frac{153}{59.7} \approx 2.5628 \tag{3.10}$$

Table 3.2: Material properties of all layers used in the FEA for thin-film PZT specimen

	Top Electrode (Gold)	PZT-7A	Bottom Electrode (Platinum)	Silicon	Glue layer
Length (mm)	3	5.5	5.5	5.5	5.5
Width (mm)	3	5.5	5.5	5.5	5.5
Thickness (μm)	0.5239	1.1313	0.2449	385.72	50
ρ (kg/m^3)	19280	7700	21450	2330	1170
d_{31} (m/V)		-0.60×10^{-10}			
d_{33} (m/V)		1.53×10^{-10}			
d_{15} (m/V)		3.60×10^{-10}			
s^E_{11} (m s^2/kg)		1.07×10^{-11}			
s^E_{33} (m s^2/kg)		1.39×10^{-11}			
s^E_{12} (m s^2/kg)		-3.58×10^{-12}			
s^E_{13} (m s^2/kg)		-4.60×10^{-12}			
s^E_{44} (m s^2/kg)		3.40×10^{-11}			
s^E_{66} (m s^2/kg)		2.86×10^{-11}			
K^T_{11} (unitless)		1354			
K^T_{33} (unitless)		617			
ε_0 (F/m)		8.85×10^{-12}			
E (GPa)	80		168	202	2.4
ν	0.42		0.38	0.33	0.34

Two diced PZT thin-film specimens are temporarily packaged according to the technique mentioned in Section 2.5.3 and tested using an impact force ranging from 1.8 N to 10 N. With α=2.5628, the calibrated charge-force relationship (αQ vs. F) derived from the experiment is also added into Figure 3.9 (cf. the triangular markers). The open markers correspond to one specimen and the solid markers correspond to the second specimen. Since the experimental data from the two specimens are so consistent, only one solid line is used to least-square fit the

data. The resulting slope of the least square fit is 21.3 pC/N, which is the measured d_{33} for the fabricated PZT thin film according to (3.8) free of the effects from the substrate.

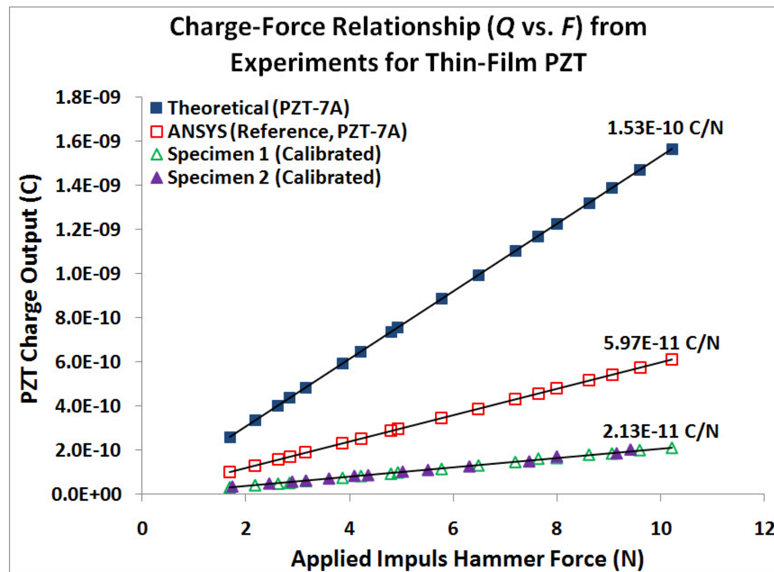

Figure 3.9: Charge-force relationship (Q vs. F) from experiments for thin-film PZT

There are several issues worth noting for these experimental measurements. First, the experimental measurements indicate that the fabricated PZT thin film has very uniform piezoelectric properties. The measurements from two separate specimens from the same wafer show almost the identical slope indicating very consistent d_{33}.

Second, the measured d_{33} from the PZT thin films is significantly less than that of bulk PZT-5A or PZT-7A. It is well known that piezoelectric coefficients of PZT thin films are smaller compared with those of bulk PZT due to smaller grain size of PZT film. Also, sol-gel derived PZT thin films will inherit residual stresses from their fabrication process, which subsequently affect the piezoelectric coefficients [170,171]. Therefore, we believe that the measured d_{33} in Figure 3.9 is reasonable.

Third, it is informative to compare how thick-film PZT and thin-film PZT behave differently to broaden our knowledge base. Table 3.3 lists major dimensions and measured properties of thick-film and thin-film PZT specimens. Although the capacitance of PZT thin film is larger than that of the thick-film PZT (19.3 nF vs. 9.02 nF), dielectric constant and piezoelectric coefficient of the PZT thin film are about one-order-of-magnitude smaller than those of the thick-film PZT (274.15 vs. 2646.77 and 21.3 pC/N vs. 457 pC/N, respectively). These results make sense

because the PZT thin films are fabricated using a sol-gel process. After sintering, PZT thin films are likely to become porous degrading the material properties. Also, a porous bottom electrode could greatly reduce the PZT thin film poling effectiveness yielding a low piezoelectric coefficient. In general, a reduction in dielectric constants often accompanies a reduction in piezoelectric coefficient.

Table 3.3: Comparison of dimensions and properties of thick-film and thin-film PZT specimens

	Thick-Film PZT Specimen	Thin-Film PZT Specimen
PZT Size A_0	63.617 mm^2	30.25 mm^2
Electrode Size A	38.485 mm^2	9 mm^2
PZT Thickness d	100 µm	1.1313 µm
Capacitance C	9.015 nF	19.30 nF
Dielectric Constant ε_r	2646.773	274.15
Force Voltage V_{in}	200 mV	206 mV
PZT Voltage V_{out}	2.08 V	74 mV
d_{33} with Correction Factor	426-493 pC/N	21.3 pC/N

Note: dielectric constant $\varepsilon_r = \dfrac{Cd}{\varepsilon_0 A}$ with $\varepsilon_0 = 8.854\times10^{-12}\ \mathrm{C^2/m^2N}$

3.7 Applications of d_{33} Measurements to PZT Thin Film Microactuators

The measured d_{33} can now be used to design PZT thin-film membrane microactuator shown in Figure 3.10. The microactuator consists of four parts: a membrane, a bulk silicon substrate, a PZT thin film layer, and a pair of electrodes. (Note that the parts in Figure 3.10 are not drawn in proportion.) The membrane is a moving component of the actuator anchored to the silicon substrate. As a result of its small thickness, the silicon membrane has low structural stiffness compared with the substrate. Often, the membrane can be fabricated by releasing part of the bulk silicon substrate for example using DRIE. On top of the membrane is a layer of PZT thin film with a pair of electrodes. When a driving voltage is applied to the electrodes, the PZT thin film extends or contracts in the plane of the membrane, thus creating a bending moment to flex the membrane out of its plane.

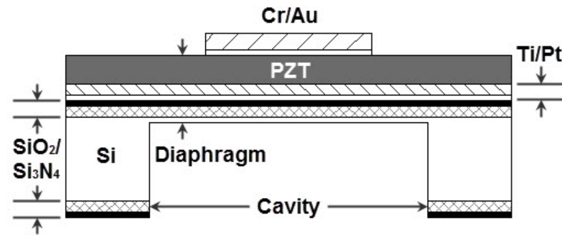

Figure 3.10: Schematic drawing of PZT thin film membrane actuator

Lee et al. [178] has studied the PZT thin-film membrane actuator extensively. Experimentally, the actuator displacement is measured using a laser Doppler vibrometer shining right at the center of the membrane. They also measured actuator dimensions using SEM. Numerically, the actuator displacement is predicted using piezoelectric coefficients from bulk PZT-7A. The numerical predictions, however, disagree with the experimental measurements by an order of magnitude. As a result, the article [178] by Lee et al. serves as an ideal proving ground to validate the accuracy of the newly measured d_{33} in Section 3.6.

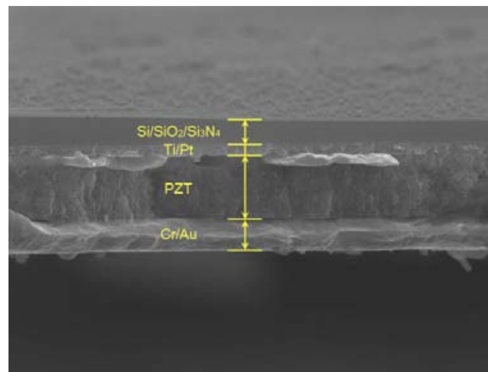

Figure 3.11: SEM cross section view of actuator C4

Table 3.4: Layered structure thickness of the selected PZT actuator membrane

Actuator	C4
$Si/SiO_2/Si_3N_4$	0.48 µm
Ti/Pt	0.19 µm
PZT	1.00 µm
Cr/Au	0.53 µm
Natural Frequency (Experiment)	59.578 kHz
Natural Frequency (FEA, PZT-7A)	40.942 kHz
$\beta \equiv \left(\frac{\omega_{FEA}}{\omega_{EXP}} \right)^2$	0.4722

As a demonstration, let us focus on the actuator C4 described in [178]. The dimensions of actuator C4 is measured under SEM cross section picture (Figure 3.11) and listed in Table 3.4. The dimensions include the thickness of each layer in the actuator. Both real and theoretical natural frequencies are recorded from spectrum analyzer measurement and FEA simulation and also included in Table 3.4. The natural frequency ω_{EXP} measured from the experiment is 59.578 kHz. The natural frequency ω_{FEA} calculated via finite element with the assumption that PZT material is PZT-7A and has same properties as we measured in Section 3.6. The corresponding calculated ω_{FEA} is 40.942 kHz. Figure 3.12 shows measured displacement of actuator C4 with respect to the applied voltage. The response becomes nonlinear when the applied voltage is greater than 4 V. If the measured d_{33} in Section 3.6 is accurate, it will predict the measured actuator displacement below 4 V.

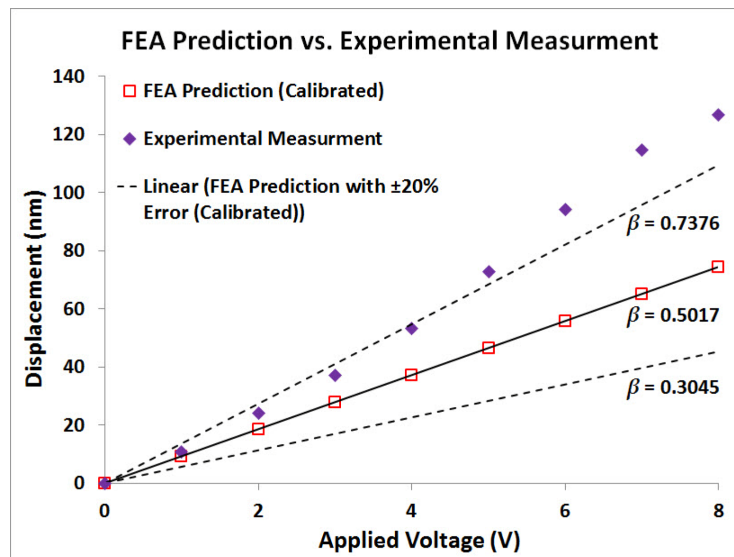

Figure 3.12: Schematic drawing of PZT thin film membrane actuator

To predict the displacement of actuator C4 reasonably, two additional factors must be included: residual stresses and dimension variations. They can be explained in detail as follows.

Significant residual stresses develop in the PZT thin-film membrane actuators. Since PZT is sintered at 650 °C and subsequently cooled down to room temperature, mismatch in coefficients of thermal expansion in different layers results in significant residual stresses. The in-plane residual stresses stiffen the membrane significantly increasing the natural frequency of the actuator. (That is why ω_{EXP} is greater than ω_{FEA} in Table 3.4.) Although the magnitude of the

residual stresses is unknown, its effects on displacement reduction can be estimated via $\beta \equiv \left(\frac{\omega_{FEA}}{\omega_{EXP}}\right)^2$. This is because natural frequency ω is proportional to $\sqrt{k}$, where k is the stiffness of the actuator. In addition, the actuator displacement is proportional to k^{-1}. Therefore, displacement predictions from finite element analysis must be multiplied by the factor $\beta \equiv \left(\frac{\omega_{FEA}}{\omega_{EXP}}\right)^2$ to compensate for the stiffness increase caused by the residual stresses. For actuator C4, the correction factor is $\beta \equiv \left(\frac{40.942}{59.578}\right)^2 \approx 0.4722$.

The thickness of each layer, as measured from SEM, bears an uncertainty too. The dimensions listed in Table 3.4 are measured so that the SEM is perpendicular to the Au layer. If the SEM is oriented such that it is perpendicular to the $Si/SiO_2/SiN_x$ layer, the measured dimensions can vary by 10% to 20%.

With the information above, Figure 3.12 shows the FEA displacement predictions using the measured d_{33} from Section 3.6 (i.e., 23.1 pC/N), correction factor $\beta \equiv \left(\frac{\omega_{FEA}}{\omega_{EXP}}\right)^2$ for the residual stresses (i.e., 0.4722), and 20% variations in measured dimensions of each layer. The dash lines delineate the boundaries when the dimensions of each layer are varied. The measured actuator displacement below 4 V is within the boundaries proving that the measured d_{33} from Section 3.6 is accurate.

3.8 Remarks on Residual Stresses

For PZT thin films, presence of residual stresses can affect the piezoelectric coefficient d_{33} [170,171]. In other words, piezoelectric coefficient d_{33} is a function of residual stresses. Technical speaking, existing methods [173-177] all measure piezoelectric coefficient d_{33} of PZT thin films with residual stresses. Naturally, the following two questions arise. First, does it make sense to measure piezoelectric coefficient d_{33} under the influence of residual stresses? Should one measure piezoelectric coefficient d_{33}, while the PZT film is under a stress-free condition? Second, does the new method presented in this paper remain valid, given that the finite element model does not include any residual stresses?

In so far as the first question, it actually makes more sense to measure piezoelectric coefficient d_{33} while residual stresses are present. When the PZT thin film is in use as a sensor or an actuator, the PZT thin film remains in the state of residual stresses. Therefore, measuring d_{33} with residual stresses will better match the condition that appears in actual devices. As such, the measured d_{33} with residual stresses can be used directly in finite element analyses to improve design or estimate performance of the sensor or actuator.

For the second question, the finite element modeling in Section 3.4 remains valid for thin films with embedded residual stresses. One should note that residual stresses could affect piezoelectric response as well as mechanical response. The finite element analysis in Section 3.4 aims to extract d_{33} from piezoelectric response to account for the effects of residual stresses. The effects of residual stresses on mechanical response should be accounted for via the correction factor $\beta \equiv \left(\frac{\omega_{FEA}}{\omega_{EXP}} \right)^2$ at the device level.

3.9 Summary

1. In this chapter, we have developed and demonstrated a simple and low-cost method to measure piezoelectric coefficient d_{33} of PZT thin films. The method adopts a mini-impact hammer to generate an impulsive force. A load cell at the tips of the hammer measures the impulsive force, and a charge amplifier measures the charge generated by the PZT layer. Prior to the experiment, a finite element analysis is conducted to estimate a calibration constant to compensate for the substrate effects associated with the specimen. From the measured force and charge and the calculated calibration constant, we can estimate the piezoelectric coefficient d_{33} according to equation (3.8).

2. Experimental results on thick-film PZT specimens with known piezoelectric coefficients indicate that the method is accurate. Piezoelectric coefficient d_{33} measured using the new method is well within the specification tolerance. The method also works successfully on PZT thin films without damaging the films. Nevertheless, impact force level needs to be capped to avoid depolarization of the PZT thin films. With the measured d_{33}, we can predict the displacement of PZT thin-film membrane actuators accurately to match with existing experimental results.

3. This new method is distinct from existing measurement methods [173-177] in two aspects. First, it does not require expensive experimental setup, and yet it can accurately compensate for the effects of the substrate. It employs impact forces and averaging techniques. As a result, the measured data do not scatter and have very low noise level. Second, this paper proves that the measured d_{33} is accurate. Simulations based on the measured d_{33} predict the displacement of PZT thin-film membrane microactuators accurately.

Chapter 4

STUDIES ON A NOVEL-DESIGNED NONPOROUS PT/TI BI-LAYER BOTTOM ELECTRODE

4.1. Introduction

With the reference fabrication process, a successful PZT thin film with good quality usually shows a uniform and crack-free surface with the thickness around 400 nm per coat. Defects, however, often occur in the form of bumps, dimples, black dots, cracks, and even delamination.

Our early study indicates that many factors could contribute to the formation of defects. For example, aging of PZT sol could dehydrate essential acidic solvent in the sol thus changing viscosity of the sol during coating. Wettability of the bottom electrode could affect surface tension as solvent evaporates. Drying methods, temperature and duration would affect the rate of evaporation. Mismatch of coefficients of thermal expansion (CTE) between the PZT thin film and the bottom electrode could result in significant residual stresses causing cracks and delamination. Weak interfacial strength between PZT thin film and bottom electrodes could enhance cracking and delamination.

Based on these possible causes, in previous Chapter 2 Section 2.4, we design a parametric study to identify critical parameters that need to be controlled to minimize defect formation. The parameters chosen include drying methods, drying temperature and time, age of PZT sol, and degree of porosity on the bottom electrode. In particular, we are interested in the porosity of the bottom electrode, because it mechanically changes the bonding strength at the PZT/electrode interface.

The parameter space used in the study is as follows. Four types of drying methods are simultaneously attempted, which include air dry, inside a dry box, vacuum dry, and hot plate dry. Drying temperature and duration (limited to the hot plate method) range from 100°C to 150°C and from 1 to 2 minutes, respectively. The age of the sol varies from 5 to 61 days. Three levels of porosity, high, medium, and low, are individually investigated, refer to Figure 2.49. For the high porosity, the bottom electrode becomes many disconnected islands. For the medium porosity, plenty of pores appear on the bottom electrode, but all portions of the electrode remain

topologically connected. For the low porosity, only small amount of pores appear on the bottom electrode.

For the range of the parameters studied above, we find that degree of porosity on bottom electrode becomes the most critical factor in reducing defects. Other parameters, meanwhile, have relatively small impact. To demonstrate the effects of the porosity, Figure 2.48 shows surface quality of the fabricated PZT thin films taken under the optical microscope for different levels of porosity. As the degree of porosity on Pt/Ti bi-layer bottom electrode drops, the PZT thin film surface quality improves significantly. The best outcome, however, does not appear when bottom electrode bears no pores. When the bottom electrode is pore-free, the PZT thin film often delaminates or peels off from the bottom electrode. These observations lead us to believe that some pores are necessary to serve as “anchors” for the PZT thin film to latch sturdily onto the bottom electrode in order to withstand the large thermal stresses developed in the sintering process via RTA.

However, on the other hand, it is also understood that a bottom electrode with certain degree of porosity may technically introduce several other issues. Electrically, porous Pt/Ti bi-layer literally reduces the effective bottom electrode area which in turns reduces the capacitance of the device. Dielectrically, the fast diffusion of Ti through pores on the bottom electrode results in a formation of TiO_2 in Pt and PZT. TiO_2 with lower dielectric constant can drastically reduce the net charge density of the device. Piezoelectrically, electrode porosity avoids partial PZT thin film to be activated through poling process and prevent it from being proper functional; see Figure 4.1. Mechanically, electrode pores pulled by the prolonged thermal treatment provide a pathway for fast Ti migration into the upper layers leading a depleted Ti bonding layer and subsequently cause a loss of Pt adhesion.

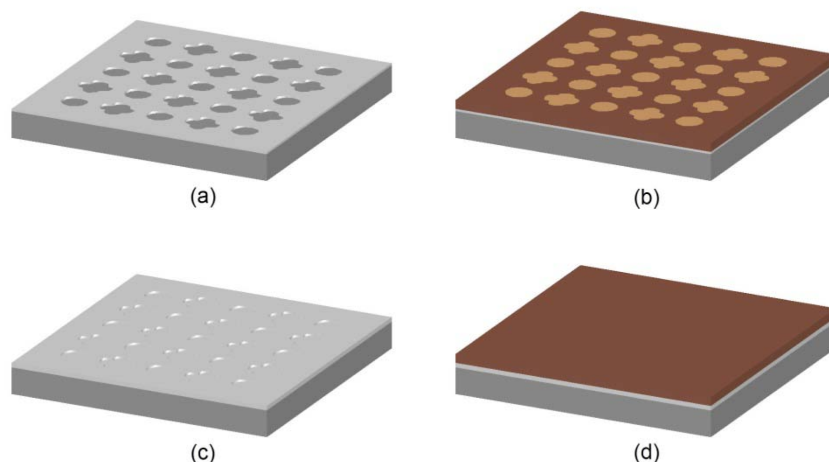

Figure 4.1: (a) Bottom electrode with porosity; (b) Partial PZT is functional on porous bottom electrode; (c) Bottom electrode with sealed pores; (d) PZT is fully functional on nonporous bottom electrode.

To cope with such dilemma, a novel-designed Pt/Ti bi-layer bottom electrode appears highly desired. Such bottom electrode should inherit the proper microstructure and morphology (i.e., “surface texture”) from electrode with low porosity to ensure good PZT thin film quality. Meanwhile, those pores generated under heat treatment can be effectively sealed to obtain full electrode area and assure PZT thin film to be fully functional.

In this chapter, we will first present a deposition and annealing procedure to fabricate such newly designed nonporous bottom electrode (NBE) with the desired surface texture. Then three-layer PZT stacks are spin-coated and sintered on the NBE alongside with the porous bottom electrode (PBE). To evaluate the performances of PZT thin film on both types of bottom electrodes, physical properties including PZT elastic modulus E, thin film leakage current density J, PZT hysteresis loop (P-E loop), as well as its piezoelectric coefficient d_{33}, are subsequently measured. Based on the special design, the performance of PZT thin film fabricated on NBE is expected to be improved comparing with that on PBE.

4.2. Sample Preparation

The beginning steps for samples preparation of PZT thin film with NBE and PBE quite follows the procedures described in Chapter 2 and start with commercial available 3-inch single-side polished bare silicon wafers (made by Montco Silicon Technologies, Inc., 3" P/BOR <1-0-0>

1-5OHM-CM, 356-406μm); see Figure 4.2(a). Wafers are first carefully selected, cleaned, and oxidized in a tube furnace (MRL812 atmospheric furnace stack tube 3) at 1050 °C for 3 hours to grow a SiO_2 layer of 500 nm thick; see Figure 4.2(b). Then a layer of silicon nitride of 200 nm thick is deposited by LPCVD (tube furnace No.3); see Figure 4.2(c). After nitridation process, wafers are grouped into two for different bottom electrode approach.

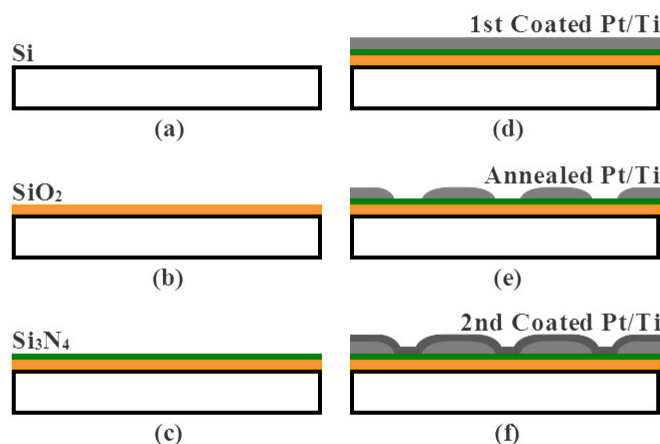

Figure 4.2: Fabrication sequence of nonporous Pt/Ti bi-layer bottom electrode

4.2.1 Pt/Ti Bi-Layer Bottom Electrode

Nonporous Bottom Electrode (NBE)

The wafers in first group are selected for NBE investigation. In Figure 4.2(d), the Pt/Ti bi-layer bottom electrode is deposited through NRC (Al) E-Beam evaporator under following conditions: deposition rate for Ti and Pt is 0.5 nm/s and 0.3 nm/s, respectively, and chamber pressure is set to be 3.0×10^{-6} Torr. In addition, the fabrication process consists of two subsequent rounds of deposition and annealing as follows. For the first round, 50 nm Ti and 50 nm Pt are sequentially deposited and later annealed in a tube furnace at 700°C for 30 min with same ramp up and ramp down rate of 13 °C/min. Figure 4.2(e) illustrates a side view of first round deposited bottom electrode becomes porous through the annealing process. Figure 4.3 also shows the degree of porosity on the Pt/Ti bi-layer on one selected wafer (SI-236) via an SEM nine-spot inspection; refer to Figure 2.10 for inspection location setup.

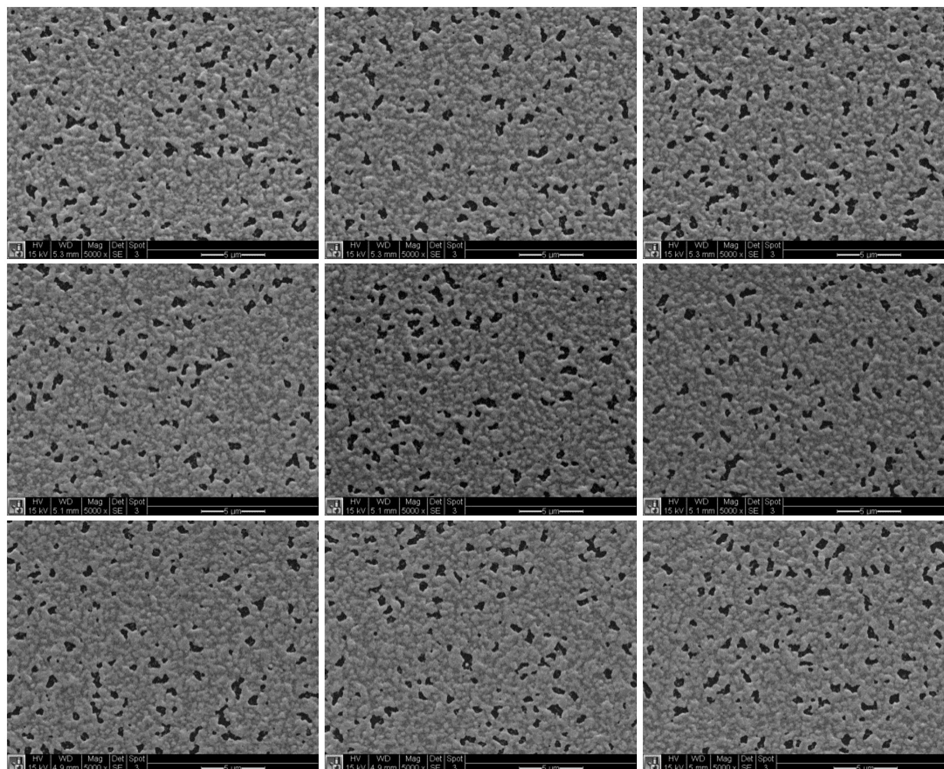

Figure 4.3: Porosity of first round deposited and annealed Pt/Ti bi-layer on wafer SI-236 via SEM nine-spot inspection.

For the second round of deposition, refer to Figure 4.2(f), another 50 nm Pt is deposited at a rate of 0.3 nm/s on top of just-annealed Pt/Ti bi-layer to seal the pores. To enhance mechanical strength of the newly deposited Pt, it is required to be heat treated under 700˚C for another 15 min with same ramp up and ramp down rate of 13˚C/min. Figures 4. 4 and 4.5 reveals the annealing temperature profile of second deposited bottom electrode and consequent SEM microstructure result. It is clearly to see that previously annealed porous bottom electrode is fully covered by later deposited Pt layer and now becomes nonporous, while the final electrode still maintains desire surface texture. All details for NBE two rounds bottom electrode deposition and annealing are summarized in Table 4.1.

Table 4.1: Empirical setups for NBE two rounds deposition and annealing

Deposition Round	E-Beam Type	Ti Thickness (nm)	Pt Thickness (nm)	Ramp up Rate (°C/min.)	Target Temp. (°C)	Dwell Time (min.)	Ramp down Rate (°C/min.)	Annealing Posture
1	NRC (Al)	50	50	13	700	30	13	Flat
2	NRC (Al)	N/A	50	13	700	15	13	Flat

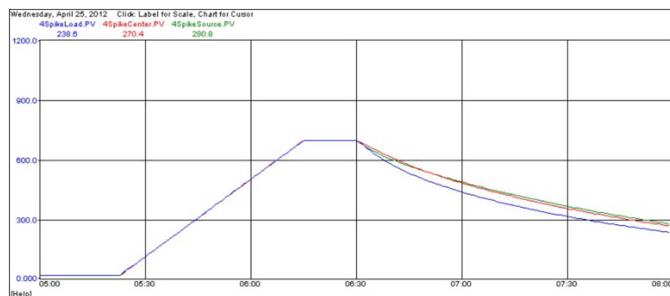

Figure 4.4: Annealing temperature profile of second deposited Pt layer on wafer SI-236

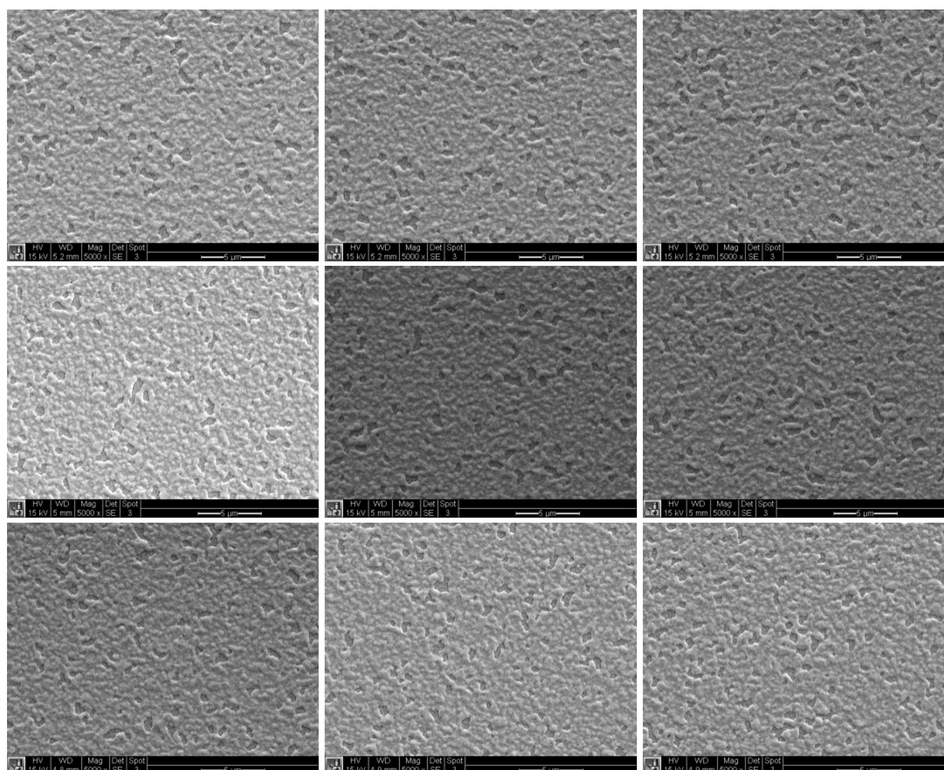

Figure 4.5: Pores of annealed Pt/Ti bi-layer bottom electrode on wafer SI-236 is sealed by second Pt layer becoming nonporous.

<u>Porous Bottom Electrode (PBE)</u>

Second group of wafers is reserved for PBE fabrication. Pt/Ti bi-layer deposition is carried out in the same NRC (Al) E-Beam evaporator with identical chamber pressure setting and Ti/Pt deposition rate. Other than NBE, PBE formation only involves one round bottom electrode deposition. Table 4.2 lists the detailed setting of PBE deposition and annealing. To keep the same overall electrode thickness, final deposition thicknesses of Ti and Pt are adjusted to 50 nm and 100 nm, respectively. Pt/Ti bi-layer is then annealed in tube furnace at 800˚C for 20 min

with equal ramp up and ramp down rate of 13°C/min ; see Figure 4.6. Thermal treated PBE on the wafer (SI-229) appears medium degree of porosity under SEM; See Figure 4.7. Figure 4.8 and Table 4.3 show the calculated porosity through MATLAB® R2010a image processing tools.

Table 4.2: Empirical setups for PBE deposition and annealing

Deposition Round	E-Beam Type	Ti Thickness (nm)	Pt Thickness (nm)	Ramp up Rate (°C/min.)	Target Temp. (°C)	Dwell Time (min.)	Ramp down Rate (°C/min.)	Annealing Posture
1	NRC (Al)	50	100	13	800	20	13	Flat

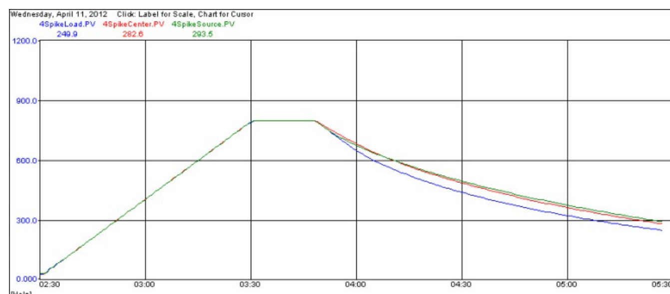

Figure 4.6: Annealing temperature profile of Pt/Ti bi-layer on wafer SI-229

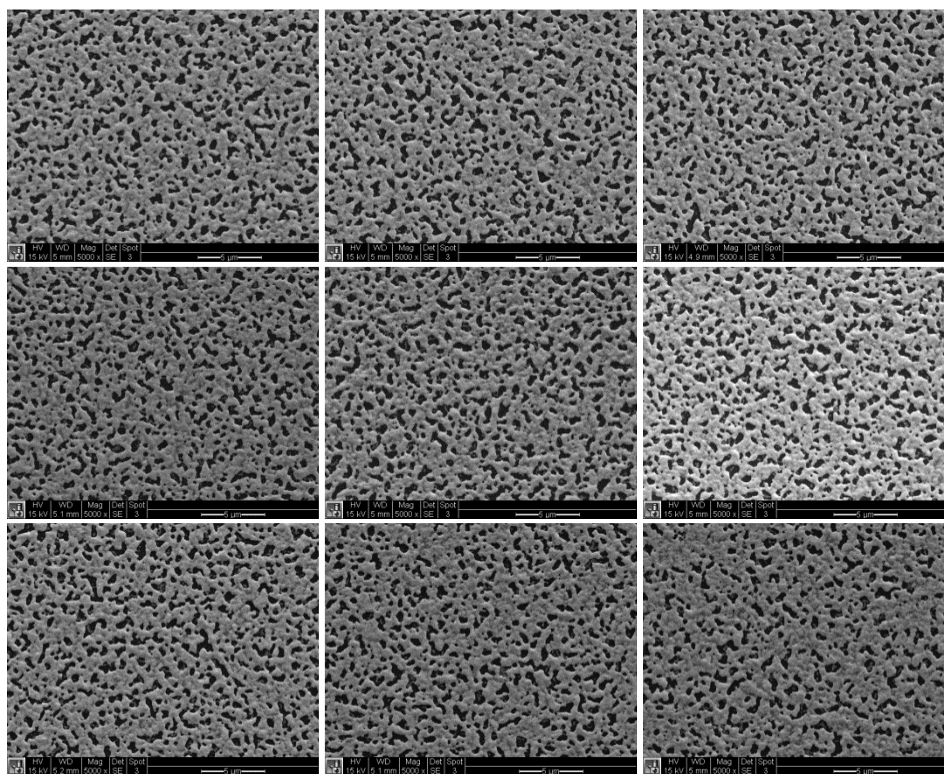

Figure 4.7: Porosity of deposited and annealed Pt/Ti bi-layer on wafer SI-229 via SEM nine-spot inspection.

Table 4.3: Calculated porosity of Pt/Ti bi-layer on wafer SI-229

Inspection Spot		Column 1	Column 2	Column 3	Average Porosity
Row	1	22.38%	22.73%	22.34%	22.63%
	2	23.18%	24.63%	22.16%	
	3	23.80%	22.85%	19.63%	

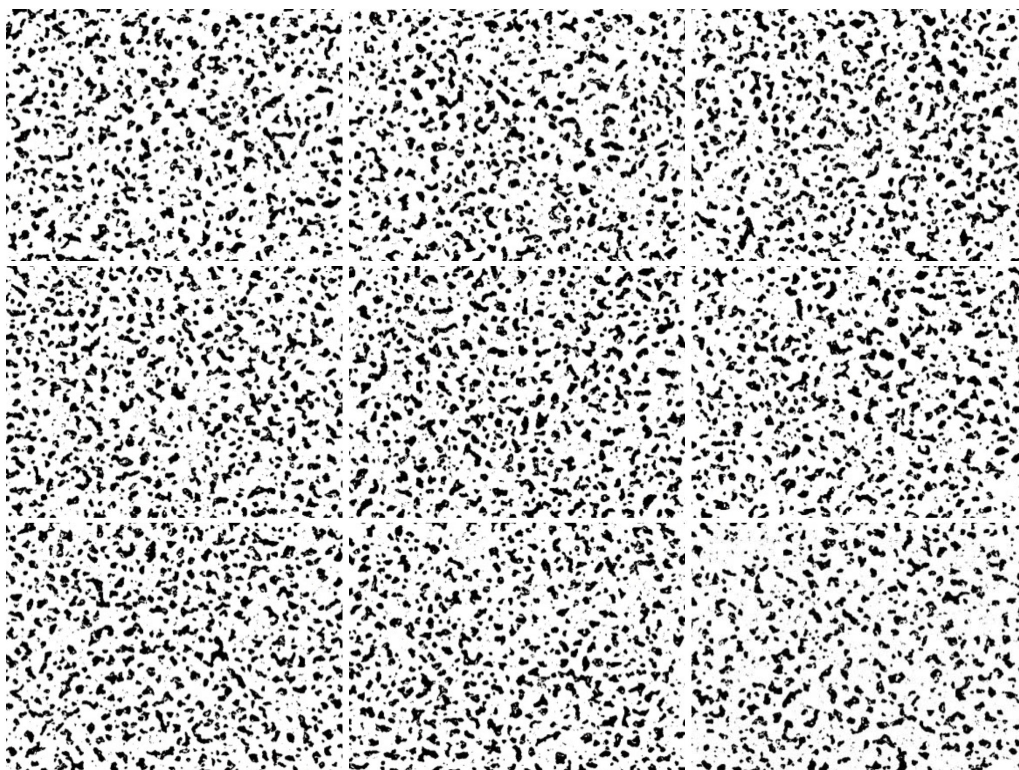

Figure 4.8: Calculated porosity of deposited and annealed Pt/Ti bi-layer on wafer SI-229 via MATLAB® image processing.

On bottom electrode annealing process, many researchers offer quite constructive suggestions. Some suggest that Pt/Ti bi-layer should be annealed under the protection of nitrogen (N_2) ambient. This could not only prevent Ti oxidation, but also drastically reduce Ti out-diffusion into both Pt and Si and insure a Pt layer with low surface roughness [179]. In addition, lower Ti diffusion allows a better PZT thin film growth with preferential crystal orientation [180-182]. The others, however, argue that Pt/Ti bi-layer annealed under oxygen ambient is required for the presence of TiO_2 on the top surface of bottom electrode through metal diffusion. During PZT coating process, these Ti could enrich PZT layer near the electrode

and reduce the activation energy for its nucleation [183]. The layer will later act as seed layer for the rest of the PZT film growth [184].

Following with the above thoughts, we pick two wafers (SI-227 and SI-232) with just-deposited Pt/Ti bi-layer and test-anneal them in tube furnace separately. First run, one wafer is thermal treated under nitrogen ambient. For the second run, tube furnace is filled with argon (Ar). Annealing temperature profile is chosen the same as that for PBE. Outcomes from two runs are, unfortunately, not satisfied. Figure 4.9 and 4.10 reveal macro and micro views of two annealed bottom electrodes under different ambient conditions. Pt/Ti by-layer on both wafers seem burnt or somewhat react with the filling gas although N_2 and Ar are normally considered to be inert. The results unfortunately halt us from further testing all due to their inapplicability.

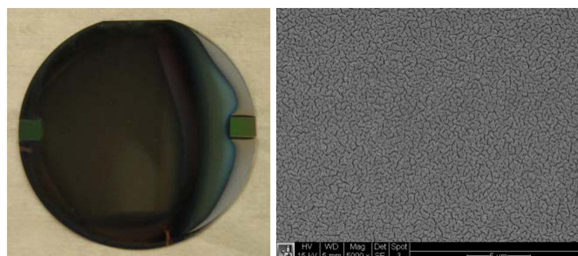

Figure 4.9: Macro and micro views of annealing result for Pt/Ti bi-layer (SI-227) in N_2 ambient.

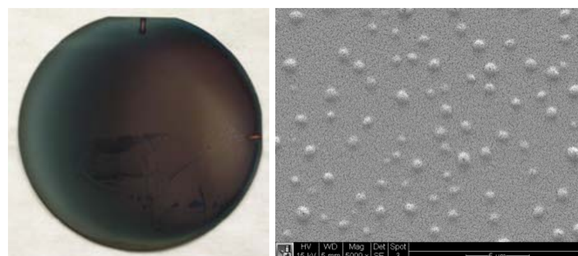

Figure 4.10: Macro and micro views of annealing result for Pt/Ti bi-layer (SI-232) in Ar ambient.

4.2.2 PZT Thin Film

Studies in Chapter 2 Section 2.4 already systematically help us sort out the critical factors to minimize defects and project a trend for producing a good PZT thin film. Besides the understanding on the degree of porosity on bottom electrode, drying methods for just-coated PZT thin film is found to be the second most crucial parameter; refer to Table 2.24. Sol-gel PZT prepared for coating bares a Zr/Ti ratio of 52:48 with 10% excess of Pb. Three layers of PZT gel films are successively spin-coated at room temperature (22 °C / 72 °F), each immediately

followed with 1 minute hotplate softbake and 15 minutes tube furnace RTA sintering. Wafers with NBE and PBE are coated with same prepared sol-gel PZT and heat treated together; see Table 4.4.

Table 4.4: Parameters for PZT thin film fabrication on wafers with NBE and PBE

Wafer No.	Pt/Ti Type	Pt/Ti Porosity	Sol-Gel Type	Aging (Day)	Humidity (%)	Dry Method	Dry Time (Min)	Dry Temp. (°C)	RTA Temp. (°C)	RTA Time (Min)
SI-236	NBE	N/A	Non-diluted	8	21	Hot Plate	1	100	650	15
SI-229	PBE	22.63%	Non-diluted	8	21	Hot Plate	1	100	650	15

4.2.3 Au/Cr Bi-Layer Top Electrode

Lift-off is the photolithography method adopted for top electrode patterning and it requires to be processed in advance of electrode deposition. P-20 primer and NR71-1000PY (Futurrex, Inc.) negative photoresist are first consecutively spin-coated on top surface of sintered PZT followed with UV exposure and developer patterning. Then Cr and Au are serially deposited in NRC (Al) E-Beam evaporator to form Au/C bi-layer top electrode. The deposition conditions are listed in Table 4.5. After overnight soaking in acetone tank, unexposed negative photoresist is dissolved to release unwanted part of Au/Cr bi-layer off the PZT surface. After three rounds DI water rinse, PZT with separated top electrode pads on top with desired pattern is achieved.

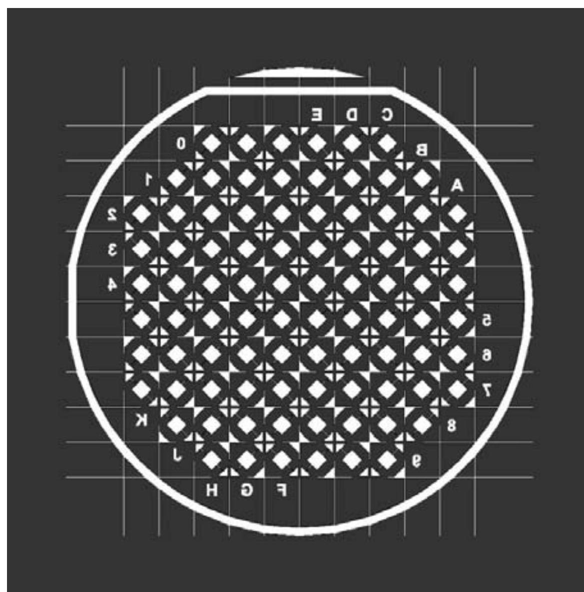

Figure 4.11: Special designed mask for Au/Cr bi-layer top electrode patterning

Table 4.5: Parameters for Au/Cr Bi-layer top electrode deposition

E-Beam Type	Deposition Pressure (Torr)	Cr Deposition Rate (nm/s)	Cr Thickness (nm)	Au Deposition Rate (nm/s)	Au Thickness (nm)
NRC (Al)	3.0×10^{-6}	0.1	25	0.5	100

The top electrode patterning mask used in the fabrication is specially designed for later piezoelectric coefficient d_{33} measurement purpose, see Figure 4.11. There are overall eighty-eight top electrode pads designed in the mask array. Figure 4.12 sketches the enlarged details of an individual electrode. One square-shaped pad is sitting in the middle and diagonally connected with two triangle pads in the corners through two interconnects. The interconnects serve as extraction top electrode while two triangle pads act as soldering pads in the later wire connecting. The whole structure has a combined effecting electrode area of 0.09 mm^2.

Figure 4.12: Details of one top electrode pattern

4.2.4 Specimen Finalization

Through above fabrication process, two groups of wafers now all bare setup as three-layer stack PZT thin film sandwiches in between NBE/PBE and top electrode. To make them testable, all wafers need to be further diced into small pieces of specimens with square size of 6 mm by 6 mm under dicing saw (DAD321 Automatic Dicing Saw by DISCO Corporation); see Figure 4.13(a). Top and bottom electrodes on each specimen have to be soldering connected with insulated lead wires for full function. Bottom electrode for a diced off specimen, however, only has extremely small area exposed around the edge. This makes it impossible for a directly wire connection. To solve the problem, another triangle pad is designed locating in the third corner of specimen on top of PZT thin film; see Figure 4.13(b). Soldered with lead wire, the triangle pad is then brushed with silver paste to connect with edge-exposed bottom electrode. Wired specimens are later glued onto a big aluminum block with epoxy (5 Minute® Epoxy by ITW

Devcon, Inc.). Meanwhile, the edge of specimen covered by silver paste is also packaging strengthened by epoxy to secure the electrode connection; see Figure 4.13(c). When epoxy is fully cured, all prepared specimens are 30 minutes individually poled under a 150 kV/cm electric field for PZT thin film activation. Figure 4.14 shows close view of a finalized PZT thin film specimen fixed on top of the aluminum block.

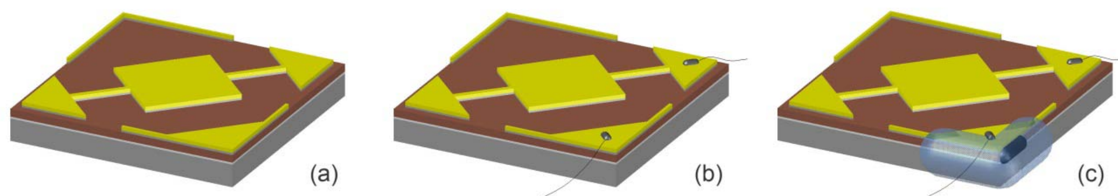

Figure 4.13: Details procedures of specimen finalization. (a) Dicing. (b) Wiring. (c) Packaging.

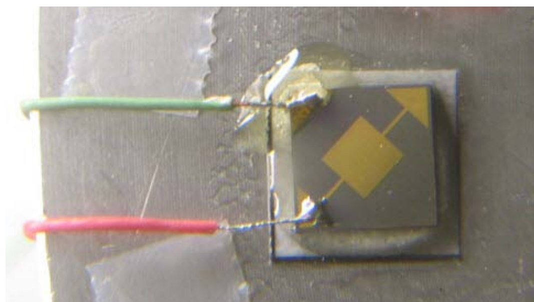

Figure 4.14: One piece of finalized testing specimen with thin-film PZT on top

4.3. Physical Properties Evaluation

The purpose of the study is to compare physical properties of PZT thin films when deposited on different type of bottom electrode. The range of evaluated properties for fabricated PZT thin film include: elastic modulus E_r, leakage current density J, hysteresis loop (P-E loop), and piezoelectric coefficient d_{33}.

4.3.1 Elastic modulus

Elastic modulus is commonly used to describe material stiffness. It is defined as the ratio of the axial load per unit area over the corresponding axial strain in the material elastic range. Experimentally, it can be determined from the slope of a stress-strain curves created during tensile or compressive tests conducted on a prepared material sample. In our application, PZT usually takes the form of thin film which makes it improper for a tensile load test. Nanoindenter,

however, provides another solution to deal with thin film material. The mechanism of nanoindenter for measuring elastic modulus of thin-film material has been well developed [185,186] and can be stated as follow. Nantoindenter forces a pre-designed chisel-shaped diamond tip penetrating straight downward into the thin film material. The tip will receive and continuously measure a resisting force generated by the material. Such force keeps increasing when the tip of indenter moves deeper. When the measured tip force reaches the preset maximum load P_{max}, tip motion will be immediately ceased. After a short holding with a constant load, the tip is retrieved but leaving a residual dent on the material surface. The project dent area A_c is then calculated as a function of dent depth caused by indenter tip. On the other hand, the slope of the initial portion of the tip unloading curve can be used for finding material initial unloading contact stiffness S [186]. Combining these two measurements, a so called elastic modulus E_r of thin film material can be accurately calculated through

$$E_r = \frac{\sqrt{\pi}}{2\sqrt{A_c}} S \tag{4.1}$$

The reason that thin-film PZT elastic modulus attracts our interests are two causes. First, elastic modulus is a frequent required material property for ANSYS model. Although in Chapter 3 Section 3.4 we already proved that such property only has a minor effect on simulation results, its real value for our lab-prepared thin-film PZT still remains skeptical. Second, thin-film PZT fabricated on substrate with porous bottom electrode is always challenged by Ti migration. Ti can easily penetrate electrode pores into the above layer during heat treatment, interfering PZT crystallization and its growing direction. This could introduce a relatively less condensed PZT with porous structure and lower hardness. However, so far there is no strong evidence from XRD results showing plane index of PZT will take <111> or <100> instead of <101> when under effect of Ti migration. But nonporous bottom electrode is still believed to be capable of working against Ti migration and mechanically improve PZT thin film property.

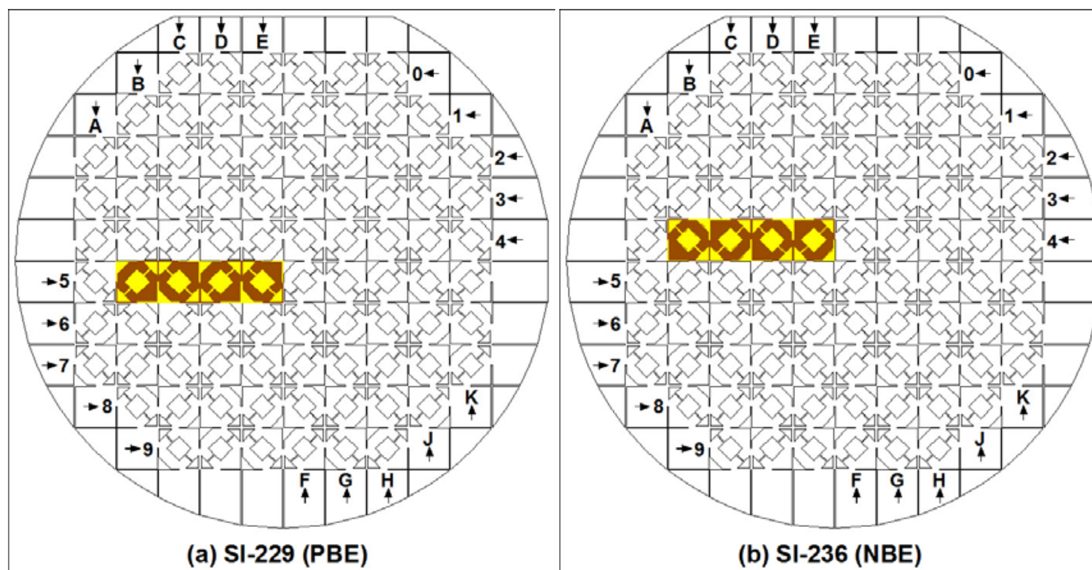

Figure 4.15: Thin-Film PZT specimens picked from substrate with PBE and NBE

In the study, eight PZT thin films specimens, four with PBE (from wafer SI-229) and four with NBE (from wafer SI-236) bottom electrodes, are picked and individually tested under nanoindenter (Ubi 1, HYSITRON, Inc); refer to Figure 4.15. The hardness and elastic modulus measurements on each coated thin film are conducted with a series loads ranging from 1000 µN to 2500 µN, corresponding to a contact depth from approximate 85 nm to 300 nm.

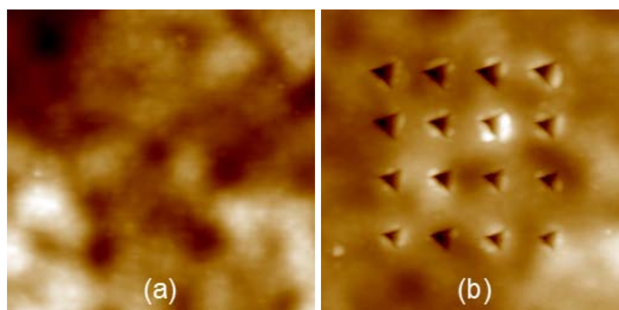

Figure 4.16: PZT thin film surface topography. (a) before and (b) after nanoindent test.

Figure 4.16 illustrates the nanoindent testing arrangement on one specimen. A series of loads with constant force increment of 100 µN are applied on a very small sample area. Locations of applied forces are defined as a four-by-four array with a spacing of 2 µm in between two consecutive points. Meanwhile, corresponding force-displacement relationships are registered by nanoindenter. Figure 4.17 shows four force-displacement relationships of one specimen under various loads. As discussed previously, hardness and elastic modulus of thin-

film PZT can be evaluated through each force-displacement curve and Equation (4.1). Table 4.6 provides a complete list of contact depth, hardness, and elastic modulus values for eight thin-film PZT specimens when same load magnitude of 1000 μN is applied.

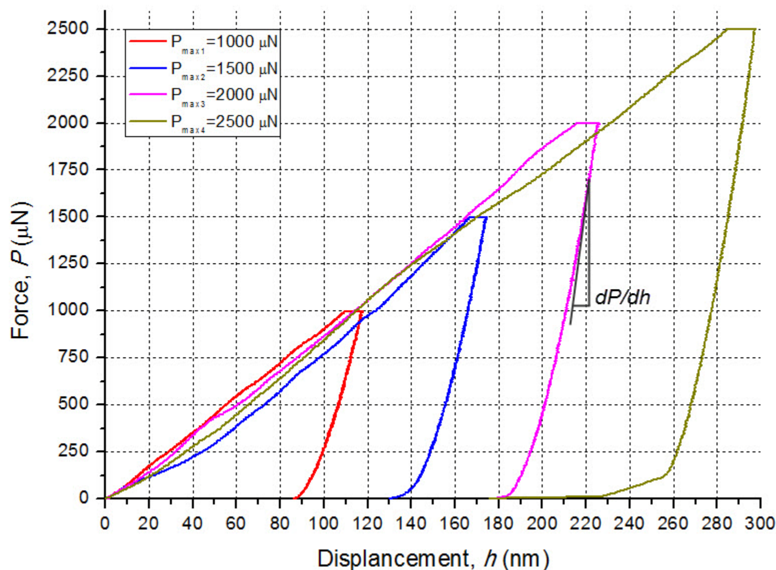

Figure 4.17: Force-Displacement relationships of one PZT thin film specimen through nanoindent test.

Table 4.6: Hardness and elastic modulus of thin-film PZT with PBE and NBE

Wafer	Specimen (No.)	Indentation Load P (μm)	Contact Depth h_c (nm)	Hardness H (GPa)	Elastic Modulus E_r (GPa)
SI-229 (PBE)	B5	1000	142.93	3.53	81.24
	C5		125.04	3.61	82.16
	D5		102.13	5.07	70.31
	E5		85.75	5.35	90.32
SI-236 (NBE)	B4	1000	105.54	4.31	91.47
	C4		134.19	3.34	87.99
	D4		102.72	4.44	97.16
	E4		101.74	4.49	91.14

Based on this experiment, we have two questions regarding to the measurement data that need to be addressed.

First, tested by nanoindenter under the same load, there is no obvious clue from Table 4.6 showing hardness H and elastic modulus E_r for PZT thin films that adopt NBE are greatly improved comparing with those on PBE. Considering the hardness and elastic modulus within each testing group (PZT with PBE or NBE), their variations are so large (around 20%) that can

easily compensate the differences between two groups. This makes it difficult to conclude that thin-film PZT on one type of bottom electrode is better than the other.

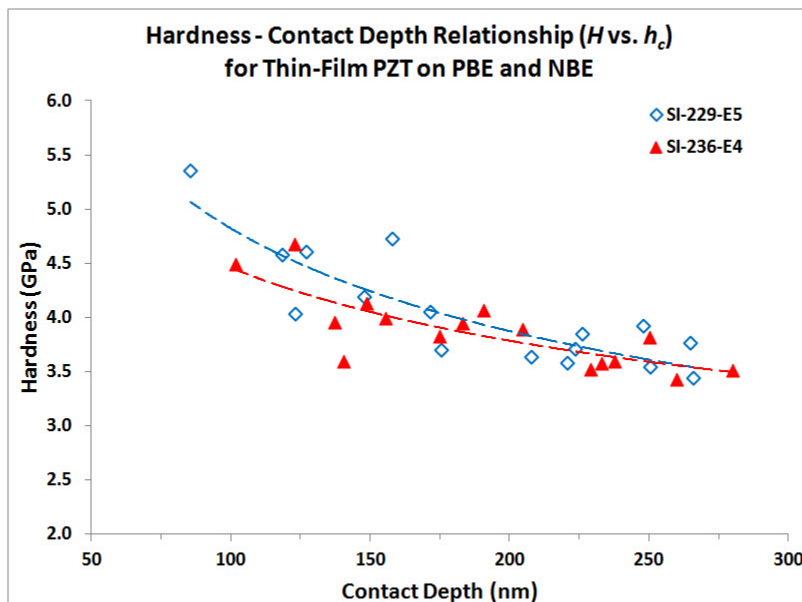

Figure 4.18: Hardness and contact depth relationship of PZT thin films on PBE and NBE

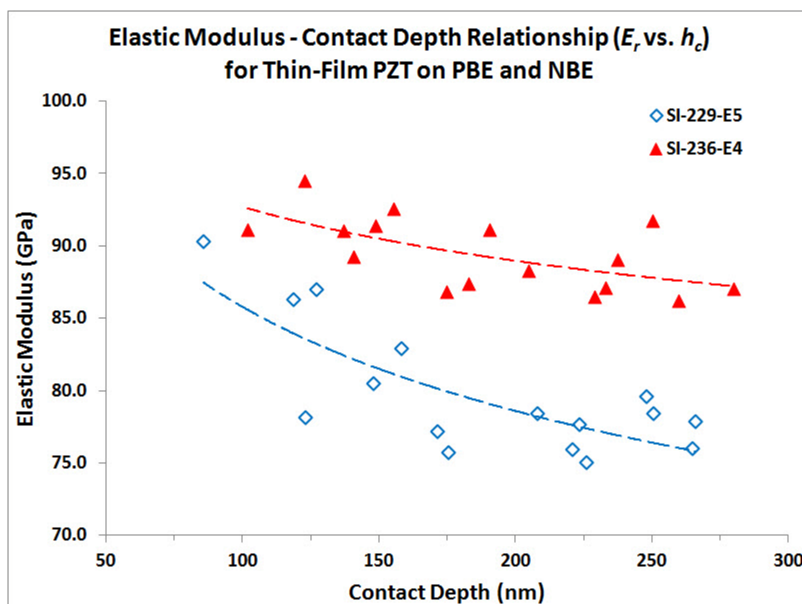

Figure 4.19: Elastic modulus and contact depth relationship of PZT thin films on PBE and NBE

Second, when considering individual testing specimen, indentation results reveal the dependence of the hardness and elastic modulus of PZT thin films on contact depths that are directly introduced by serial nanoindentation loads. As an example, Figure 4.18 and Figure 4.19

virtually include these two relationships for two PZT thin films on different type of bottom electrodes. Both hardness and elastic modulus are observed, however, following the same trend by decreasing their values when contact depth increases, which is quite opposite to our basic knowledge.

These two phenomena has, fortunately, been proposed and interpreted in some available literatures that such variation and reduction of both hardness and elastic modulus could be attributable to the effect of bottom electrode and substrate underneath the thin film coating [187,188].

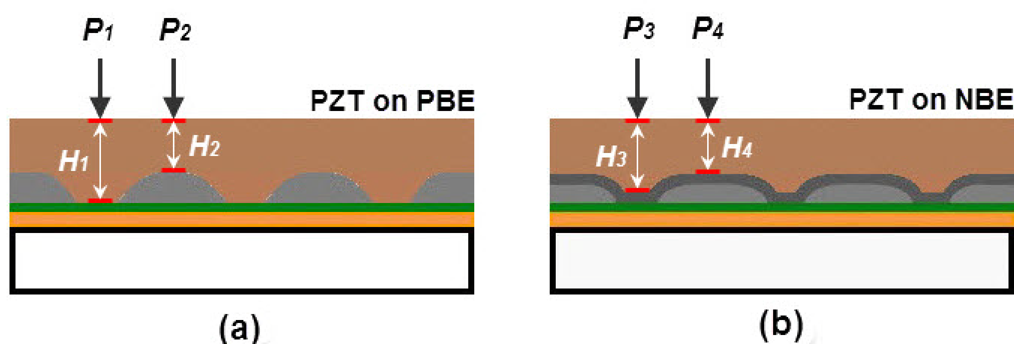

Figure 4.20: Cross section views of PZT thin films on PBE and NBE with indentation forces applied at various surface locations

For better understanding, Figure 4.20 sketches cross section views of PZT thin films on two types of bottom electrodes with nanoindentation forces applied in various surface locations. Let's first assume the condition that all forces are identical (P_1=P_2=P_3=P_4) and vertically added on the PZT surface. For the specimen with PBE, force P_1 happens to be applied straight above the pore of bottom electrode while force P_2 is above the electrode hillock. Effective thicknesses of PZT thin film at two forces locations are determined by H_1 and H_2 which are the distances from film surface to film/electrode interface. Since H_1 is greater than H_2, comparing with P_2 the indentation measurements of PZT thin film under P_1 is less likely to be affected by mechanical properties of bottom electrode. This could possibly explain why indentation measurements under same load at various PZT surface locations would bear large tolerance. Similar situation could possibly occur on specimen with NBE, where indentation measurements through force P_4 on thinner PZT location (thickness of H_4) tends to combine more effect from bottom electrode than those on thicker film location (thickness of H_3). Following with such concept a little bit

further, should indentation measurements for PZT thin film receive more influence from bottom electrode when deeper contact depth is achieved by larger applied force.

Looking back on our experiment data, it is noticed that with a given load of 1000 μN shown in Table 4.6 can only result contact depths less than 15% of PTZ thin film thickness. Within this depth range, indentation measurement cannot be affected by bottom electrode or substrate [189]. Even with acceptance of our measurements that do have electrode effect stored, when compared with the hardness and elastic modulus (12 GPa and 150 GPa) of thin-film PZT recently measured by X.J. Zheng et al. [189], those values (9 GPa and 140 GPa) for Pt/Ti bottom electrode reported by D.F. Bahr et al. [190] are not low enough to bring thin-film PZT indentation measurements down to less than 6 GPa and 100 GPa. Moreover, if we accept that these measurements are electrode influenced results, it indicates that our lab-fabricated thin-film PZT inherit extremely low mechanical properties. When indentation depth goes deeper, PZT thin film should receive more electrode compensation with a steady increment in both hardness and elastic modulus. However, parabolic (nonlinear) curves in both Figure 4.18 and Figure 4.19 do not agree with the hypothesis in their trends. Thus, we prove that the theory of bottom electrode and substrate effect is not applicable to our case.

Based on the observation, our conclusion can be stated as follow. Large variations in thin-film PZT hardness and elastic modulus are reasonable and the measurements are highly location dependent, simply because coating drying method and series of heat treatment during the process may potentially cause loose structure and quality nonuniformity throughout the whole PZT film. Since fabricated PZT thin film takes less condensed structure, its mechanical strength will decrease correspondingly. This could be the reason why hardness and elastic modulus for all tested PZT specimens are in constantly low level regardless the type of electrode used. The reduction in PZT hardness and elastic modulus, however, could be explained by another possible mechanism which is related to the density gradient of the thin film. It is proposed that sol-gel derived coatings may have a density gradient with density decreasing from the surface toward the interface between the coating and the substrate [191]. The density gradient could be due to the more restricted shrinkage and a slower drying rate at the interface compared with the relative free shrinkage and rapid solvent evaporation at the surface [187]. With the effect of decreased film density, PZT thin film surface has a better chance to be much harder than other places long film cross section direction pointing to the substrate.

4.3.2 Leakage Current Density

Leakage current is the current driven by the applied electric field flowing through the insulated material to the ground with absence of effective conducting path. Leakage current density is defined as such current divided by unit area. It is frequently used method for testing material electric behavior. Material either has very low density or internal defects may cause an unwanted current leaking. It is already known that bottom electrode porosity has a strong impact on PZT thin film crystallization orientation and thereafter affect film quality; refer to the studies on four major thin-film PZT defects induced by bottom electrode porosity patterns discussed in Chapter 2 Section 2.4.4. Such produced defects or micro voids could weaken thin-film PZT performance by enabling electron internal migration through the film from electrode on one side to the other. Meanwhile, with the adoption of PBE, Ti can easily merge through bottom electrode pores into PZT grain boundary during the heat treatment. This is another possible case to potentially enhance the film leaking. The selection of NBE is an improved electrode with proper surface microstructure that can not only maintain PZT defects in a very low level but also minimize the Ti migration. By measuring leakage current of thin-film PZT fabricated on both PBE and NBE, it will allow us instantly compare the electrode effect on electrical properties of PZT.

PZT thin films on two types of bottom electrodes are sequentially connected with leakage current meter (HP 4155B Semiconductor Parameter Analyzer) in series with a grounding connection. The range of applying voltage provided by the meter is preset to be 0-15 V with an increment of 0.1 V. The corresponding thin films leakage current densities are registered in Figure 4.21.

Similar variation ranges and trends for PZT thin films on different electrodes are observed. NBE electrode does not present much privileges compared with PBE to hold film current leaking. When applied voltage reaches above 13 volts, measured current density for thin-film PZT on NBE quickly shoots up indicating the existence of film defects in certain location. On the other hand, one should be noticed that Ti migration, if there is some, is not effectively isolated by NBE as expected. Its effect on leakage current still remains unknown based on the limited conducted tests.

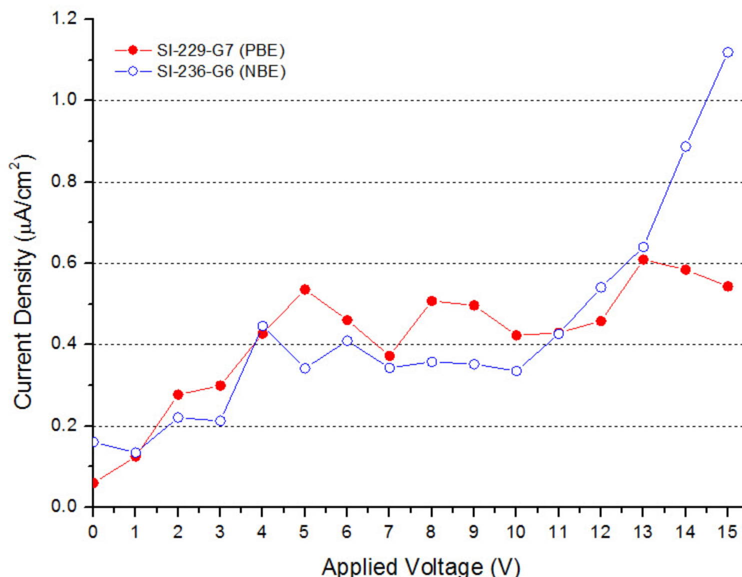

Figure 4.21: Leakage current density (*J-V* curves) of PZT thin films on PBE and NBE

4.3.3 Hysteresis Loop (P-E Loop)

Hysteresis loop is to measure material polarizing behavior under symmetrically applied positive and negative electric fields. During the experiment, thin-film PZT is first poled reaching its saturation point under a positively increasing electric field. When such field is switched to opposite direction, thin film will be gradually depolarized and reversely poled. After switching the electric field back to positive direction again, a PZT hysteresis loop (P-E loop) can be obtained. In the P-E loop, remnant polarization (P_r) and coercive field (E_c) are usually two most important factors used for judging PZT ferroelectric properties. Remnant polarization determines the stability of polarization after removal of poling electric field. Coercive field, on the other hand, determines the ferroelectric material poling capability. For microactuator and microsensor application, thin-film PZT often pursues higher remnant polarization and coercive field. This is because high coercive field can prevent PZT from being depolarized when operating under certain applied voltage range. High remnant polarization, in the meantime, ensures PZT providing large energy density.

In the test, we serially conduct P-E loop measurements on our lab-prepared PZT thin films with two different bottom electrodes. Figure 4.22 illustrates the testing curves while correlated property measurements are listed in Table 4.7. It is observed that both remnant polarization and coercive field of three PZT thin films on NBE are slightly but constantly larger than those of films

on PBE (ex. 16.17 μC/cm^2 vs. 14.06 μC/cm^2 and 158.69 kV/cm vs. 155.64 kV/cm). Although such increments in measured properties are not significant, it is reasonable to claim that NBE does play an important role. Through special bottom electrode fabrication, NBE successfully enlarges the effective electrode area by covering the pores, which later enable it activate more PZT material to be functional.

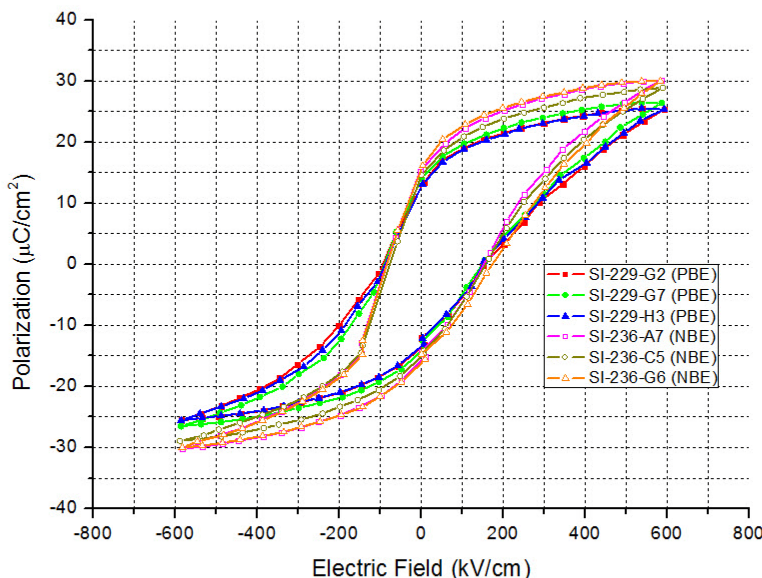

Figure 4.22: Hysteresis loops (*P-E* loops) for PZT thin films on PBE and NBE

Table 4.7: Ferroelectric properties for PZT thin films on PBE and NBE

Wafer No.	Electrode Type	Specimen No.	P_r (μC/cm^2)	E_c (kV/cm)
SI-229	PBE	G2	13.45	149.54
		G7	14.06	155.64
		H3	13.09	152.59
SI-236	NBE	A7	15.29	167.85
		C5	14.61	164.80
		G6	16.17	158.69

4.3.4 Piezoelectric Coefficient d_{33}

Adopting the method that well defined in Chapter 3, we are able to calibrate, restore, and compare real piezoelectric coefficient d_{33} for PZT fabricated on NBE and PBE. Before the test, three PZT thin films, one on NBE and two on PBE, are picked and sequentially measured for capacitances through impedance analyzer (Agilent 4294A Precision Impedance Analyzer). In the

finite element simulation, ANSYS adopts the size of thin-film PZT substrate defined in Section 4.2 and thin film elastic modulus found in Section 4.3.1 for analyzing the PZT charge-force relationship. The simulation result shows a straight line with slope of 55.4 pC/N and has been included in Figure 4.23 as reference. Material type of our PZT is still assumed to be same as bulk PZT-7A with a theoretical d_{33} value of 153 pC/N. By taking the ratio between this theoretical d_{33} and its simulated value, a d_{33} calibration factor for the PZT-7A thin film is calculated as

$$\alpha = \frac{153}{55.4} \approx 2.8 \tag{4.2}$$

Three previously selected PZT thin films are now consecutively tested under mini impact hammer with applied force range from 1 N to 10.4 N. After multiplying with α=2.8, the calibrated charge-force relationships (*αQ vs. F*) derived from the experiments for three PZT thin films are illustrated in Figure 4.23. All measured electric and piezoelectric properties are summarized in Table 4.8. It is observed that two calibrated piezoelectric coefficient d_{33} for PZT thin films on PBE are both slightly lower when compared with that for PZT with NBE. The testing results quite make sense since NBE with full electrode surface area can pole more PZT material to activate and generate additional surface charge under same hammer impact load.

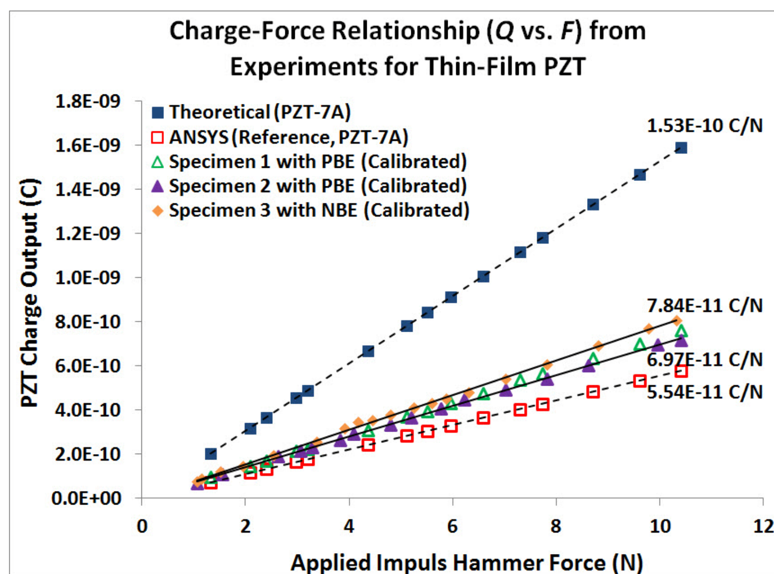

Figure 4.23: Charge-force relationship of PZT thin film specimens on PBE and NBE

Table 4.8: Electrical and piezoelectric properties for PZT thin film specimens on PBE and NBE

	SI-236 (NBE)	SI-229 (PBE)	
	A5	C2	C4
Capacitance *C* (nF)	31.686	28.507	29.582
Dielectric Constant ε_r	477.379	429.487	445.680
α Corrected d_{33} (pC/N)	78.4	73.9	69.7

4.4. Summary

In this chapter, Pt/Ti bi-layer nonporous bottom electrode (NBE) has been developed, fabricated, and applied. Its effect on thin-film PZT mechanical, electrical, ferroelectric, and piezoelectric properties has been investigated and demonstrated through comparison with porous bottom electrode (PBE). Our prediction that NBE should surpass PBE in promoting thin-film PZT performance does not well supported by the limited experimental results. However, NBE contains large effective electrode area by covering the pores earns it better chance to outperform PBE. Based on the experiment, our conclusions are summarized as follow:

1. Despite of NBE and PBE selection, nanoindentation results shows that hardness and elastic modulus of our lab-fabricated thin-film does not affected by bottom electrode or substrate effect. Instead, its low value can be due to the less condensed film structure resulting from fabrication process. The large variation in the values are possibly caused by thin-film PZT quality nonuniformity. We also observe that those values for PZT hardness and elastic modulus steadily decrease when indentation measurement taken from thin film surface toward film/electrode interface.
2. Leakage current density measurements for PZT thin films on NBE and PBE are quite competitive. No obvious clue shows NBE provide significant improvement in PZT film electric properties. In addition, previously suspected Ti migration effect is not verified as a critical issue causing a big increment of film leakage current.
3. Although hysteresis loop (P-E loop) measurement reveals that both remnant polarization and coercive field of PZT thin films on NBE are constantly greater than those on PBE, their values do not bear large enough difference to unconvincingly claim NBE brings privilege on PZT ferroelectric properties.
4. Similar trends in piezoelectric coefficient measurement are observed that thin-film PZT on NBE has slightly larger d_{33} when compared with that on PBE. But since the number of tested

specimens are limited and finite element model used for finding d_{33} is not custom designed, our weakened experiment results could hardly be considered as a seasonable support to NBE.

Chapter 5: Conclusions and Future Work

5.1 Conclusions

In this thesis, I have illustrated the research need and process enhancement for fabricating thin-film PZT with satisfied quality. PZT integrated microdevice is undoubtedly promising, but its development and fabrication still remains challenging. To cope with such challenges and develop a well functional microdevice with adoption of thin-film PZT in sub-millimeter range requires thorough understand on its properties and fundamental behaviors both in theoretical and practical way.

For the first part, an entire process for fabricating crack-free thin-film PZT based microdevice is thoroughly investigated and practiced. In the meantime, valuable modifications on key processes are contributed for fabrication improvements. A systematic investigation is conducted right after characterizing four major defect types of sol-gel derived PZT thin film. It is discovered that thin film defects are strongly related the degree of porosity on Pt/Ti bi-layer bottom electrode. Parametric study proves that thin-film PZT imperfections will be greatly alleviated when bottom electrode porosity is effectively controlled in a relatively low level (usually less than 20%). In addition, it is also noticed that thin-film PZT defect grade will suddenly uprise when bottom electrode porosity drop to zero.

The Porosity on Pt/Ti bi-layer bottom electrode can be classified into four major degrees, and it is understood to be a combined effect of many electrode deposition and annealing factors. Another parametric study has been carried out for prioritizing the adjusting order and values of corresponding factors. It clearly shows that Pt/Ti bi-layer bottom electrode through optimized fabrication has a stable trend to bear low electrode porosity while maintaining proper surface micro texture. It can effectively assure the quality of thin-film PZT lately deposited on top of it.

For the second part, I developed and demonstrated a very simple and low-cost method to measure piezoelectric coefficient d_{33} of PZT thin films. The method adopts a mini-impact hammer, a charge amplifier, and an oscilloscope. Prior to the experiment, a finite element analysis is conducted to estimate a calibration constant to compensate for the substrate effects associated with the specimen. From the measured force and charge and the calculated

calibration constant, we can estimate the piezoelectric coefficient d_{33}. Experimental results on both thick-film and thin-film PZT specimens with known piezoelectric coefficients indicate that the method is accurate. It is noted that for a thin-film PZT application impact force level needs to be capped to avoid material depolarization. With the measured d_{33}, we can also predict the displacement of PZT thin-film membrane actuators accurately to match with existing experimental results.

For the last part, Pt/Ti bi-layer nonporous bottom electrode (NBE) has been developed, fabricated, and applied. Its effect on thin-film PZT mechanical (nanoindentation) property, electrical (leakage current density) property, ferroelectric (hysteresis loop) property, as well as piezoelectric (piezoelectric coefficient) property has been investigated and demonstrated through comparison with porous bottom electrode (PBE). Due to the limited experimental results, there is lack of strong evidence showing new electrode surpasses traditional one in all ways. However, NBE contains large effective electrode area by covering the pores earns it better chance to outperform PBE.

5.2 Future Work

The work in this thesis successfully improved thin-film PZT fabrication yield through parametric study. Based on the current situation, thin-film quality is mainly determined by bottom electrode porosity while the degree of electrode porosity is majorly affected by e-beam selection. However, with the evolution of thin-film PZT fabrication process as well as the adoption of larger silicon substrate (4-inch wafer), many new parameters could be involved potentially influence their results. For the case, the current conclusion may not apply and additional parametric study should be carried out correspondingly.

Newly design thin-film PZT piezoelectric coefficient measurement is appealing. However, its application should be very carefully restricted in a very low force range to avoid PZT thin film damage and depolarization. Moreover, this method is restricted to a relative small sample with fixed PZT, bottom electrode, and substrate thickness ratio. Testing on a PZT sample with very large surface area or various thickness ratio may introduce large measurement error. Based on this reason, the mini impact hammer method still need to be modified.

Nonporous bottom electrode is achieve. But its fabrication process so far is still not quite stable. This is because there is no Ti layer involved during the bottom electrode second deposition. Improper heat treatment many still cause electrode delamination of peel off. So additional work on modifying the process is required.

Appendix A

Bottom Electrode Porosity Calculation Code

```
clear all;
close all;


ImagefileName = imread('O:\Porosity\Figure 2.49f.TIF');

% Change RGB Colormap To Grayscale
% originalpic = rgb2gray(originalpic);
%++++%imshow(ImagefileName);
% roipic = imcrop;

% [MouseX, MouseY] = ginput;
ROI_Rect = [1 1 645 483];
roipic = imcrop(ImagefileName, [ROI_Rect(1,1) ROI_Rect(1,2)
ROI_Rect(1,3) ROI_Rect(1,4)]);

% AdjImage = histeq(roipic);

AdjImage = imadjust(roipic,stretchlim(roipic),[]);

%   imshow(roipic);
%   figure,
%++++%imshow(AdjImage);

% hold on

% I = imread(AdjImage);
imhist(AdjImage);

I=imhist(AdjImage);

% Average PicInten
AveInten = 50;

for ImgRow = 1:484

    for ImgCol = 1:645

        if AdjImage(ImgRow, ImgCol) > AveInten

            AdjImage(ImgRow, ImgCol) = 255;

        elseif AdjImage(ImgRow, ImgCol) < AveInten

            AdjImage(ImgRow, ImgCol) = 0;
```

```
        end

    end

end

%++++%imshow(AdjImage);

% Pick out the white point and black point
WhtPnt = 0;
BlkPnt = 0;
for ImgRow = 1:484

    for ImgCol = 1:645

        if AdjImage(ImgRow, ImgCol) == 0

            BlkPnt = BlkPnt + 1;

        elseif AdjImage(ImgRow, ImgCol) == 255

            WhtPnt = WhtPnt + 1;

        end

    end

end

imshow(AdjImage);

WhtPnt
BlkPnt

(BlkPnt/(WhtPnt+BlkPnt))*100
```

VITA

Qing Guo, a typical Shanghainese, was given birth in October 1977 in district of Hongkou, city of Shanghai, China. During childhood, he went to Tianjin for six-year elementary school. Early 1990's, he came back to Shanghai for junior (No. 1 Junior High School Affiliated to East China Normal University) and senior high school (Beihong Senior High School), and graduated in 1993 and 1996, respectively. After four years study, he completed his B.S. degree in Mechanical Engineering at Shanghai University, Shanghai, China in 2000. After two years working as an electro-mechanical engineer in Shanghai SINE pharmaceutical company, he decided to attend Cleveland State University in Cleveland, Ohio for advanced education. In late 2004, he received his M.S. degree in Mechanical Engineering. After a short break, he joined University of Washington at Seattle, Washington in 2005. As a Ph.D. student in Mechanical Engineering, he worked towards the development of thin-film PZT based MEMS devices. Four years later, he attempted his first entrepreneurship in solar business, which was proved as a heavy interruption on his school project. In 2012, he focused back on his research and successfully accomplished the graduate study. He received dual Ph.D. degree from both department of Mechanical Engineering and Center of Nanotechnology in June and became the sixth Ph.D. in the family. Two years delay in graduation is indeed a harsh lesson, however, the opportunities working tightly with several top venture capitals as well as University of Washington Center of Commercialization could be his priceless experience. He married with his wife in Alki beach right after graduation. Now, he considers Seattle as home.